



저작자표시-비영리-변경금지 2.0 대한민국

이용자는 아래의 조건을 따르는 경우에 한하여 자유롭게

- 이 저작물을 복제, 배포, 전송, 전시, 공연 및 방송할 수 있습니다.

다음과 같은 조건을 따라야 합니다:



저작자표시. 귀하는 원저작자를 표시하여야 합니다.



비영리. 귀하는 이 저작물을 영리 목적으로 이용할 수 없습니다.



변경금지. 귀하는 이 저작물을 개작, 변형 또는 가공할 수 없습니다.

- 귀하는, 이 저작물의 재이용이나 배포의 경우, 이 저작물에 적용된 이용허락조건을 명확하게 나타내어야 합니다.
- 저작권자로부터 별도의 허가를 받으면 이러한 조건들은 적용되지 않습니다.

저작권법에 따른 이용자의 권리는 위의 내용에 의하여 영향을 받지 않습니다.

이것은 [이용허락규약\(Legal Code\)](#)을 이해하기 쉽게 요약한 것입니다.

[Disclaimer](#)

공학박사학위논문

**Prediction on the Excitation  
Loads and Vibratory Response of  
the Supersonic Flight Vehicle  
with Air Breathing Inlet**

공기 흡입구를 가진 초음속 비행체의  
가진하중 및 진동응답 예측에 관한 연구

2017년 2월

서울대학교 대학원

기계항공공학부

김진형

Prediction on the Excitation Loads and  
Vibratory Response of the Supersonic Flight  
Vehicle with Air Breathing Inlet

공기 흡입구를 가진 초음속 비행체의  
가진하중 및 진동응답 예측에 관한 연구

지도교수 신 상 준

이 논문을 공학박사 학위논문으로 제출함

2016년 12월

서울대학교 대학원

기계항공공학부

김진형

김진형의 공학박사 학위논문을 인준함

2016년 12월

위원장 : 李 樹 甲   
부위원장 : 申 尙 垸   
위원 : 李 營 中   
위원 : 金 基 秀   
위원 : 田 赫 秀 

## **Abstract**

# **Prediction on the Excitation Loads and Vibratory Response of the Supersonic Flight Vehicle with Air Breathing Inlet**

**Jinhyeong Kim**

**School of Mechanical and Aerospace Engineering**

**The Graduate School**

**Seoul National University**

This thesis presents an estimation methodology on the vibratory response of the supersonic flight vehicle caused by various dynamic loads during operation. High-speed flight vehicle (HSFV) is an imaginary supersonic flight vehicle with an air breathing engine (i.e., ramjet engine). It undergoes severe dynamic loads which are generated during the launch and in-flight environments. And a typical vehicle is composed of thin plate skin structures with high-performance electronic units sensitive to such vibratory loads. Such lightweight structures are then exposed to external dynamic loads which consist of random excitation, shock, and acoustic loads created under the operating environments. Three types of dynamic

loads (acoustic loads, rocket motor self-induced excitation loads and aerodynamic fluctuating pressure loads) are considered as major components in this thesis. Generally, for large structural components such as an entire launch vehicle considering high frequency range, proper structural response analysis method should be chosen because it is known that deterministic method (such as finite element analysis) is not capable of precisely and efficiently predicting the response for high frequency ranges. To overcome such limitations of the deterministic method for high frequency range, statistical energy analysis is used in this thesis. The estimation results are compared with respect to the design specification (MIL-STD-810) to examine the appropriateness. The objective of this thesis is to study an estimation methodology which helps to establish design specification for the dynamic loads acting on the vehicle which cannot be followed general design procedure because there exit a little data can be applied to establish design dynamic loads.

**Keyword: Vibratory Response, Statistical energy analysis,  
Acoustic load, Rocket motor self-excited load,  
Aerodynamic fluctuating pressure load.**

**Student Number: 2013-30195**

# Contents

<b>Abstract</b> .....	<b>i</b>
<b>Contents</b> .....	<b>iii</b>
<b>List of Tables</b> .....	<b>vi</b>
<b>List of Figures</b> .....	<b>vii</b>
<b>Chapter 1. Introduction</b> .....	<b>1</b>
1.1. Background and Motivation .....	1
1.2. Dynamic Loads on a High Speed Flight Vehicle.....	6
1.2.1. Rocket Motor Vibratory Loads.....	7
1.2.2. Acoustic Vibratory Loads .....	8
1.2.3. Aerodynamic Fluctuating Pressure Excitation Loads.....	8
1.3. Analytical Method for the Higher Frequency Response.....	10
1.4. Objectives and Layout of Thesis .....	14
<b>Chapter 2. Statistical Energy Analysis</b> .....	<b>17</b>
2.1. Brief Historical Background.....	17
2.2. Theoretical Background .....	20
2.3. Advantages and Limitations .....	37

<b>Chapter 3. Dynamic Loads on the High Speed Flight Vehicle during</b>	
<b>Launch Events.....</b>	<b>39</b>
3.1. Acoustic Loads on the Launch Pad .....	39
3.2. Rocket Motor Vibratory Load .....	46
3.2.1. Rocket Motor Self-Excited Vibration.....	46
3.2.2. Overview of Input Force Estimation .....	49
3.3. Aerodynamic Fluctuating Surface Pressure Excitation Loads	50
<b>Chapter 4. Input Force Estimation Method to Predict the Rocket</b>	
<b>Motor Self-Excited Loads.....</b>	<b>52</b>
4.1. Introduction .....	52
4.2. Theoretical Background .....	53
4.3. Verification by a Simple Structure.....	67
<b>Chapter 5. Prediction on Fluctuating Surface Pressure of the High</b>	
<b>Speed Flight Vehicle.....</b>	<b>83</b>
5.1. Introduction .....	83
5.2. Present Prediction Procedure.....	87
5.3. Existing Semi-Empirical Model for the Attached Flows.....	90
5.3.1. Cockburn and Robertson’s model .....	90
5.3.2. Emfimtsov’s model .....	92
5.3.3. Goody’s model .....	93

5.4. Verification of the present prediction procedure .....	95
5.4.1. Rocket Motor Self-Excited Vibration .....	95
5.4.2. Predicting fluctuating pressure using the present procedure on the ATLAS-Agena shroud.....	96
5.4.3. Examination of the surface pressure fluctuation spectrum .....	108
5.5. Fuselage excitation on a high speed flight vehicle.....	114
5.5.1. Development of the present prediction analysis .....	114
5.5.2. Prediction on the fluctuating surface pressure of the vehicle .....	119
<b>Chapter 6. Vibratory Response Analysis Using SEA.....</b>	<b>129</b>
6.1. Development of the Present Response Analysis Model ...	129
6.2. Discussion of the predicted structural Response .....	135
<b>Chapter 7. Conclusions and Future Works .....</b>	<b>147</b>
7.1. Summary .....	147
7.2. Future Works .....	151
<b>Bibliography .....</b>	<b>152</b>
<b>Appendix .....</b>	<b>162</b>
<b>Abstract in Korean.....</b>	<b>180</b>

## List of Tables

Table 1-1	Analysis methodology in terms of frequency range (full-scale launch vehicle) .....	5
Table 2-1	Modal density of the basic subsystems [14, 15] .....	28
Table 4-1	Dimensions and material properties of the cantilevered beam .....	69
Table 5-1	Flight and CFD analysis condition of ATLAS-Agena ...	107
Table 5-2	Cases of sub-iteration .....	107
Table 5-3	Flow parameters for the present flight condition .....	113
Table 5-4	Parameters of the present CFD analysis for HSFV .....	118
Table 6-1	OASPL on the surface (vehicle flight altitude: 6m) .....	131

## List of Figures

Fig. 1-1	Analysis procedure of the vibratory loads of a launch vehicle..	
	.....	5
Fig. 1-2	Dynamic behavior and analysis methodologies in terms of frequency range [7] .....	12
Fig. 1-3	Desing loads estimation procedure.....	16
Fig. 2-1	Characteristic of the natural frequency uncertainty in high order modes (FRF of acoustic pressure measured in the room).....	19
Fig. 2-2	Schematic of SEA model.....	24
Fig. 2-3	Illustration of the junction type [14].....	30
Fig. 2-4	Experimental method for defining damping [18].....	34
Fig. 2-5	Empirical damping loss factor for steel and aluminum thin plates and shells in the size range of 0.1 – 10 m [18] .....	36
Fig. 3-1	Illustration of the acoustic source locations and propagation.... .....	43
Fig. 3-2	Overall sound pressure level at each station with respect to the altitude of the vehicle.....	44
Fig. 3-3	Sound pressure level at each position on the surface in terms of the frequency at a fixed.....	45

Fig. 3-4	Rocket motor excitation loads and acoustic pressure measurements from the static firing test .....	48
Fig. 3-5	Procedure for defining the TBL parameters using VA-ONE.	51
Fig. 4-1	Complete operating procedure of the Kalman filter [34] .....	57
Fig. 4-2	Flow chart of the recursive input estimation algorithm.....	66
Fig. 4-3	Finite model of the cantilever beam .....	69
Fig. 4-4	Example of Rayleigh damping .....	70
Fig. 4-5	Comparison between measurement and estimated results for the sinusoidal force (without measurement noise).....	73
Fig. 4-6	Comparison between measurement and estimated results, sinusoidal force (with measurement noise, $\sigma = 1.0 \times 10^{-5}$ ).....	74
Fig. 4-7	Time history of the comparison between measurement (blue line) and estimation result (red line), impulsive force .....	77
Fig. 4-8	Frequency spectrum of the comparison between exact (blue line) and estimation force (red line), impulsive force .....	78
Fig. 4-9	Time history of the comparison between measurement (blue line) and estimation result (red line), (Random excitation) .....	81
Fig. 4-10	Frequency spectrum of the displacement and input force ...	82
Fig. 5-1	Procedure for determining the fluctuating surface pressures using CFD and VA-ONE.....	99

Fig. 5-2	Characteristics of the aerodynamic fluctuating pressures for ATLAS-Agena payload shroud [13] .....	94
Fig. 5-3	Verification analysis object configuration (FEA grid, ATLAS- Agena).....	102
Fig. 5-4	Variaton of the FSP spectrum with respect to number of sub- iteration .....	102
Fig. 5-5	CFD analysis results of ATLAS-Agena.....	103
Fig. 5-6	Distribution of the overall surface pressure spectra and dynamic pressure on the vehicle .....	104
Fig. 5-7	Time history of the total pressure in Zones 1 and 2 .....	105
Fig. 5-8	Surface pressure spectrum in terms of the distance from starting point of the attached flow.....	106
Fig. 5-9	Comparison between the present CFD results and the existing semi-empirical models (in Zone 4) .....	107
Fig. 5-10	Auto spectrum of the fluctuating surface pressure observed by Klables [9].....	112
Fig. 5-11	Conceptual configuration of the present HSFV.....	116
Fig. 5-12	Configuration of the sectional grid locations (sectional view).....	117
Fig. 5-13	Shock movement at the inside the inlet (buzz effect) and flow field configuration.....	125
Fig. 5-14	configuration of the FEA grid distribution .....	126

Fig. 5-15 Overall level pressure magnitude RMS (dB, ref=2.0e-5 Pa)	127
Fig. 5-16 Fluctuating surface pressure spectrum on the external surface and inside the inlet	127
Fig. 6-1 Number of “modes in bands” at the equipment bay	133
Fig. 6-2 External depiction of the loads distribution on a HSFV	134
Fig. 6-3 Comparison of the SEA and FEA response prediction results excited by the rocket motor	141
Fig. 6-4 SEA analysis results at the mounting plate during the lift-off (as excited by acoustic loads)	142
Fig. 6-5 SEA prediction results at the mounting plate during lift-off (excited by acoustic loads and by random loads of the rocket motor)	143
Fig. 6-6 FEA prediction results at the mounting plate MP-1 (red) and MP-3 (blue) excited by the aerodynamic pressure fluctuating loads	144
Fig. 6-7 Effectiveness of vibratory response in terms of variation of FSP spectrum in high frequency range	145
Fig. 6-8 Comparison of response analysis results between SEA and FEA on mounting plate 1 (only excited by aerodynamic loads)	146

Fig. B-1	Membership function of the fuzzy sets, $\theta(k)$ and $\gamma(k)$ ...	172
Fig. B-2	Calculation example of Mamdani inference engine .....	172
Fig. B-3	Flowchart of the fuzzy input estimation algorithm.....	173
Fig. C-1	Flowchart of damping estimation procedure .....	175

# **Chapter 1.**

## **Introduction**

### **1.1. Background and Motivation**

High speed flight vehicle, such as launch vehicles and missiles, undergo severe dynamic loads which are generated during the launch and atmospheric flight. Such critical dynamic loads include random vibration, shock, and acoustic loads. It is important to predict such vibratory responses accurately, even at an early stage of the design. These loads provide an important criterion for the principal structural design of the launch vehicle. Critical events responsible for the dynamic loads induced in the launch vehicle include the following: lift-off, atmospheric flight (e.g., static aeroelastic, gust, buffet), engine ignition, shutdown, and separating events [1].

High-speed flight vehicle (HSFV) is an imaginary supersonic flight vehicle with air-breathing inlet. It is launched in a launch canister and flies only in the atmosphere, and which is a significant difference from the space launch vehicles. Such operating conditions induce different dynamic loads on the vehicle, which are acoustic loads in the launch canister and aerodynamic loads during cruise flight and maneuvering. This

this thesis considers those unique situations to estimate acoustic loads, rocket motor shelf-excited loads, and aerodynamic fluctuating loads.

Osborne et al. [2] examined the flight test results of Taurus launch vehicle and found that the payload vibratory response was affected significantly by the acoustic load during lift-off and by aero-acoustic excitation during atmospheric flight than it was by the excitation caused by the burning inside the rocket motor. This suggests that the acoustic load and aero-acoustic excitation together represent a significant dynamic load component for a launch vehicle.

Dotson and Womack [3] showed that for a relatively small launch vehicle with solid rocket motor in stages, the firing of the solid rocket motor would impose a significant spacecraft load that would exceed those induced by flight events.

In those previous examinations, three major excitation sources have been reported: acoustic loads, aerodynamic loads, and rocket motor loads. These factors should be considered for a small-size launch vehicle, such as a high-speed flight vehicle (HSFV).

Jeffrey and Vincent [4] analyzed and modeled the dynamic response of a large composite spacecraft antenna structure subjected to acoustic excitation loads during lift-off. To predict the broad frequency range of the response, different analysis methods were used. In the high frequency range, the statistical energy analysis (SEA) method was used and at the

low frequency to mid-frequency range, and the hybrid FE-SEA method was used to predict the structural response.

Jeffrey and William [5] undertook modelling and analysis for predictions of the structural dynamic responses of the Ares I-X launch vehicle when this vehicle was subject to vibro-acoustic excitation in the form of lift-off acoustics and unsteady aerodynamic pressure fluctuations. A SEA model was used to predict the high frequency ranges of the vehicle.

The general development of launch vehicles and missiles includes estimations of the loads by examining results based on the experience of the previous developments. In the case of a launch vehicle, there are a multitude of investigation results and design specifications regarding dynamic loads. However, for missiles, it is scarce to have relevant load results in the literature because of confidential reason.

MIL-STD-810 [6] is a well-established environmental design specification for military vehicles. It has been used as a general specification for vehicle dynamic loads in early design stage. But it is also known to be rather conservative and is even incapable of specifying the requirements for all the possible flight conditions. Therefore, it should be revised and verified by using the experimental results and analytical predictions during the vehicle development period.

The major objective of this thesis is to propose proper and prompt estimation method which helps to establish design specifications for the

dynamic loads acting on the vehicle in early design stage. And using this method, the excitation loads and vibratory response of high speed flight vehicle, i.e., supersonic flight vehicle with air breathing inlet, is predicted. The dynamic characteristics of this kind of vehicle and the data which can be used to apply general design procedure of dynamic loads are not known much until now.

However, in this thesis, not all of the dynamic load components to be considered at an early design stage of the vehicle during launch events are considered. The acoustic loads and self-excited loads caused by the solid rocket motor during the lift-off event and initial flight (boosting stage) stage, and the load caused by aerodynamic pressure fluctuations during cruising flight are presented. The main engine excitation load is not considered in this thesis due to the complexity of predicting and/or measuring this type of load.

The analytical procedure pertaining to the dynamic loads acting on a HSFV is illustrated in Figure 1-1. At first, various dynamic loads are predicted by using either analytical, numerical or experimental method. Indeed, acoustic load is predicted by semi-empirical method. Aerodynamic pressure fluctuation load is predicted by numerical method. And rocket motor self-excited load is predicted by measurement data from static firing test in this thesis. Next, after reliable dynamic loads are predicted, vibratory responses on the vehicle induced by dynamic loads

will be estimated. To perform this, appropriate structural analysis methods will be investigated by considering large size of analysis model with broad frequency range. And then the predicted dynamic loads will be applied to the SEA and FEA model. Finally, the vibratory responses on the various locations of a vehicle will be predicted by using SEA and FEA method which is the structural analysis method for high frequency ranges.

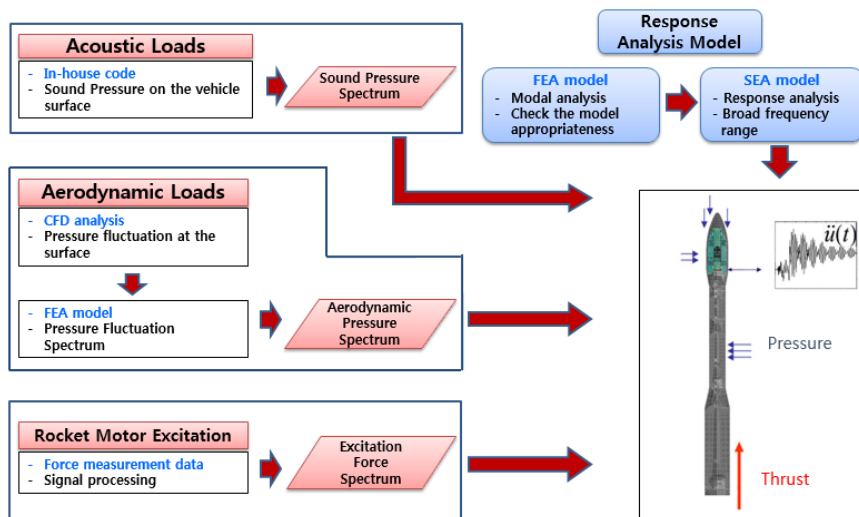


**Fig. 1-1 Analysis procedure of the vibratory loads of a launch vehicle**

## 1.2. Dynamic Loads on a High Speed Flight Vehicle

A HSFV is launched in a launch canister. Subsequently, solid rocket motor accelerates the vehicle to reach the main engine start up speed. The vehicle then separates the rocket motor and ignites the main engine to maintain cruise flight. The launch events of a HSFV are divided into the following three phases: lift-off, boosting, and cruise phase. Within each phase, the vehicle experiences a different set of dynamic loads.

A HSFV launch consists of several series of events, and each of these contains several independent sources of dynamic loads acting on the launch vehicle and electronic equipment. The launch and flight environments generate severe dynamic loads on the hardware; these can be categorized into the following four major excitation sources [7].

- Acoustic pressure excitation generated by the solid rocket motor during launch in the frequency range of 20 to 8,000 Hz.
- Self-induced excitation generated by the solid rocket motor and the sustaining main engine in the frequency range of 20 to 2,000 Hz.
- High-frequency random excitation generated by aerodynamic pressure fluctuations during the atmospheric flight in the frequency range of 20 to 2,000 Hz
- Shock impulsive excitation loads generated by pyro-shocks during separation events: this type of loads provides significant energy

exceeding a frequency of 500 Hz. It is measured from 100 to 10 kHz.

Acoustic loads, rocket motor vibratory loads, and aerodynamic pressure fluctuation loads among the four major excitation sources will be considered in the present thesis.

### **1.2.1. Rocket Motor Vibratory Loads**

Most of all the launch vehicles and missiles contain solid rocket motor as boosting stages. When the rocket motor burns, vortex shedding in the internal flow inside the solid rocket motor can generate self-induced oscillation with regard to the internal pressure in broad band frequency range. Hence, this type of self-induced oscillation in the rocket motor can excite the fuselage mainly in the axial direction. The pressure oscillation frequencies approximately correlate with those of the longitudinal acoustic modes of the solid rocket motor in a phenomenon known as “resonant burning” which affects vehicle in low frequency ranges. Generally, resonant burning for large launch vehicles and their payload structures has not been considered as a critical dynamic load during the design of load cycles for primary structures. However, for relatively small vehicles such as the Taurus launch vehicle or missiles with solid rocket motor, resonant burning can induce significant dynamic loads and thus must be considered [3].

### **1.2.2. Acoustic Vibratory Loads**

A HSFV and its electronic equipment experience severe high-level random acoustic loads during the lift-off. Such severe dynamic loads originate from the acoustic noise due to the rocket motor exhaust gas. The rocket motor jet plume hits the launch pad and is re-directed to the launch vehicle by the plum deflector [8]. These acoustic loads will impinge on the launch vehicle structure and skin. Subsequently, the sound pressure will excite the surface and generate a vibratory response, which is then transferred from the skin to the payload and to the sensitive electronic equipment [9]. The acoustic vibratory load is characterized as random in nature; thus, the resulting mechanical vibrations will be random as well.

The rocket motor create wide-band frequency acoustic noise, and the high-frequency content is particularly intense. Such high-frequency noise will particularly affect the electronic equipment [10, 11].

### **1.2.3. Aerodynamic Fluctuating Pressure Excitation Loads**

Aerodynamic fluctuating pressure was considered as a significant dynamic load during the 1960s, as a series of launch vehicle failures occurred during transonic flights [12].

In general, fluctuating pressures are proportional to the free-stream dynamic pressure ( $q_\infty$ ) for a given unsteady flow. However, the maximum

fluctuating pressure does not always arise at the maximum free-stream dynamic pressure for certain regions which undergo a rapid change of the cross-section due to the non-homogeneous flow field. Regions exposed to separated flow and shock waves will experience higher fluctuating pressures of the magnitude at least ten times bigger than those associated with an attached flow. Accordingly, the flight vehicle geometry is important with regard to aerodynamic fluctuating pressure levels because the air flows are highly correlated with the geometry [13].

In this thesis, an external fluctuating pressure estimation model is developed to estimate the fluctuating pressure time history on the surface of the vehicle using CFD calculations. From the CFD results, the turbulent boundary layer (TBL) parameters are predicted and subsequently, a vibration response in the vehicle can be estimated using VA-ONE [14] which is a commercial vibro-acoustic analysis software.

### **1.3. Analytical Method for the High Frequency Response**

The frequency range for the present predictions of relevant vehicle cannot always be selected accurately, as they depend on the characteristics of the structures, i.e., stiffness, mass distribution, boundary condition, and so on.

Generally, for a large structural component such as an entire launch vehicle, it should be noted that the low frequency range will be from 0 Hz (static) to the first normal mode of the entire structure, i.e., up to approximately 100 Hz. The high frequency range is characterized by the high modal density and high modal overlap, which usually exceeds 400 Hz [7].

Figure 1-2 and Table 1-1 show the dynamic behavior and analysis method for the large scale vehicle, respectively. For the low frequency range, the finite element method (FEM) is capable of predicting the structural responses at appropriate confidence levels. However, for the high frequency range, the prediction accuracy will be degraded as the frequency increases [15]. This is induced by accurate modelling of the structural behavior for the high frequency range by requiring fine structural grids in order to capture short wavelengths. This will cause

accumulation of the numerical discrepancies from the actual response. For a more detailed physical explanation, the number of natural modes of the structure increases sharply as the frequency increases. Those modes can overlap with one another, and the deterministic computational methods, such as FEM and the boundary element method (BEM), cannot predict all of the natural modes precisely. In addition, the physical response will become quite sensitive to structural details such as the boundary conditions [16].

To overcome such limitations of the deterministic method for the high frequency range described above, statistical energy analysis (SEA) has been widely adopted to predict the transient responses of large scale structures such as the space launch vehicles, ships, and high-speed train [17, 18]. However, SEA is not capable of precisely predicting the transient structural responses in the lower frequency range due to its limitations related to theoretical hypotheses [17].

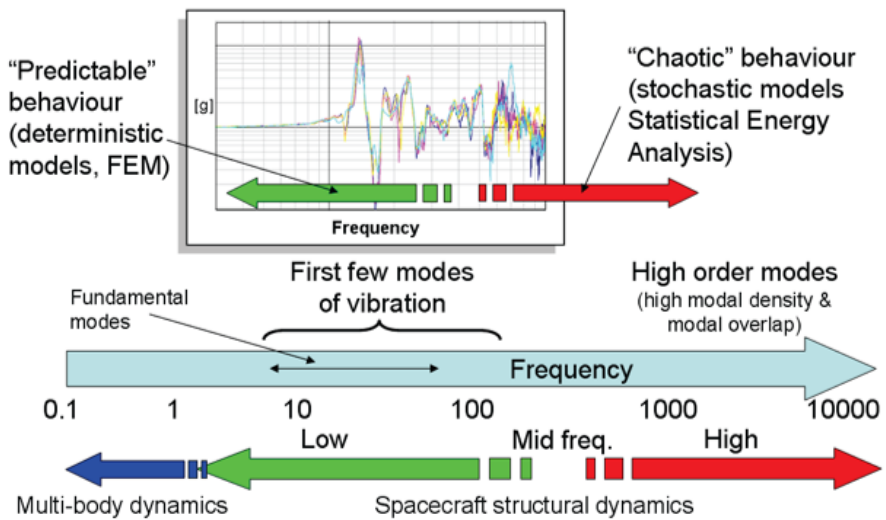


**Fig. 1-2 Dynamic behavior and analysis methodologies in terms of frequency range [7]**

**Table 1-1.** Analysis methodology in terms of frequency range

(full-scale launch vehicle)

<b>Description</b>	<b>Frequency Range</b>	<b>Vibration Type</b>	<b>Analysis Methodology</b>
Low	~ 200	Low Frequency Dynamic Response	FEM, BEM
Mid	200 ~ 400	Random Vibration Acoustic Pressure	Hybrid Method (FEM + SEA)
High	~ 20,000	Random Vibration Acoustic Pressure	SEA

## **1.4. Objectives and Layout of Thesis**

In general, the design procedure of dynamic loads for launch vehicle is based on the data obtained by previous developed vehicle. For general launch vehicles, there exist many design references and data which can be applied to establish design dynamic loads, they are design specification, design guide line and computer programs for predicting dynamic loads on the vehicle (Figure 1-3). However, for the special vehicles such as a supersonic flight vehicle with air breathing inlet in this thesis, it cannot be applied the general design procedure of dynamic loads because there exist only limited data can be used to the design procedure.

The objective of this thesis is to study an analytical estimation methodology which can establish design specification for the dynamic loads acting on the vehicle which cannot be followed general design procedure. And using this methodology, the excitation loads and vibratory responses of the supersonic flight vehicle with air breathing inlet will be predicted. The dynamic characteristics of this kind of vehicle are not known much until now.

The present thesis consists of two parts. One is study for predicting dynamic loads impinging on the vehicle, i.e., acoustic loads, aerodynamic fluctuating pressure loads, and rocket motor self-excited loads. The other is prediction of the structural response excited by dynamic loads for large

scale model and broad frequency ranges.

- a) To investigate the effective structural analysis method for large scale model for the broad frequency ranges, both deterministic and the statistical methods are compared with respect to the advantages and defects by surveying literatures. SEA is chosen as one of the effective analysis methods to predict the response of the structure caused by various dynamic loads for the high frequency range. Details of SEA, i.e., introduction, theoretical background, and advantages and limitation, will be described in Chapter 2.
- b) Prediction method on the acoustic loads considering characteristics of the launch pad will be described in Chapter 3. An improved prediction methodology for the sound pressure level impinging on the surface of the HSFV considering the launch canister effect are suggested based on the semi-empirical method (DSM-II) suggested in NASA SP-8077.
- c) The rocket motor self-excited loads will be investigated in Chapters 3 and 4. The direct measurement results of rocket motor self-excited loads during static firing test will be presented in Chapter 3. And indirect force estimation method using structural responses will be introduced and verified in Chapter 4.

- d) A numerical investigation on the fluctuating surface pressure acting on the external surface and inner wall of air breathing inlet will be presented in Chapter 5. The prediction procedure using CFD and FEA will be introduced and verified by comparing between predictions and semi-empirical model.
- e) The vibratory responses on a HSFV caused by various dynamic loads which are predicted in advance will be investigated in Chapter 6. The comparisons between analysis results by using FEA and SEA will be presented.

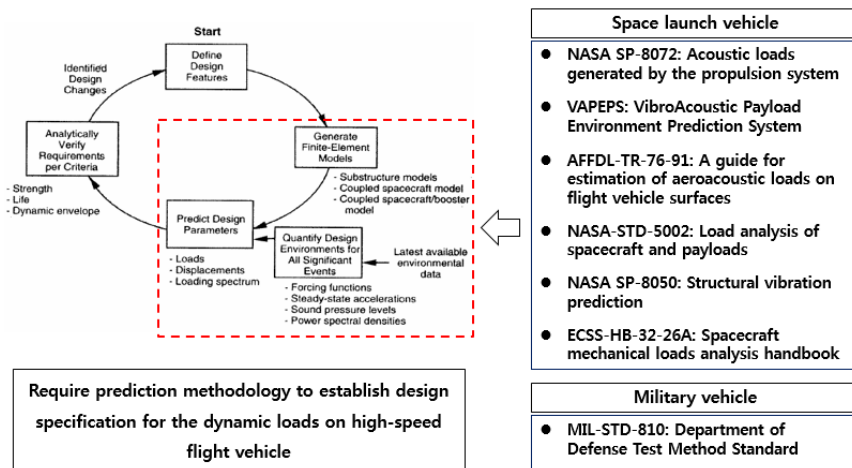


**Fig. 1-3 Design loads estimation procedure**

## **Chapter 2.**

### **Statistical Energy Analysis**

#### **2.1. Brief Historical Background**

Traditional analysis of mechanical vibration of structures have been focused only on a few lower resonant modes because these modes normally have the greater displacement response. However, when fairly large and lightweight aerospace structures are to be designed, broad band high frequency load is important for the purpose of predicting the structural fatigue, equipment failure, and noise [18].

Characteristic of the higher order modal analysis provides the basic uncertainty in the modal parameters. The resonant modes show much sensitivity to small variations of the geometry and material properties. There exists unavoidable uncertainty about structural detail and material properties associated with manufacturing tolerances and imperfections. In addition, the population of the natural modes of a structure significantly increases as the frequency increase. Thus, the dense modal frequencies and modal overlaps in the high frequency range cannot be accurately predicted by the deterministic methods, such as FEM and BEM. Moreover demands increase with geometric and material complexity, and

requirement of the mesh size becomes smaller with increasing frequency. Although today the computational methods are highly developed and optimized, it is not practicable to predict the detailed vibratory behavior at frequencies beyond a few hundreds of Hz using the deterministic methods. For example, the Saturn launch vehicle possesses approximately 500,000 natural frequencies within the range 0 to 2,000 Hz [17, 19].

Considering these unavoidable uncertainties and dense modal populations in high order modal analysis, a statistical model of the modal parameter seems to be proper. Even though it is impossible to predict detailed response behavior of any structure to any specific form of high frequency excitation, it is clear that the gross physical properties determine the ensemble-averaged behavior of a population that shares those properties such as structure geometry and material properties. Figure 2-1 shows for the typical example of uncertainty of high order modes in the room cavity. Modes in the low frequency range can be defined identically. On the other hand those in high frequency range can be defined in the statistical way rather than those are in the deterministic way because of uncertainty of mode population. The statistical energy analysis (SEA) method is known to be representative statistical method for the high frequency vibration and acoustic problems. It gives more accurate predictions in the high frequency range. Lee et al. [20] presented the method for pyro-shock prediction using an empirical model and SEA in

conjunction with virtual mode synthesis to predict shock response of a low altitude earth observation satellite.

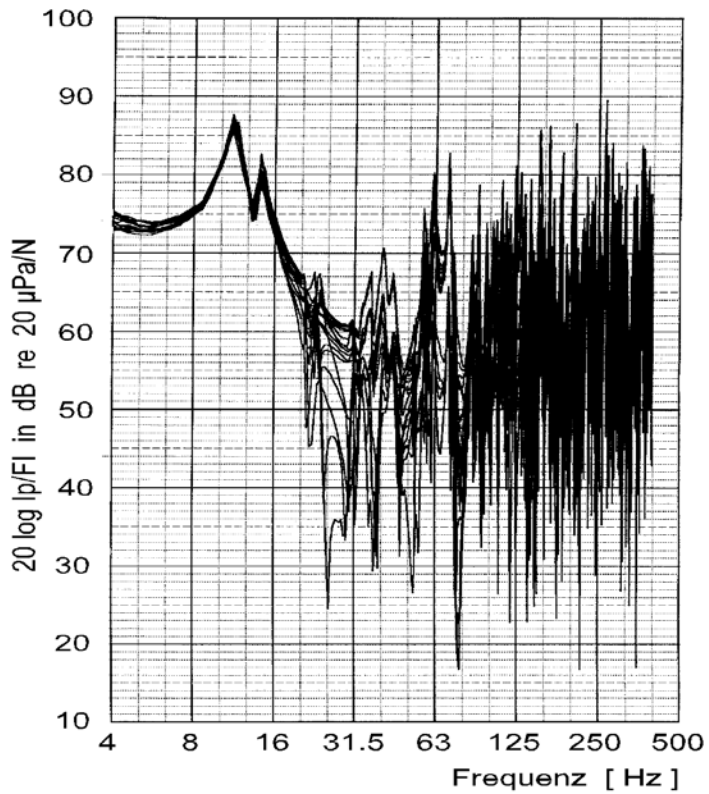


**Fig. 2-1 Characteristic of the natural frequency uncertainty in high order modes (FRF of acoustic pressure measured in the room)**

## **2.2. Theoretical Background**

### **2.2.1. Power Balance Equation**

Theoretical development of SEA is based on the average power flow between two coupled groups of natural modes. It is proportional to the difference in the average modal energies. SEA model has a few particular assumptions as follows:

- ① Each mode in subsystems is assumed to have a natural frequency that is uniformly probable over a frequency band.
- ② Every mode in a subsystem is assumed to be equally energetic and modal displacements are assumed to be incoherent.
- ③ The damping of each mode in a subsystem assumed to be the same. It simplifies the formulation and tends to be approximately true for the complex system.

SEA can be used in order for enhanced accuracy in situations in which there exist sufficient number of modes in a subsystem because increased number of modes provide improved statistics in general. In SEA application, it is recommended that to ensure enhanced accuracy of the SEA computation it should use more than three modes in band in a subsystem.

The complex system may be subdivided into a number of groups (subsystems) having similar modes (such as, flexural, in-plane, acoustical,

and so on) in the system. And considering a power balance equation of the form which govern response of a system in a given frequency band:

$$\Pi_{in} = \Pi_{out} \quad (2-1)$$

Power flows out of a subsystem through dissipation or transmission to another subsystem.

$$\Pi_{out} = \Pi_{transmitted} + \Pi_{dissipated} \quad (2-2)$$

The schematic of two coupled systems is shown in Figure 2-2, where  $\Pi_{in,1}$  and  $\Pi_{in,2}$  are the input power from external sources,  $\Pi_{diss,1}$  and  $\Pi_{diss,2}$  are the dissipated power in the subsystem, and  $\Pi_{coupling,12}$  represents the transmitted power flow from Subsystem 1 to Subsystem 2.

The transmitted power can be represented as follows:

$$\Pi_{coupling,12} = \omega \eta_{12} n_1 \left( \frac{E_1}{n_1} - \frac{E_2}{n_2} \right), \text{ and}$$

$$\Pi_{coupling,21} = \omega \eta_{21} n_2 \left( \frac{E_2}{n_2} - \frac{E_1}{n_1} \right) \quad (2-3)$$

where  $n_i$  is the modal density in Subsystem  $i$ ,  $\eta_{12}$  is the coupling loss factor from Subsystem 1 to 2 and  $E_1$  is the total dynamic energy of the subsystem modes at frequency  $\omega$ .

The dissipated power in Subsystem 1 can be evaluated by

$$\Pi_{diss,1} = \omega \eta_1 E_1 \quad (2-4)$$

where  $\eta_1$  is the damping loss factor.

The power balance equation for the two subsystems can be derived as

$$\begin{aligned} \Pi_{in,1} &= \Pi_{diss,1} + \Pi_{coupling,12} = \omega(\eta_1 + \eta_{12})E_1 - \omega\eta_{21}E_2 \\ \Pi_{in,2} &= \Pi_{diss,2} + \Pi_{coupling,21} = \omega(\eta_2 + \eta_{21})E_2 - \omega\eta_{12}E_1 \end{aligned} \quad (2-5)$$

It can be rewritten by a matrix form as

$$\begin{Bmatrix} \Pi_{in,1} \\ 0 \end{Bmatrix} = \omega \begin{bmatrix} (\eta_1 + \eta_{12}) & -\eta_{12} \\ -\eta_{21} & (\eta_2 + \eta_{21}) \end{bmatrix} \begin{Bmatrix} E_1 \\ E_2 \end{Bmatrix} \quad (2-6)$$

In this matrix form,  $\Pi_{in,2} = 0$  (see, Figure 2-2) and coupling loss factors are not symmetric but using the reciprocity relationship ( $n_1\eta_{12} = n_2\eta_{21}$ ) it can be re-written as a symmetric form.

$$\begin{Bmatrix} \Pi_{in,1} \\ 0 \end{Bmatrix} = \omega \begin{bmatrix} n_1(\eta_1 + \eta_{12}) & -\eta_{12}n_1 \\ -\eta_{21}n_2 & n_2(\eta_2 + \eta_{21}) \end{bmatrix} \begin{Bmatrix} E_1/n_1 \\ E_2/n_2 \end{Bmatrix} \quad (2-7)$$

This implies that power flow reciprocity will be valid only in the condition of the subsystem modal energy and will not be the amount of the total energy.

The general form of  $N^{\text{th}}$  number of the subsystem then becomes

$$\begin{Bmatrix} \Pi_{in,1} \\ \Pi_{in,2} \\ \vdots \\ \Pi_{in,N} \end{Bmatrix} = \omega \begin{bmatrix} (\eta_1 + \sum_{i=1, i \neq 1}^N \eta_{1i}) n_1 & -\eta_{12} n_1 & \cdots & -\eta_{1N} n_1 \\ -\eta_{21} n_2 & (\eta_2 + \sum_{i=1, i \neq 2}^N \eta_{2i}) n_2 & \cdots & -\eta_{2N} n_2 \\ \vdots & \vdots & \ddots & \vdots \\ -\eta_{N1} n_N & -\eta_{N2} n_N & \cdots & (\eta_N + \sum_{i=1, i \neq N}^N \eta_{Ni}) n_N \end{bmatrix} \begin{Bmatrix} \frac{E_1}{n_1} \\ \frac{E_2}{n_2} \\ \vdots \\ \frac{E_N}{n_N} \end{Bmatrix} \quad (2-8)$$

In this power balance equation, energy (E) in each subsystem is an unknown parameter and it can be obtained by inverting loss factor matrix. The input power vector and loss factor matrix are known or assumed parameters in this case. In general, the coupling loss factors can be estimated using an analytical method. Those have been presented by many studies but damping loss factors has usually been obtained by measurement or assumption.

Averaged responses such as displacement, vibration, acceleration in structure and sound pressure level in acoustic cavity can be calculated from subsystem energies.

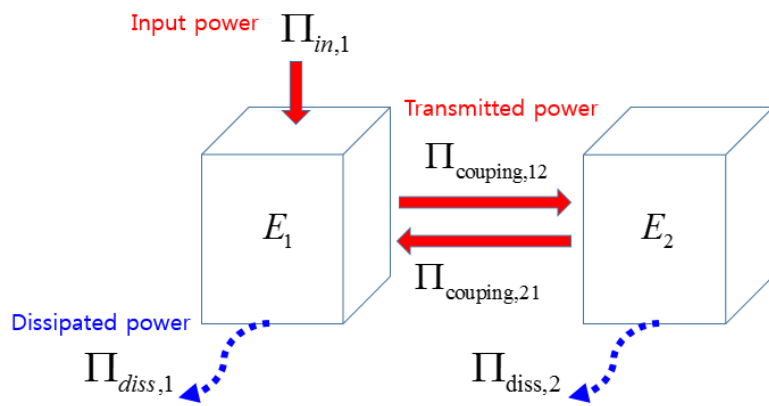


**Fig. 2-2 Schematic of SEA model**

### **2.2.2. Definition of SEA Parameters**

SEA is a statistical analysis method of the energy in the dynamical system. This statistical nature of SEA enables a complex system to be modeled with fewer degrees of freedom than it is needed in a deterministic method.

The SEA procedure consists of three steps as follows:

- ① Define the subsystem,
- ② Evaluate the SEA parameters,
- ③ Evaluate the response variables.

### **Definition of the Subsystems**

A subsystem is a group of similar modes (such as flexural, in-plane, acoustical and so on) that are capable of storing, transmitting, and dissipating of energy. In selecting the subsystem, it meets the criteria of similarity and significance. Similarity means that the modes of the subsystem have nearly equal excitation, coupling, and damping. And significance means that the modes of the subsystem play an importance role in the storing, transmission, and dissipation of energy. The groups of similar modes in each physical component are identified as those having resonant frequencies in a frequency band and having similar modes shape.

### Definition of the Mode Count

The mode count is an important parameter in SEA and it represents the number of resonance modes in a subsystem. The mode count can be represented by three forms such as:

- ① The number of modes in a frequency band,  $N$  or  $\Delta N$
- ② The modal density,  $n(\omega) = dN / d\omega$
- ③ The average spacing frequency between modes,

$$\delta \bar{f} = 1 / [2\pi n(\omega)] \quad (2-9)$$

Among these representation forms, the modal density is a representative form used often in the theoretical development of SEA calculation.

The modal density defines the number of modes per unit frequency band. In general, SEA is known to be more accurate as the modal density increases. It can be calculated by analytical method. Table 2-1 represents the calculated frequency spacing and modal density of a simple configuration. It is calculated based on the wave equation. The modal density can be expressed by geometry, material properties and group speed ( $c_g$ ).

One-dimensional subsystem:

$$n(\omega)^{1D} = \frac{dN}{d\omega} = \frac{L}{\pi c_g} \quad (2-10)$$

Two-dimensional subsystem:

$$n(\omega)^{1D} = \frac{dN}{d\omega} \approx \frac{A\omega}{2\pi c_g c_\phi} + \Gamma'_{BC} P \quad (2-11)$$

where  $c_g = \frac{dk}{d\omega} = \frac{1}{c_\phi} \left( 1 - \frac{\omega}{c_\phi} \frac{dc_\phi}{d\omega} \right)$ : group speed,

$k = \frac{\omega}{c_\phi}$ : wave number, and  $c_\phi$ : phase speed

The group speed is a key parameter in the modal density calculation. It is the same as the phase speed for non-dispersive wave type such as air. However, for general materials it is different from each other. The group speed is also represented in Table 2-1.

**Table 2-1** Modal density of the basic subsystems [14, 21]

Subsystem		Mode	Modal density	Sound speed
1 D	Bar	Longitudinal	$\frac{L}{\pi c_L}$	$c_L = \sqrt{\frac{E}{\rho}}$
		Torsional	$\frac{L}{\pi c_T}$	$c_T = \sqrt{\frac{JG}{\rho I_p}}$
	Beam	Flexure	$\frac{L}{2\pi c_B}$	$c_B = \sqrt{\omega \kappa c_L}$
		Flexure with shear	$\frac{L \left( \frac{1}{c_B^2} + \frac{2}{c_\gamma^2} \right)}{2\pi \sqrt{\frac{1}{c_B^2} + \frac{1}{c_\gamma^2}}}$	$c_B = \sqrt{\omega \kappa c_L}$ $c_\gamma = \sqrt{\frac{G}{\rho \gamma}}$
2 D	Plate	In-plane extension	$\frac{\omega A}{2\pi \kappa c_L^2}$	$c_L = \sqrt{\frac{E}{\rho(1-\nu^2)}}$
		In-plane shear	$\frac{\omega A}{2\pi \kappa c_s^2}$	$c_L = \sqrt{\frac{G}{\rho}}$
		Flexural	$\frac{A}{4\pi \kappa c_L}$	$c_L = \sqrt{\frac{E}{\rho(1-\nu^2)}}$
		Flexural with shear	$\frac{\omega A \left( \frac{1}{c_B^2} + \frac{2}{c_\gamma^2} \right)}{4\pi \kappa c_L}$	$c_B = \sqrt{\omega \kappa c_L}$ $c_\gamma = \sqrt{\frac{G}{\rho \gamma}}$

### Definition of Coupling Loss Factor

The coupling loss factor (CLF) is a key parameter of SEA. It is based on the assumption that the average power flow coupled between each subsystem is proportional to the difference in the average modal energies of mode groups similar to heat transfer. The CLF can be evaluated by either theoretical, numerical, or experimental method. It can be idealized point junction (Figure 2-3 (a)), line junction (Figure 2-3 (b)), and area junction (Figure 2-3 (c)) [14, 22, 23].

The power flow between the modes of two coupled subsystems is given as

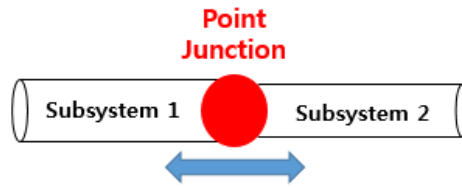
$$\Pi_{12} = \omega(\eta_{12}E_1 - \eta_{21}E_2) \quad (2-12)$$

And an alternative form of the power flow equation is

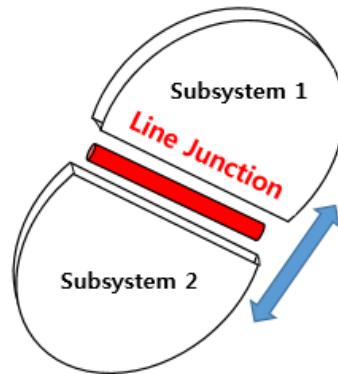
$$\Pi_{12} = \beta_{12} \left( \frac{E_1}{n(\omega_1)} - \frac{E_2}{n(\omega_2)} \right) \quad (2-13)$$

where  $\beta_{12} = \omega\eta_{12}n(\omega_1)$ , modal coupling factor

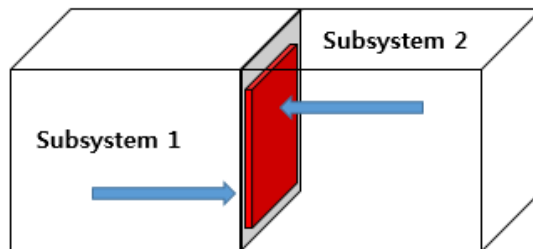
Because of the reciprocal relation ( $\beta_{12} = \beta_{21}$ ), the modal coupling factor are symmetrical, which enforces the relevant process simple.



(a) Point Junction



(b) Line Junction



(c) Area Junction

**Fig. 2-3 Illustration of the junction type [14]**

The junction can be calculated theoretically by the modal and wave approaches. Both approaches are useful, but the wave approach is usually preferred because it is easier than the modal approach is. The direct evaluation of the CLF is sometimes difficult because of the need to implement complex integrations between the subsystems. On the other hand, calculation of the junction for the semi-infinite systems can be used to indirectly evaluate the CLF by using theoretical work in the literature.

① Point connected subsystems

Energy transmission in Subsystem 1 to 2:

$$\Pi_{1 \rightarrow 2} \equiv \omega \eta_{12} E_1 \quad (2-15)$$

Power transmission coefficient:

$$\tau_{12} = \frac{\Pi_{tra}}{\Pi_{inc}} = \frac{4R_1 R_2}{|Z_1 + Z_2|^2} \quad (2-16)$$

where  $Z$  is the semi-infinite input impedance of the subsystem, and  $R$  represents the real part of the impedance.

② Line connected subsystem

$$\eta_{12} = \frac{\overline{\delta f_1}}{\pi f} \beta_{corr} I_{12} \frac{\tau_{12}(0)}{2 - \tau_{12}(0)} \quad (2-17)$$

$$\tau_{12}(0) = \frac{4R'_1 R'_2}{|Z'_1 + Z'_2|^2} \quad (2-18)$$

③ Area connected subsystem (structure-acoustic area coupling)

$$\eta_{12} = \frac{\rho_0 c_0}{\omega \rho_p h_p} \sigma_{rad} \quad (2-19)$$

where  $\sigma_{rad}$  is the radiation efficiency of a structure.

### **Definition of the Damping Loss Factor**

Damping loss factor (DLF) is an important parameter for dynamic analysis, including SEA. It is inversely proportional to the overall response level.

$$\Pi_{in} = \Pi_{diss} = \omega \eta E_{tot}$$

where  $\eta$  is damping loss factor

In many cases, damping can be evaluated only by an experimental method because it is difficult to define analytically due to its nonlinear characteristics. The most commonly used method for experimental determination of the DLFs is the “decay rate method” and the “half-power bandwidth method.” Neither method will be applicable for all the situations, and thus it is important to understand the characteristics of each method. In general, almost all the analytical damping estimation and measurement will be approximate within accuracy greater than 20% [18].

The decay rate method is based on the transient response in time domain. Since the energy  $E$  is proportional to the square of the peak amplitude  $C$ , the decay rate of the response will be  $C \approx e^{-\pi f \eta t}$ . At time interval,  $t_1$  and  $t_2$ , the amplitude decay will be described as:

$$20 \log_{10} \left( \frac{C_1}{C_2} \right) = 27.3 f \eta (t_2 - t_1) \quad (2-20)$$

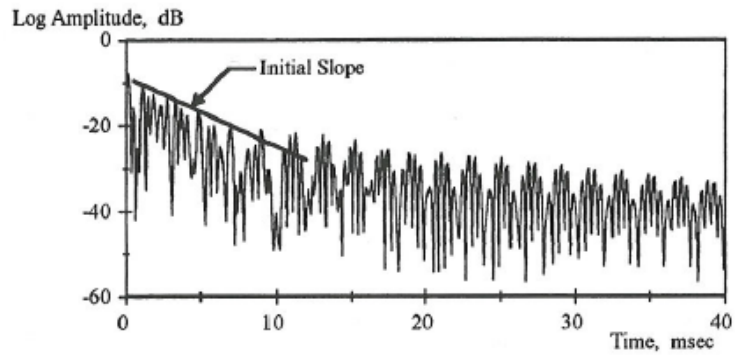
from Eq. 2-20, the DLF can be defined as

$$\eta = \frac{DR}{27.3 f} \quad (2-21)$$

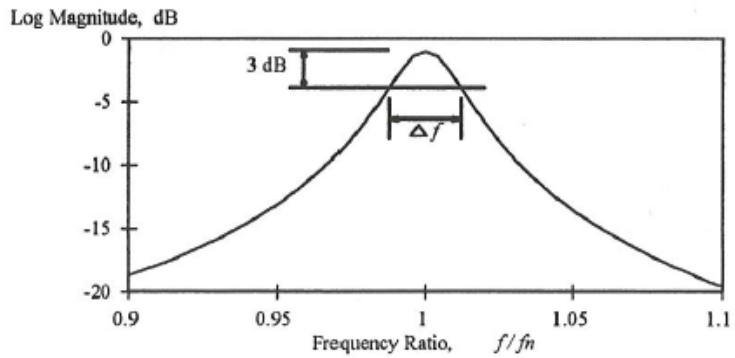
where DR is a decay rate defined as the slop of the decay in unit of dB/sec, (Figure 2-4 (a))

$$DR = \frac{20 \log_{10} (C_1 / C_2)}{t_2 - t_1}$$

In general, the DR can be easily defined by using the log-rms amplitude vs. linear time plot, as Figure 2-4 (a). The initial decay straight line means a constant value of DLF in this plot.



(a) Decay rate method (Log-rms vs. Time)



(b) Modal bandwidth method (frequency response function)

**Fig. 2-4 Experimental method for defining damping [18]**

**Modal bandwidth method** is based on the bandwidth of resonance in the frequency response function. It can be defined by the half-power bandwidth in a single mode. The half-power bandwidth can be defined the frequency spacing ( $\Delta f$ ) between the two amplitude which are 3 dB lower from the peak amplitude (Figure 2-4 (b)). The DLF is described as:

$$\eta = \frac{\Delta f}{f_n} \quad (2-22)$$

where  $f_n$  is the resonance frequency.

#### **Empirical Damping Values**

Predicting a DLF using experimental method is difficult and a time-consuming task, and generally, it is also difficult to be performed in a small laboratory. Lyon [18] suggested certain procedures for evaluating the damping loss factor. He suggested that an empirical damping value can be used when either measured or theoretical damping values are not available. It is estimated based on the measured values for similar subsystems. Figure 2-5 shows the empirical damping loss factor for typical subsystems.

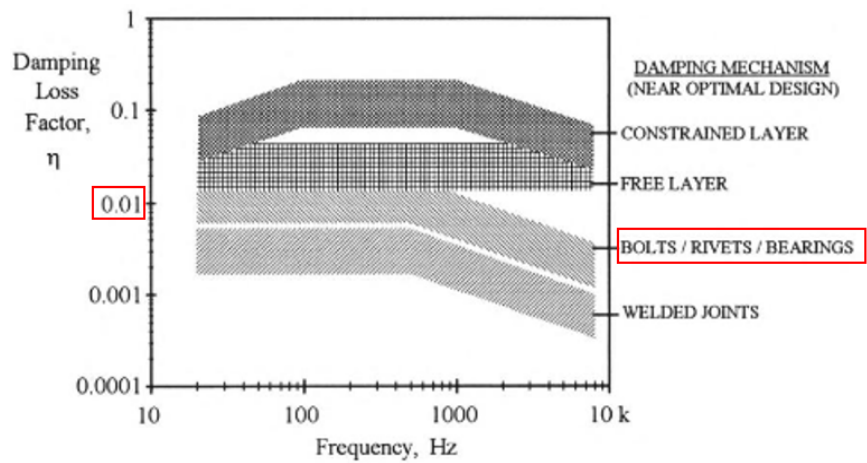


**Fig. 2-5 Empirical damping loss factor for steel and aluminum thin plates and shells in the size range of 0.1 – 10 m [18]**

### **2.3. Advantages and Limitations**

SEA addresses the problem in which it is no longer possible to predict the exact behavior because of uncertainty in the analysis model and limitation of the deterministic analysis methods especially for high frequency range. It can predict the average performance using the statistical way.

The significant advantage of SEA is the ability to simplify a complex system. It requires only a few idealization of the physical system that possesses relatively few gross parameters and uses the decreased number of degrees of freedom per system [21]. Though SEA consists of small set of the modal subsystems and applying power balance relationships between them, it can derive in a set of linear algebraic equation which has substantially reduced number of degrees of freedom when compared to the deterministic methods. Therefore, computational time and expense are quick and cheap, respectively.

Statistical approach is not only a main advantage of SEA but also one of disadvantage. If the number of ‘modes in band’ exists relatively small in the relevant subsystem in SEA, it can cause significant error in SEA calculation. Generally, the prediction error is a function of modal overlap [17, 24]. A small average of modal overlap usually corresponds to large values of prediction error. In the low frequency bands where the

wavelengths are larger than or comparable with the surface dimension of SEA subsystem, it cannot be ensured the confidence of prediction results. As the frequency increases, the bandwidth of analysis will become larger and the number of 'modes in band' will increase enough to ensure the confidence of SEA results. It is generally recommended that the number of 'modes in band' will be greater than three 'modes in band' in a frequency band in order to have a confidence of the SEA results.

## **Chapter 3.**

# **Dynamic Loads on the High Speed Flight Vehicle during Launch Events**

### **3.1. Acoustic Loads on the Launch Pad**

HSFV is launched from inner space of the launch canister which is different from the space launch vehicle. The launch canister affects the acoustic load impinging on the vehicle. This thesis suggests an improved prediction methodology for the sound pressure level (SPL) impinging on the surface of a HSFV which includes the launch canister effect, the screen effect, and the reflection effect based on the suggestions in NASA SP-8072 (Figure 3-1).

The rocket motor exhaust stream mixed with the ambient atmosphere will induce strong sound pressure into the atmosphere. This sound pressure will impinge on the surface of the HSFV. The magnitude of the resulting acoustic loads will be a function of the following parameters: the rocket nozzle geometry, the shape of the launch pad, the shape of the exhaust plume, and the launch speed of the vehicle [9, 25, 26].

To predict the acoustic loads existing on the surface of the HSFV considering the launch pad, an improved empirical estimation method was

developed based on the DSM-II (Distributed Source Method-II) in NASA SP-8072 [25], which suggested an empirical estimation method for the launch vehicle. Figure 3-1 (a) shows an illustration of the rocket exhaust flow and the contour of the overall sound pressure level (OASPL) for the launch situation.

Overall acoustic power radiated by jet is determined as:

$$W_{OA} = \eta \left( \frac{1}{2} \dot{m} U_e^2 \right) = 0.005 F U_e. \quad (5)$$

where

$W_{OA}$  is the overall acoustic power,  $F$  is the thrust of each engine,

$U_e$  is the fully expanded exit velocity

Propagation of the sound from the distributed sources is estimated by the geometric relationship between the noise sources and receiver. Finally, the acoustic loads on the surface of vehicle are predicted to be logarithmic summation of contributions from each of the slices from:

$$SPL_{b,p} = 10 \log \sum_s \text{anti log} \frac{SPL_{s,b,p}}{10}. \quad (6)$$

where

$SPL_{s,b,p}$  is the sound pressure level in each frequency band at each point, p, in each slice

$SPL_{b,p}$  is the total SPL in the frequency band  $b$  at any point  $p$

The methodology suggested in NASA SP-8072 can estimate the acoustic pressure to a precision level of  $\pm 4$  dB.

Differing from other general launch vehicles, the HSFV is launched in a launch canister and exhibits the following two unique phenomena (Figure 3-1 (b)). The first is the “screen effect,” reducing the SPL impinging on the vehicle because the launch canister acts as a screen to reduce the acoustic pressure from the rocket motor. The second is the “reflection effect,” which increases the SPL because the launch canister acts as a reflector for the acoustic pressure, such as when the sound source is located in the canister. Figure 3-1 (b) shows an analysis of a configuration using the present improved method. In this figure, the HSFV is fired from the inside of a tilted canister and has a deflector for the rocket plume at the rear of the aft canister such that it deflects the rocket motor exhaust stream. The blue line represents the launch canister. Each of the green dots represents a sound source on the jet plume, and the red dots represent the location of the sound source when applying the reflection effect in the canister. The station number represents the locations of the receivers at which the SPL is estimated.

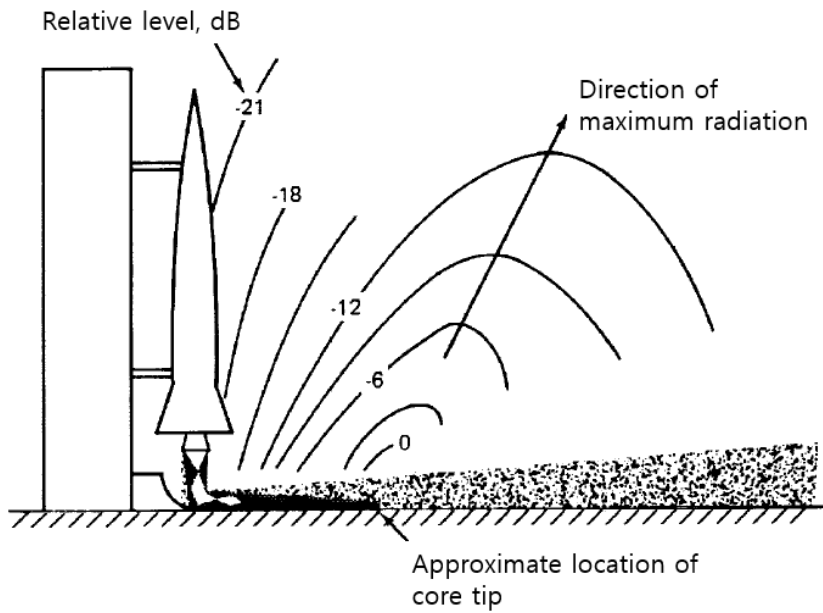
Park et al. [27] showed details pertaining to the analytical prediction method of the acoustic loads experienced by a HSFV as utilized in this

thesis.

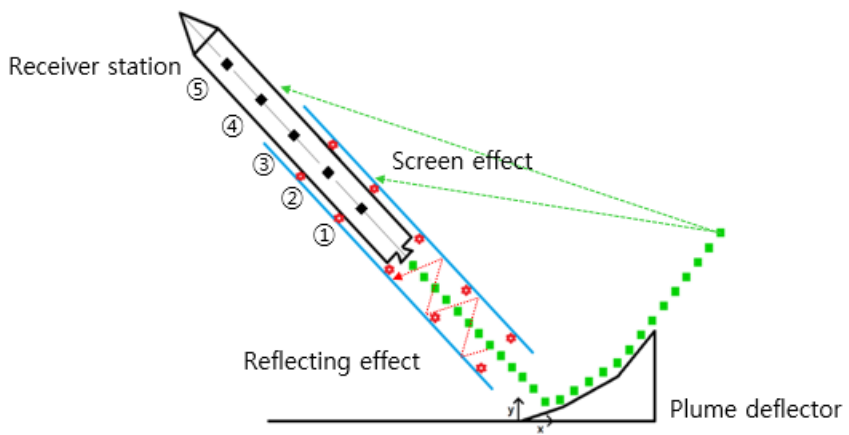
Figures 3-2 and 3-3 show the predicted results in terms of the SPL regarding the vehicle flight altitude at five locations of the HSFV surface in the axial direction of the vehicle.

Figure 3-2 shows the OASPL results on the surface of the vehicle with respect to the flight altitude of the vehicle. Each station is a sensor location (Figure 3-1 (b)). Station 1 is the location of the closest sensor to the rocket motor, and Station 5 is the sensor farthest from the rocket motor. OASPL on the surface of the vehicle varies with respect to the location of the sensors from the rocket motor; it also depends on whether or not the sensor is located in the canister due to both the screen and the reflection effect. It was found that the maximum OASPL value on the surface of the vehicle will occur when the flight altitude of the vehicle is 6 m.

Figure 3-3 shows the distribution of the SPL with respect to the frequency at a fixed flight altitude of vehicle. At zero altitude (Figure 3-3 (a)), the results appear as a smooth line because there exists only the screen effect of the canister. However, at an altitude of 6 m (Figure 3-3 (b)), the result appears as a roughly shaped line due to both effects, i.e., the screen effect and the reflection effect of the canister. According to the reflection effect, the resulting OASPL was increased by approximately 3 dB [27].



(a) Concept of the empirical method by DSM-II (NASA SP-8072 [25])



(b) Present analysis configuration by DSM-II

**Fig. 3-1 Illustration of the acoustic source locations and propagation**

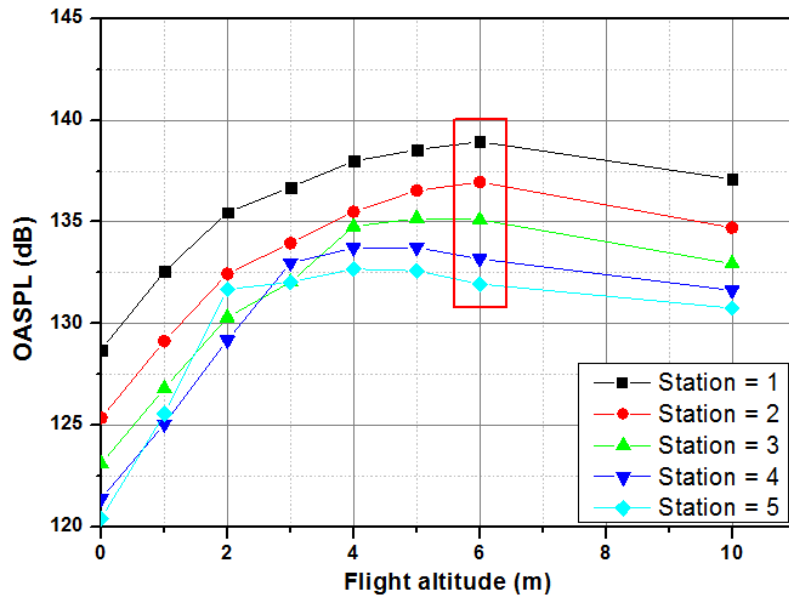
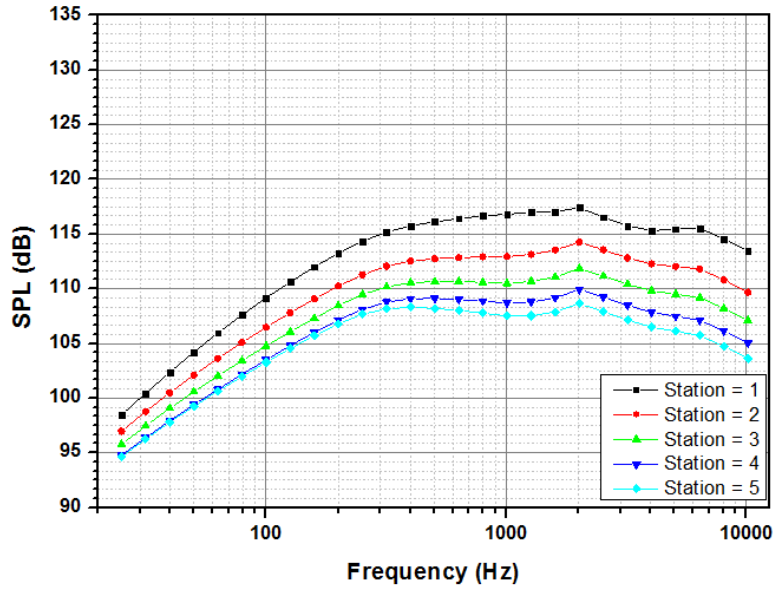
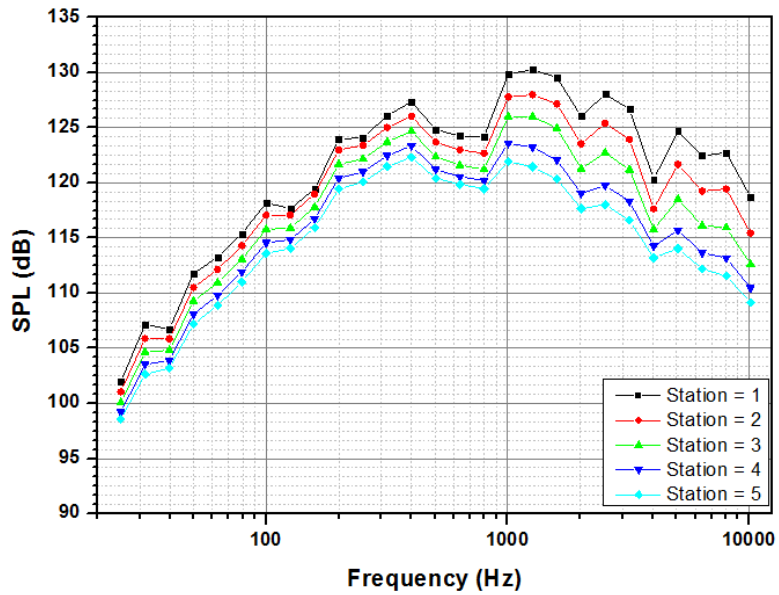


**Fig. 3-2 Overall sound pressure level at each station with respect to the altitude of the vehicle**



(a) Flight altitude 0 m



(b) Flight altitude 6 m

**Fig. 3-3 Sound pressure level at each position on the surface in terms of the frequency at a fixed**

## **3.2. Rocket Motor Vibratory Load**

### **3.2.1. Rocket Motor Self-Excited Vibration**

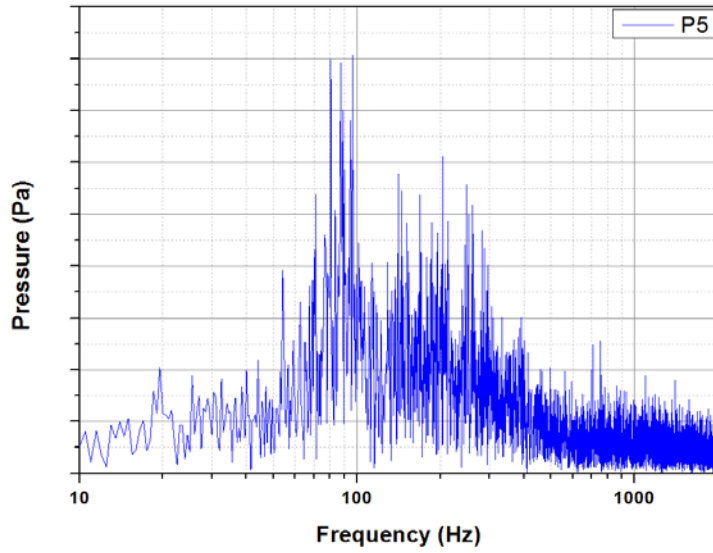
During rocket motor combustion, the shedding of vortices in the internal flow of the solid rocket motors can generate self-induced oscillations in the internal pressure. Hence, vortex induced thrust oscillations excite the hole launch vehicle system particularly in the axial direction. The thrust oscillation frequencies broadly coincide with those of the longitudinal acoustic modes of the solid rocket motor, and the phenomenon is commonly called “resonant burning” [3].

Generally, the critical loads for medium and heavy lift launch vehicles are identified by lift-off, atmospheric flight, engine ignitions and shutdowns, and stage separation events. In other words, although resonant burning occurs for medium and heavy lift vehicles with solid rocket motors as stages, it has not been a critical design loads for primary structure. However, for small-sized launch vehicles with solid rocket motors as stages, resonant burning can produce critical dynamic loads. The rocket motor self-excited vibration, also known as “resonant burning,” has characteristics such that the excitation frequency varies with respect to the size of the rocket motor. It was reported that the Peacekeeper rocket motor applied to the Taurus launch vehicle showed a natural frequency of

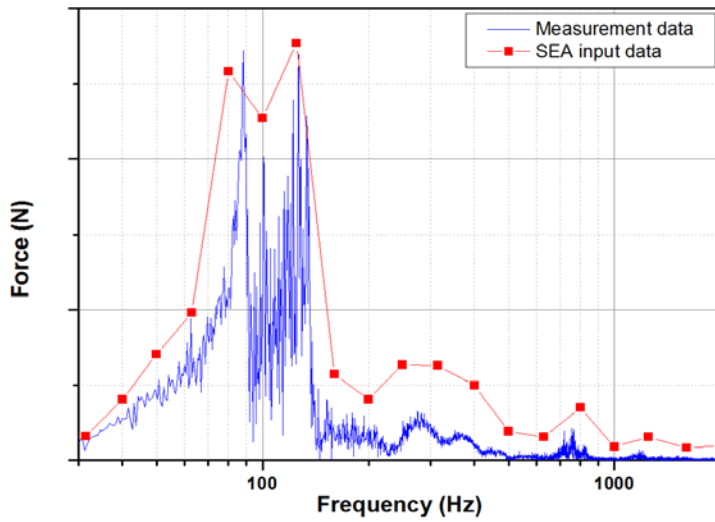
70 Hz in the axial direction [3]. Thus, launch vehicles smaller than Taurus are expected to have higher excitation frequencies as compared to that of Peacekeeper [28].

A HSFV is a small-sized flight vehicle compared to space-launch vehicles, and it has a single solid rocket motors assigned to the longitudinal axis of the vehicle hence the resonant burning should be considered as a major dynamic loads for designing structure.

The rocket motor thrust and acoustic pressure were measured during a static firing test, and the measurement sampling frequency were 10 kHz and 20 kHz, respectively. The frequency spectrum of the rocket motor was estimated using a fast Fourier transform (FFT) algorithm for the measurement results. From the thrust and acoustic measurement results as determined during the static firing test, resonant burning was observed. Figure 3-4 shows a comparison of the frequencies of the rocket motor acoustic pressure (Figure 3-4 (a)) and thrust (Figure 3-4 (b)). The dominant frequencies are very similar to each other. These frequencies are between 80 to 120 Hz. Thus, it can be regarded as a resonant burning. The red line in the thrust spectrum describes the input exciting force in the present SEA analysis model.



a) Frequency spectrum of the acoustic pressure



b) Frequency spectrum of the thrust

**Fig. 3-4 Rocket motor excitation loads and acoustic pressure measurements from the static firing test**

### **3.2.2. Overview of Input Force Estimation**

In general, predicting or measuring a rocket motor self-excited loads acting on the vehicle are not feasible during vehicle flight. However obtain structural responses (i.e. displacement, acceleration) which is excited by rocket motor loads are easier than direct measurement of forces during vehicle flight. As a results, to predict rocket motor self-excited force using structural response, an indirect estimation for excitation forces in terms of measured dynamic responses is proposed in this thesis. Many researchers have studied input force estimation method by an inverse method, such as sum of weighted accelerations technique (SWAT), pseudo-inverse method and Kalman filter method [29-31]. The method based on the Kalman filter and a recursive least-squares algorithm is one of the effective method among many different indirect methods [30].

In present thesis, an introduction, numerical formulation, and verification of the Kalman filter method are described in chapter 4.

Actually, input force estimation method is not used in this thesis because of lack of measured response on the vehicle. Instead, the rocket motor self-excited forces measured by load-cell at static firing test (see, section 3.2.1) are used as an excitation loads for response analysis model.

### **3.3. Aerodynamic Fluctuating Surface Pressure Excitation Loads**

Before the vibration response of a structure excited by fluctuating pressure flow fields is predicted, the fluctuating pressure loads impinging on the surface should be defined. The key parameters for the definition of the fluctuating pressure loads are (a) the overall pressure level, (b) the power spectrum, and (c) the narrow-band spatial correlation coefficients along and across the axis of the structure [13]. After these parameters are defined, the vibration response can be computed using SEA or a modal superposition method of the FEM.

To define the parameters of the fluctuating pressure, a CFD (computational fluid dynamics) analysis was conducted using FLUENT. From the CFD results, the TBL (turbulent boundary layer) parameters could be defined using VA-ONE. Figure 3-5 shows the procedure used to define the fluctuating surface pressure and TBL parameters.

A CFD analysis was performed using FLUENT for HSFV during the cruise flight condition.

The pressure time history at each grid point was exported to the CGNS (CFD General Notation System) file format together with the geometry data from FLUENT analysis results. VA-ONE then imported the pressure

time history to the relevant FEM grid and calculated the frequency spectrum in the subsystems using FFT.

From the procedure used to define the TBL parameters (Figure 3-5), the average fluctuating pressure spectrum and the TBL parameters could be calculated using VA-ONE for the SEA subsystems.

Blanchet et al. [32] and Shorter et al. [33] presented the prediction method of vehicle interior noise caused by vehicle's external wind flow and it is implemented by using the prediction procedure, as shown in Figure 3-5.

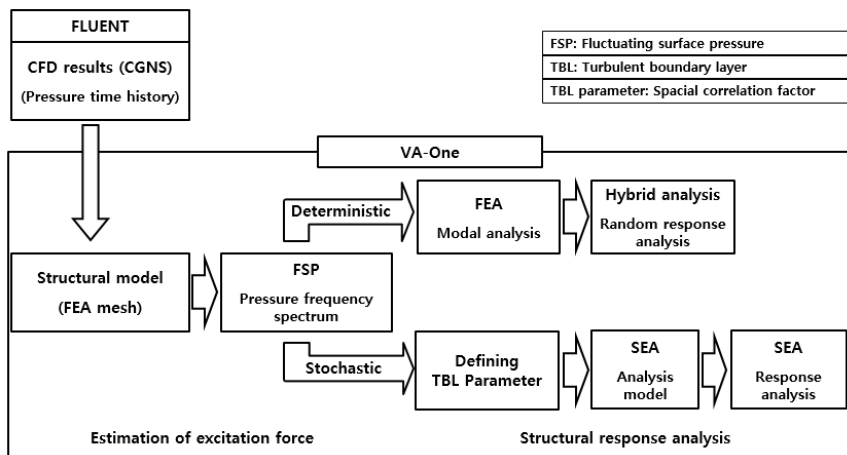


**Fig. 3-5 Procedure for defining the TBL parameters using VA-ONE**

## **Chapter 4.**

# **Input Force Estimation Method to Predict the Rocket Motor Self-Excited Loads**

### **4.1. Introduction**

Determination of the external excitation forces will be one of the most important tasks in structural design. However direct measurement of such loads will often not be feasible due to many limitations such as practical instrumentation difficulties of the force transducer and difficulties of identification of forces transferred from the complex interaction between each adjacent structure. Hence, an alternative indirect estimation method is needed to reconstruct input excitation forces based on the measurement of the structural responses (such as, displacement, velocity, and acceleration).

The inverse estimation method to identify input forces has been studied by many researchers. It can be categorized as the method using finite element analysis (FEA), Kalman filter [34], and sum of weighted acceleration technique (SWAT) [29].

In this thesis, to predict the rocket motor excitation load impinge on an HSFV, an input force identification method by using Kalman filter and

recursive least square method (LSM) [35] is studied.

Tuan et al. [36] presented an input estimation approach based on the Kalman filter technique to estimate the unknown heat flux input on the two boundaries in real time. Ma et al. [37] demonstrated the input force estimation by numerical simulation consisted Kalman filter and recursive LSM, in which impulsive loads acting on multi-degree of lumped-mass systems. Ma et al. [38, 39] presented an on-line recursive inverse method to estimate the input forces of beam structures which were constructed using the finite element method. Lee et al. proposed the input force estimator includes fuzzy Kalman filter technology, which is accelerated by the fuzzy accelerating factor and the fuzzy weighting recursive least-square method, weighted by the fuzzy weighting factor based on the fuzzy logic inference system [40-42].

## **4.2. Theoretical Background**

### **4.2.1. Kalman filter algorithm**

The Kalman filter algorithm was developed by Rudolf E. Kalman 1960s [34]. To initiate the derivation, assume the linear stochastic difference equation:

$$x_k = Ax_{k-1} + Bu_{k-1} + w_{k-1} \quad (4-1)$$

with a measurement

$$z_k = Hx_k + v_k \quad (4-2)$$

$w_k$ , and  $v_k$  represent the process and measurement noise which is assumed to be zero mean and white and normal probability distributions

$E[w_k w_k^T] = Q$  and  $E[v_k v_k^T] = R$ , here  $Q$  is the process noise covariance,  $R$  is the measurement noise covariance.

Define estimation error:

$$e_k^- = x_k - \hat{x}_k^-, \text{ priori error}$$

$$e_k = x_k - \hat{x}_k, \text{ posterior error}$$

where  $\hat{x}_k^-$  is a priori state estimate at step  $k$  and  $\hat{x}_k$  is a posteriori state estimate at step  $k$  given measurement  $z_k$

An estimate error can be defined as follows:

$$P_k^- = E[e_k^- e_k^{-T}], \text{ a priori estimate error covariance}$$

$$P_k = E[e_k e_k^T], \text{ a posteriori estimate error covariance}$$

The Kalman filter can be defined under the assumption of the linear relation:

$$\hat{x}_k = \hat{x}_k^- + K_k (z_k - \hat{z}_k), \quad \hat{z}_k = H\hat{x}_k^- \quad (4-3)$$

The posterior estimate equals the prior estimate plus and added correction term. This correction includes a weighting matrix  $K_k$  and the

measurement innovation, or the residual ( $z_k - \hat{z}_k$ ). The innovation means the discrepancy between the predicted measurement ( $H\hat{x}_k^-$ ) and the actual measurement ( $z_k$ ). The gain  $K$  can be chosen to be minimizes the posteriori error covariance ( $P_k^-$ ). As a results, a minimized  $K$  is given by

$$K_k = P_k^- H^T (HP_k^- H^T + R)^{-1} \quad (4-4)$$

Equation (4-4) represents the popular form of the Kalman gain.

The Kalman filter algorithm consists of two groups: time update and measurement update. The time update equation is known to be as a predictor, while the measurement update equation is known to be as a corrector.

The predictor (time update equation) in the discrete time system is represented as,

$$\hat{x}_k^- = A\hat{x}_{k-1} + Bu_{k-1} \quad (4-5)$$

$$P_k^- = AP_{k-1}A^T + Q \quad (4-6)$$

And the corrector (measurement update) is represented as,

$$K_k = P_k^- H^T (HP_k^- H^T + R)^{-1} \quad (4-7)$$

$$\hat{x}_k = \hat{x}_k^- + K_k (z_k - H\hat{x}_k^-) \quad (4-8)$$

$$P_k = (I - K_k H)P_k^- \quad (4-9)$$

After each time and measurement update cycle, the process is repeated

again with the previous a posteriori estimates used to project or predict the new a priori estimates. The Kalman filter recursively conditions the current estimate on all of the past measurement. Figure 4-1 presents a complete procedure of the operating of the Kalman filter.

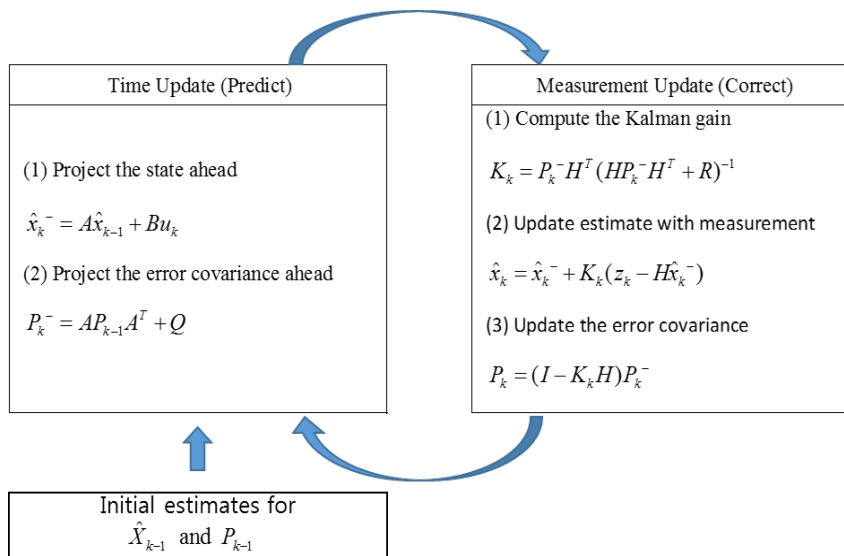


**Fig. 4-1 Complete operating procedure of the Kalman filter [34]**

#### 4.2.2. State-space equations of the system

In the present thesis, the input force estimation method is applied in the beam. In order to solve time domain motions for the  $n$  degree of freedom (dof) system using a computer, it is desirable to change the form of the equation for an  $n$ -degree-of-freedom system with  $n$  second order differential equations to  $2n$  first order differential equations. The first order form of motion equation is known as state-space form.

To construct the state-space equation of the beam structure, the beam element of the FEM is used. The differential equations of motion of the system in terms of mass, stiffness and damping are

$$M\ddot{Y}(t) + C\dot{Y}(t) + KY(t) = F(t) \quad (4-10)$$

where  $M$  is the  $n \times n$  mass matrix,  $C$  is the  $n \times n$  damping matrix,  $K$  is the  $n \times n$  stiffness matrix,  $F(t)$  is the  $n \times 1$  external force vector, and  $\ddot{Y}(t)$ ,  $\dot{Y}(t)$ ,  $Y(t)$  denotes the  $n \times 1$  acceleration, velocity, and displacement vectors respectively. To convert the Equation (4-10) to state-space form, the state variables are represented by a  $2n \times 1$  state vector.

$$X(t) = \begin{bmatrix} Y(t) & \dot{Y}(t) \end{bmatrix}^T \quad (4-11)$$

Plug in Equation (4-11) to Equation (4-10), and then 2nd differential equation can be expressed by 1st order differential equation (state equation) and measurement equation.

$$\dot{X}(t) = AX(t) + BF(t) \quad (4-12)$$

$$Z(t) = HX(t) \quad (4-13)$$

where

$$A = \begin{bmatrix} 0_{n \times n} & I_{n \times n} \\ -M^{-1}K & -M^{-1}C \end{bmatrix}, \quad B = \begin{bmatrix} 0_{n \times n} \\ M^{-1} \end{bmatrix}$$

$$X(t) = [X_1(t) \quad X_2(t) \quad \cdots \quad X_{2n-1}(t) \quad X_{2n}(t)]^T$$

$$F(t) = [F_1 \quad F_2 \quad F_3 \quad \cdots \quad F_n]^T$$

$H = I_{2n \times 2n}$  : Measurement matrix,  $Z(t)$  : Observation vector

Equations (4-12) and (4-13) are represented as a discretized form with time interval ( $\Delta t$ ), and associated with process noise of dynamic model and measurement noise. It can be represented as a discrete time state and statistical form. Then, Equation (4-12) becomes

$$X(k+1) = \Phi X(k) + \Gamma[F(k) + \omega(k)] \quad (4-14)$$

$$X(k) = [X_1(k) \quad X_2(k) \quad \cdots \quad X_{2n-1}(k) \quad X_{2n}(k)]$$

$$\begin{aligned} \Phi &= \exp(A\Delta t) \\ &\approx I + A\Delta t + \frac{(A\Delta t)^2}{2!} + \frac{(A\Delta t)^3}{3!} + \cdots \end{aligned}$$

$$\begin{aligned} \Gamma &= \int_{k\Delta t}^{(k+1)\Delta t} \exp\{A[(k+1)\Delta t - \tau]\} B d\tau \\ &= \int_0^{\Delta t} \exp(A\Delta t - \tau) B d\tau \\ &= \{(\Phi - I)A^{-1}\}B \end{aligned}$$

$$\omega(k) = [\omega_1(k) \quad \omega_2(k) \quad \cdots \quad \omega_n(k)]^T$$

$$F(k) = [F_1(k) \quad F_2(k) \quad \cdots \quad F_n(k)]^T$$

where

$X(k)$ : state vector,  $\Phi$ : the state transition matrix,  $\Gamma$ : the input matrix,  $\Delta t$ : the sampling interval,  $F(k)$ : the sequence of deterministic input, and  $w(k)$ : the noise vector which is assumed to be zero mean and white with variance  $E\{\omega(k)\omega^T(j)\} = Q\delta_{kj}$ ,  $Q = Q_w \times I_{n \times n}$ ,  $Q_w$  is the process noise covariance matrix (the process error for dynamic model),  $\delta_{kj}$  is the Kronecker delta.

Considering measurement noise, Equation (4-13) is represented as,

$$Z(k) = HX(k) + v(k) \quad (4-15)$$

$$Z(k) = [Z_1(k) \quad Z_2(k) \quad Z_3(k) \quad \cdots \quad Z_{2n}(k)]^T$$

$$v(k) = [v_1(k) \quad v_2(k) \quad v_3(k) \quad \cdots \quad v_{2n}(k)]^T$$

where

$v(k)$  is the measurement noise vector which is assumed to be zero mean and white noise. It is given by

$$E\{v(k)v^T(j)\} = R\delta_{kj}, \quad R = R_v \times I_{2n \times 2n}, \quad R_v = \sigma^2$$

$R$  is the measurement noise covariance matrix, and  $\sigma$  is the standard deviation of measurement noise.

### 4.2.3. Derivation of input force estimation procedure

Present input force estimation process consists of two part, one is the Kalman filter and the other is estimator using the least square method. The Kalman filter generates the residual innovation without external force term, after then the estimator calculates the external forces by using recursive least square method. Figure 4-2 shows the flow chart of the recursive input estimation algorithm.

The equation of the Kalman filter without force are represented by

State prediction:

$$\bar{X}(k/k-1) = \Phi\bar{X}(k-1/k) \quad (4-16)$$

State prediction covariance:

$$P(k/k-1) = \Phi P(k-1/k)\Phi^T + \Gamma Q \Gamma^T \quad (4-17)$$

Kalman gain:

$$K_a(k) = P(k/k-1)H^T [HP(k/k-1)H^T + R]^{-1} \quad (4-18)$$

Innovation covariance:

$$S(k) = HP(k/k-1)H^T + R \quad (4-19)$$

Updated state covariance:

$$P(k/k) = [I - K_a(k)H]P(k/k-1) \quad (4-20)$$

Innovation or Residual:

$$\bar{Z}(k) = Z(k) - H\bar{X}(k/k-1) \quad (4-21)$$

Updated state estimation:

$$\bar{X}(k/k) = \bar{X}(k/k-1) + K_a(k)\bar{Z}(k) \quad (4-22)$$

In this case, an external forces are not considered in the state model, i.e.,  $\bar{X}$  denotes predicted state without input forces.

Based on the previous studies [36, 38], the equation of the recursive least square algorithm are derived in more detail by Wu et al. [43].

Let  $\bar{X}(k/k)$  and  $\hat{X}(k/k)$ , denote the predicted state ( $X(k)$ ) without and with external forces  $F(k-1)$ .

First step, the time updated state without input forces can be expressed as

$$\begin{aligned} \bar{X}(k/k) &= \bar{X}(k/k-1) + K_a(k)\bar{Z}(k) \\ &= \bar{X}(k/k-1) + K_a(k)[Z(k) - H\bar{X}(k/k-1)] \\ &= [I - HK_a(k)]\bar{X}(k/k-1) + K_a(k)Z(k) \\ &= [I - HK_a(k)]\Phi\bar{X}(k-1/k) + K_a(k)Z(k) \end{aligned} \quad (4-22)$$

And the updated state with input forces can be expressed as

$$\begin{aligned} \hat{X}(k/k) &= \hat{X}(k/k-1) + K_a(k)\hat{Z}(k) \\ &= \hat{X}(k/k-1) + K_a(k)[Z(k) - H\hat{X}(k/k-1)] \\ &= [I - HK_a(k)]\hat{X}(k/k-1) + K_a(k)Z(k) \\ &= [I - HK_a(k)][\Phi\hat{X}(k-1/k) + \Gamma F] + K_a(k)Z(k) \end{aligned} \quad (4-23)$$

Second step, the discrepancy between  $\hat{X}(k/k)$  and  $\bar{X}(k/k)$  is defined as

$$\begin{aligned}
\Delta X(k/k) &= \hat{X}(k/k) - \bar{X}(k/k) \\
&= [I - K_a(k)H][\Phi\{\hat{X}(k-1/k) - \bar{X}(k-1/k)\} + \Gamma F] \\
&= [I - K_a(k)H][\Phi\Delta X(k-1/k) + \Gamma F]
\end{aligned} \tag{4-24}$$

From Equation (4-24),  $\Delta X(k/k)$  can be expressed as

$$\Delta X(k/k) = M_s(k)\Gamma F \tag{4-25}$$

Substitute Equations (4-25) to (4-24), and rearrange the equations

$$\begin{aligned}
M_s(k)\Gamma F &= [I - K_a(k)H][\Phi M_s(k-1)\Gamma F + \Gamma F] \\
&= [I - K_a(k)H][\Phi M_s(k-1) + I]\Gamma F
\end{aligned} \tag{4-26}$$

Therefore,  $M_s(k)$  can be derived as;

$$\therefore M_s(k) = [I - K_a(k)H][\Phi M_s(k-1) + I] \tag{4-27}$$

From Equation (4-25), the relation between the two estimations with and without input forces is expressed as

$$\hat{X}(k/k) = \bar{X}(k/k) + M_s(k)\Gamma F \tag{4-28}$$

Third step, the innovation (residual) of measurement  $Z(k)$  with and without input forces are represented as  $\hat{Z}(k)$  and  $\bar{Z}(k)$ .

$$\begin{aligned}
\bar{Z}(k) - \hat{Z}(k) &= \{Z(k) - H\bar{X}(k/k-1)\} - \{Z(k) - H\hat{X}(k/k-1)\} \\
&= H\Phi\hat{X}(k-1/k) - H\Phi\bar{X}(k-1/k) + H\Gamma F \\
&= H\Phi\{\hat{X}(k-1/k) - \bar{X}(k-1/k)\} + H\Gamma F \\
&= H\Phi M_s(k-1)\Gamma F + H\Gamma F \\
&= H[\Phi M_s(k-1) + I]\Gamma F
\end{aligned} \tag{4-29}$$

The discrepancy between  $\hat{Z}(k)$  and  $\bar{Z}(k)$  can be represents as

$$\bar{Z}(k) = \hat{Z}(k) + B_s(k)F \quad (4-30)$$

From Equations (4-29) and (4-30),

$$B_s(k) = H(\Phi M_s(k-1) + I)\Gamma \quad (4-31)$$

Based on the Equations (4-30) and (4-31), unknown input force can be estimated using the recursive least-square algorithm which is shown in Appendix-A [35]. The resultant force estimation equation can be obtained as follows:

Sensitivity matrix:

$$\begin{aligned} B_s(k) &= H[\Phi M_s(k-1) + I]\Gamma \\ M_s(k) &= [I - K_a(k)H][\Phi M_s(k-1) + I] \end{aligned} \quad (4-32)$$

Correction gain for the updating input forces:

$$K_b(k) = \gamma^{-1} P_b(k-1) B_s^T(k) [B_s(k) \gamma^{-1} P_b(k-1) B_s^T(k) + S(k)]^{-1} \quad (4-33)$$

Error covariance of the estimated input forces:

$$P_b(k) = [I - K_b(k) B_s(k)] \gamma^{-1} P_b(k-1) \quad (4-34)$$

Estimated input forces:

$$\hat{F}(k) = \hat{F}(k-1) + K_b(k) [\bar{Z}(k) - B_s(k) \hat{F}(k-1)] \quad (4-35)$$

The scalar parameter ( $\gamma$ ), namely fading factor, is an adaptive factor to compromise between the fast adaptive capability and the loss of estimate accuracy. It is determined by using intelligent fuzzy weighting function. The intelligent fuzzy weighting factor can be operated at each

step based on the innovation (residual) from the Kalman filter [41]. Tuan et al. [36] proposed the relation between fading factor ( $\gamma$ ) and innovation ( $\bar{Z}(k)$ ) as follows:

$$\gamma(k) = \begin{cases} 1 & |\bar{Z}(k)| \leq \sigma \\ \frac{\sigma}{|\bar{Z}(k)|} & |\bar{Z}(k)| > \sigma \end{cases}$$

More detail description about the intelligent weighting process is presented in Appendix-B.

The procedure to estimate the unknown input forces using inverse method is shown Figure (4-2) and is summarized as follows:

- i) Derive the state-space model, i.e., Equations (4-12), (4-13), and obtain an estimated system state ( $X(k)$ ) from measurement.
- ii) Using the Kalman filter, i.e., Equations (4-16) ~ (4-21), to obtain the innovation covariance ( $S(k)$ ), innovation ( $\bar{Z}(k)$ ) and Kalman gain ( $K_a(k)$ ).
- iii) Using the recursive least-square algorithm, i.e., Equations (4-31) ~ (4-35), to estimate the unknown input force ( $\hat{F}(k)$ ).

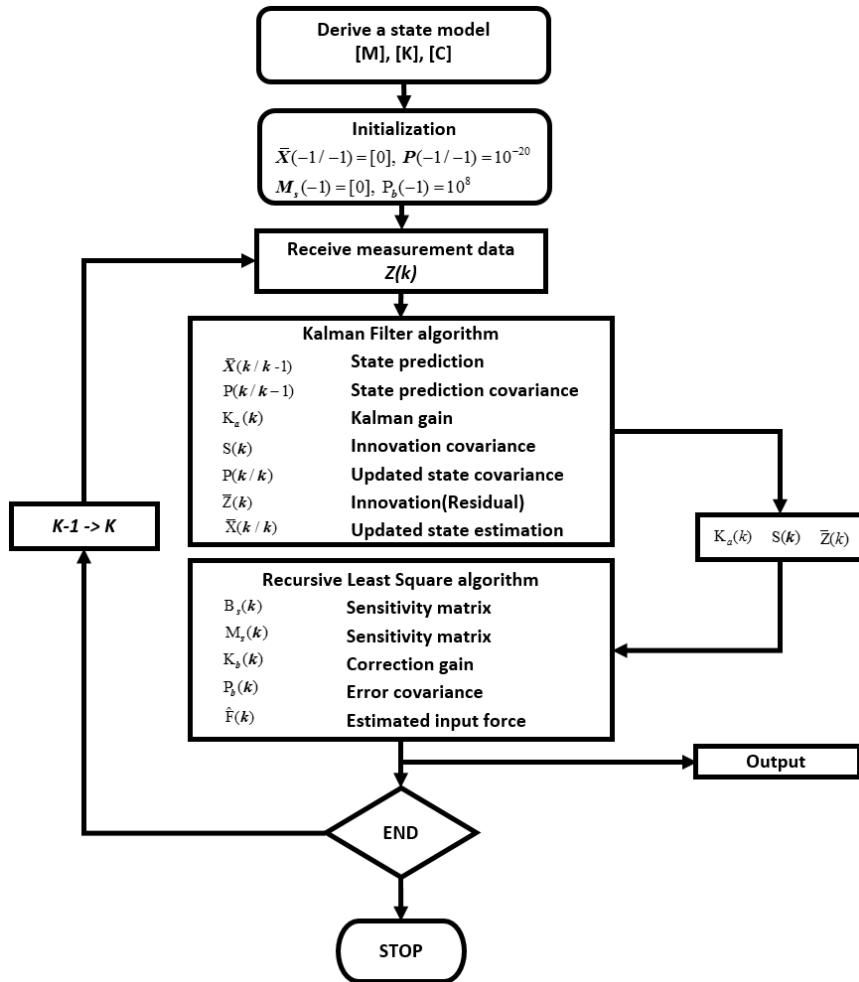


**Fig. 4-2** Flow chart of the recursive input estimation algorithm

### 4.3. Verification by a Simple Structure

To verify the practicability of the present approach, numerical simulation of a cantilever beam is investigated here. The finite model cantilever beam which has three degrees of freedom, i.e., longitudinal direction (u), transverse direction (v), and rotation ( $\theta$ ), as shown in Figure 4-3. The material properties and geometry dimension of the cantilever beam are shown in Table 4-1. The finite element mass  $[M]^e$  and stiffness matrix  $[K]^e$  can be obtained by Bernoulli-Euler beam element definition [44].

$$M^e = \frac{\rho AL}{420} \begin{bmatrix} 140 & 0 & 0 & 70 & 0 & 0 \\ & 156 & 22L & 0 & 54 & -13L \\ & & 4L^2 & 0 & 13L & -3L^2 \\ & & & 140 & 0 & 0 \\ & SYM & & & 156 & -22L \\ & & & & & 4L^2 \end{bmatrix}$$

$$K^e = \begin{bmatrix} \frac{EA}{L} & 0 & 0 & -\frac{EA}{L} & 0 & 0 \\ & \frac{12EI}{L^3} & \frac{6EI}{L^2} & 0 & -\frac{12EI}{L^3} & \frac{6EI}{L^2} \\ & & \frac{4EA}{L} & 0 & -\frac{6EI}{L^2} & \frac{2EI}{L} \\ & & & \frac{12EI}{L} & 0 & 0 \\ & SYM & & & \frac{12EI}{L^3} & -\frac{6EI}{L^2} \\ & & & & & \frac{4EI}{L} \end{bmatrix}$$

The proportional damping, a special type of viscous damping, is used in this thesis. The proportional damping model expresses the damping matrix as a linear combination of the mass and stiffness matrices, that is

$$[C] = \alpha[M] + \beta[K] \quad (4-35)$$

This damping model is known as ‘Rayleigh damping’ or ‘classical damping’ [45]. It varies with frequency, and  $\alpha$ ,  $\beta$  are real scalars. It is known that  $\alpha$  affects more at low frequency range whereas  $\beta$  affects more at high frequency ranges (see Figure 4-4). Damping matrix can be determined by using a damping estimation procedure proposed in this thesis [see Appendix-C].

The numerical FEM simulation to get system matrix (mass, stiffness and damping) and responses (displacement) at nodal point is performed by Co-Rotational FEM code which is a non-linear in-house code.

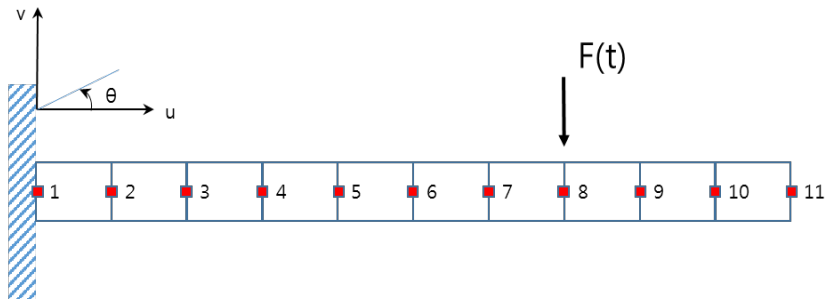


**Fig. 4-3 Finite model of the cantilever beam  
(10 element with 11 nodes)**

**Table 4-1** Dimensions and material properties of the cantilevered beam

	Symbol	Aluminum alloy
Density (kg/m <sup>3</sup> )	$\rho$	2710
Elastic modulus (Gpa)	E	70
The Poisson ratio	$\nu$	0.33
Length (m)	L	0.264
Width (m)	W	0.030
Height (m)	H	0.005

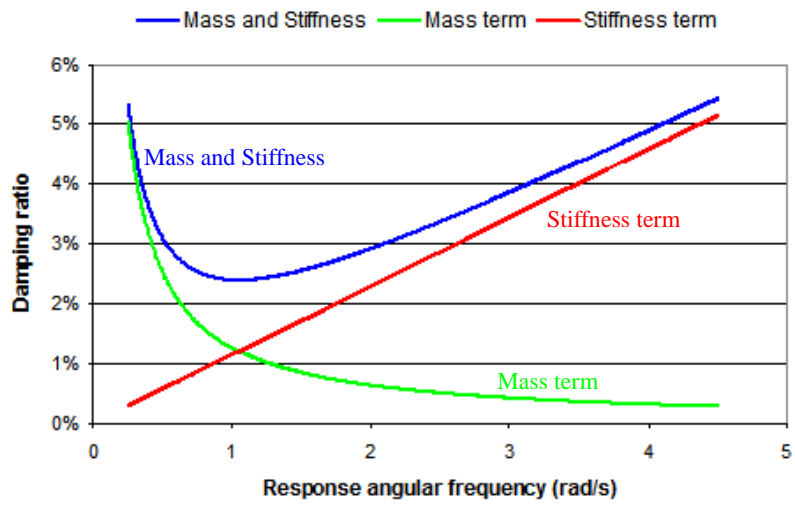


**Fig. 4-4** Example of Rayleigh damping ( $\zeta_i = \frac{\alpha}{2\omega_i} + \frac{\beta\omega_i}{2}$ )

### 4.3.1. Case I: sinusoidal excitation force (single sinusoidal)

The single sinusoidal force acts on node 8 of the beam is introduced as below:

$$F(t) = 3 \times \sin(180 \times 2\pi \times t), \quad 0 \leq t \leq 0.05 \text{ sec}, \quad \Delta t = 1.0 \times 10^{-4} \text{ sec}$$

Three of response data (displacement) measured at node 3, 9, and 10 are used as an input data of the input force estimation process. The parameters used in the numerical estimation are as follows: covariance of the process noise  $Q_w = 1.0 \times 10^{-5}$ , the measurement noise  $R_v = 1.0 \times 10^{-15}$ , and the fading factor ( $\gamma$ ) is adjusted at each step by intelligent weighting process.

Figure 4-5 shows the comparisons between estimated results and measurement data. It shows quite good agreement between the two. The error used to quantify the deviations between the estimated and exact input force is defined as:

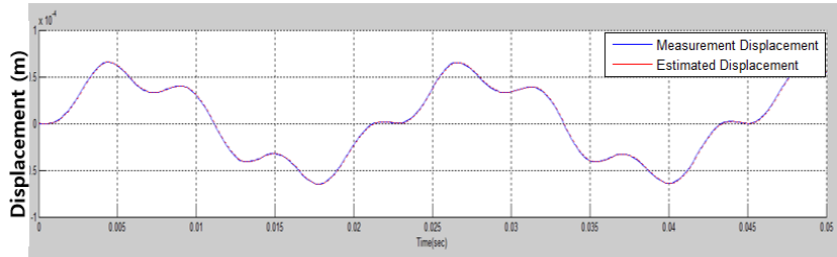
$$Error(\%) = \frac{\sqrt{\sum_{i=1}^p [f^{ex}(t_i) - f^{es}(t_i)]^2}}{\sqrt{\sum_{i=1}^p [f^{ex}(t_i)]^2}} \times 100 \quad (4-36)$$

where  $f^{ex}(t_i)$ : exact input force,  $f^{es}(t_i)$ : estimated input force

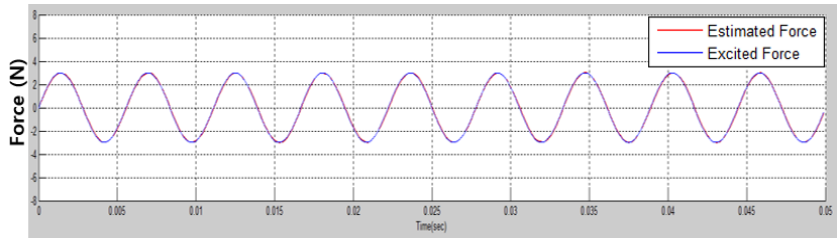
In this case, the estimated error is only 4.1%.

Figure 4-6 shows the case acted by the same input force as the previous case (Figure 4-5), but it contains measurement noise with covariance

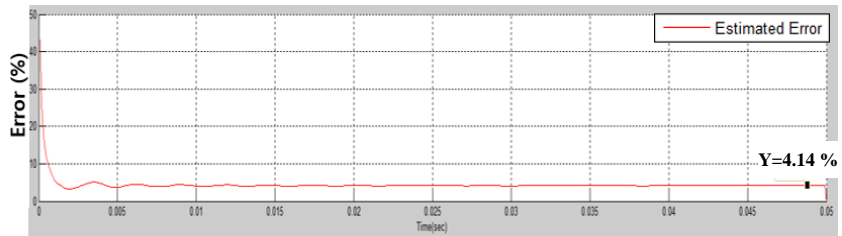
( $\sigma = 1.0 \times 10^{-5}$ ). At first, Kalman filter process removes noise from the measurement and construct the optimized state at each node points. And then RLSM estimate the input force by using optimized state. In this case, the estimated error is 4.16%. It is almost the same as the previous case though the measurement data contains relatively large noise.



(a) Time history of the displacement at Node 9  
(blue: measurement , red: estimated by Kalman filter)

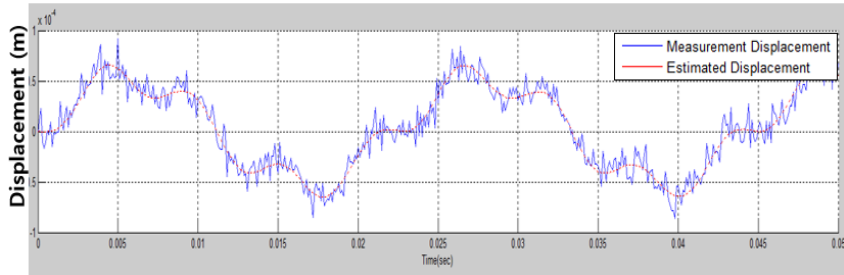


(b) Time history of the input force at Node 8  
(blue: exact force , red: estimated input force)

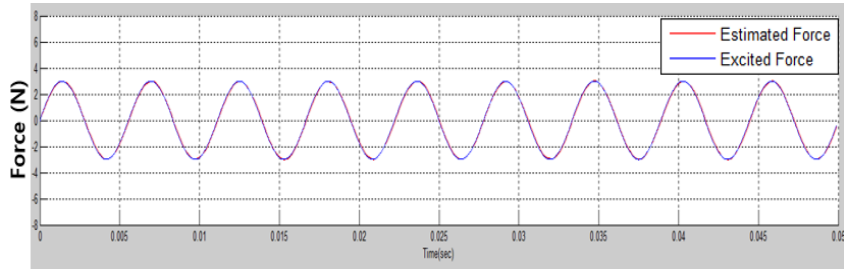


(c) Time history of the estimated error  
(Excited force vs. estimated input force)

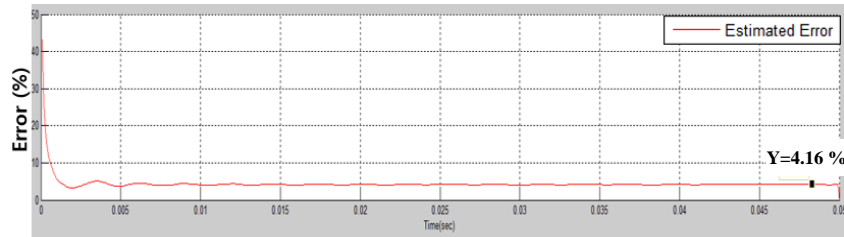
**Fig. 4-5 Comparison between measurement and estimated results for the sinusoidal force (without measurement noise)**



(a) Time history of the displacement at Node 9  
(blue: measurement , red: estimated by Kalman filter)



(b) Time history of the input force at Node 8  
(blue: exact input force , red: estimated input force)



(c) Time history of the estimated error (input force)

**Fig. 4-6 Comparison between measurement and estimated results,  
sinusoidal force (with measurement noise,  $\sigma = 1.0 \times 10^{-5}$  )**

### 4.3.2. Case II: Impulsive excitation force

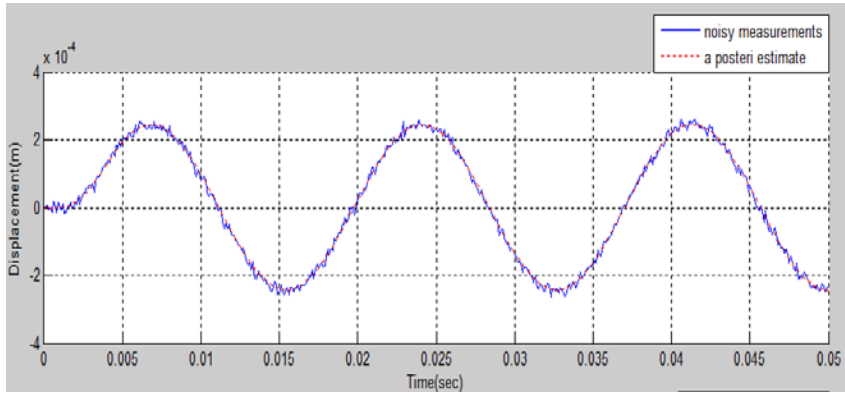
To examine performance of the present inverse method, the case which impulsive force exerted on Node 8 is considered. The shape of the impulsive force is expressed as

$$\begin{aligned} F_8(t) &= 0 \text{ (N)}, & 0 \leq t \leq 0.001 \text{ (s)} \\ F_8(t) &= 2 \text{ (N)}, & 0.001 < t \leq 0.004 \text{ (s)} \\ F_8(t) &= 0 \text{ (N)}, & t > 0.004 \text{ (s)} \end{aligned}$$

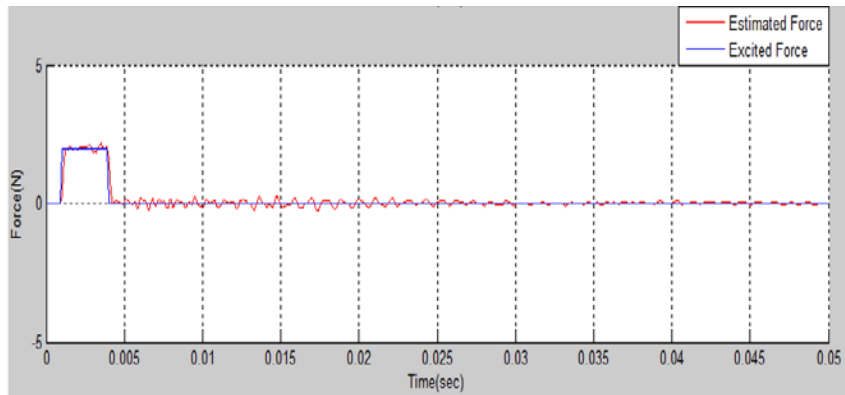
The simulation parameters, and measurement locations are the same as the previous case while sampling frequency (10,000 Hz) is greater than that in the previous case. Figure 4-6 shows the comparisons of estimation results with measurement displacement (Figure 4-7 (a)) and exact force (Figure 4-7 (b)) in the time domain. And Figure 4-8 presents comparisons between estimation result and exact force in frequency domain. It is also good agreement between the two.

In Figure 4-7 (a), it shows that the measurement data contains sensor noise (blue line) but Kalman filter estimates displacement without noise (red line). Figure 4-7 (b) shows a good tracking ability to estimate input force but it has small fluctuations on the mean value. This small fluctuating components can be investigated in the frequency domain. Figure 4-8 shows the frequency spectrum of estimation and exact force. It is relatively good agreement with each other at lower than 3,000 Hz but the discrepancy between estimation result and exact force become larger

as frequency increases beyond 3,000 Hz. The small peaks in the estimation result correspond with the natural frequencies of the beam structure. It is found that natural frequency of the structure affects estimation results in the present inverse estimation method of force.



(a) Time history of the displacement at Node 9  
(blue: measurement , red: estimated by Kalman filter)



(b) Time history of the input force at Node 8  
(blue: exact input force , red: estimated input force)

**Fig. 4-7 Time history of the comparison between measurement (blue line) and estimation result (red line), impulsive force (with measurement noise)**

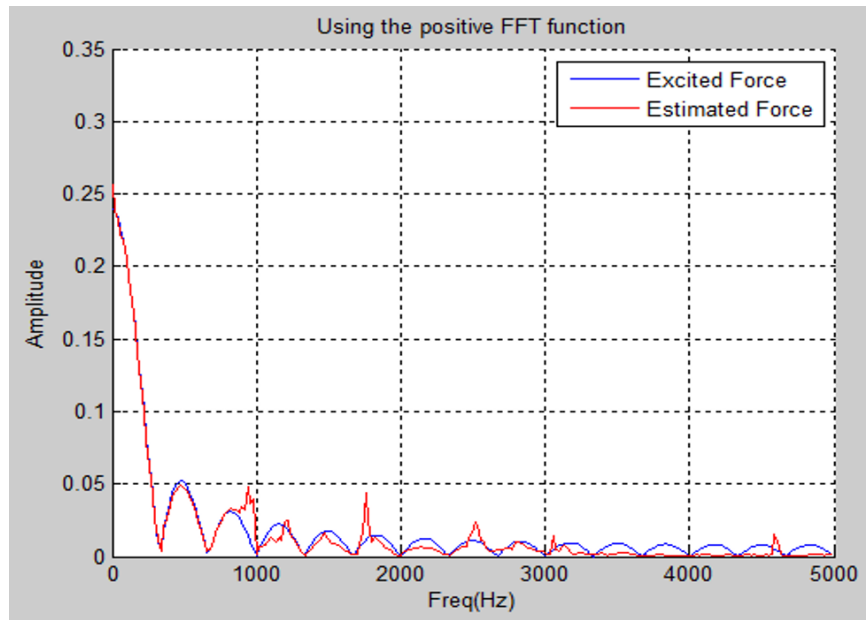


**Fig. 4-8 Frequency spectrum of the comparison between exact (blue line) and estimation force (red line), impulsive force (with measurement noise)**

### 4.3.3. Case III: Random excitation force

Estimating a random force is investigated here to consider the rocket motor self-excited forces at the inter-stage of an HSFV because rocket motor self-excited force is known as a random force. The random force is generated by a signal generator using the MATLAB software as follows:

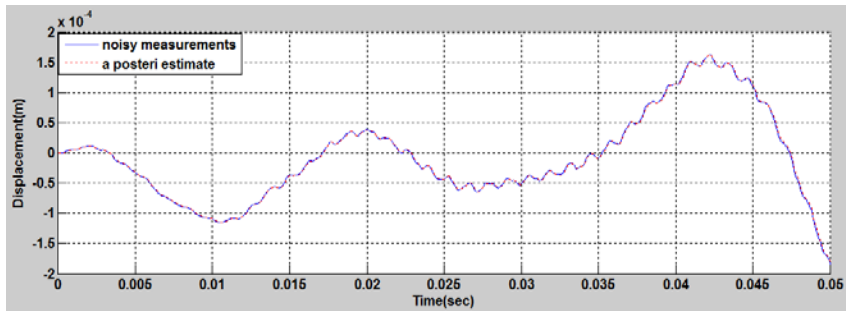
$$F_9(t) = 2 \times \text{randn} \text{ (N)} \text{ , (at node 9)}$$

It has a zero mean and 2N of standard deviation with normal distribution (see, Figure 4-8 (b)).

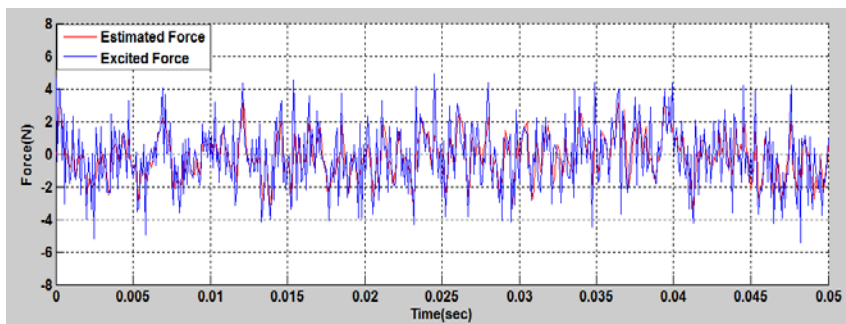
In this case, five of measurements, i.e. Node 5, 6, 7, 8, and 10, are used as an input and sampling frequency is 10,000 Hz. The covariance of the process noise is  $Q_w = 1.0 \times 10^{-2}$  and the measurement noise is  $R_v = 1.0 \times 10^{-10}$  respectively.

The estimated results in Figure 4-9 (a) and (b) show that the present input force estimation method has a good tracking capability for the random excitation force in the low frequency range. To investigate more details, Figure 4-9 (c) presents the comparison of estimation result and exact input force in narrow time duration (i.e. 0.00 to 0.01 sec.). The discrepancy between exact and estimation result is observed. It seems that present input estimation method can't exactly track the high frequency contents. It can be observed more clearly using the frequency spectrum of

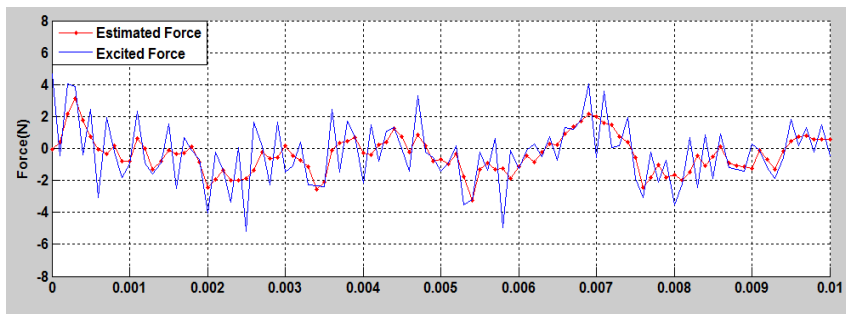
the input force. Figure 4-10 shows the frequency spectrum of the displacement (a) and input force (b). In the case of displacement (Figure 4-10 (a)), it is in good agreement with the estimation result and the measurement even in the high frequency range. In contrast, in the case of input force, the discrepancy is shown in high frequency range (in this case, over 1,000 Hz). And it is interesting that the discrepancy become increase after a certain peak which is correspond to natural frequency of the beam. That is, it is found that the natural frequency contents are included in the input estimation results even if it is not real one because present estimation method is operated based on the measurement data which include natural frequency contents of the structural. To improve accuracy of input force estimation in the higher frequency range, the influence of natural frequency on the estimation results will be studied in the future.



(a) Time history of the displacement at Node 5  
(blue: measurement , red: estimated by Kalman filter)

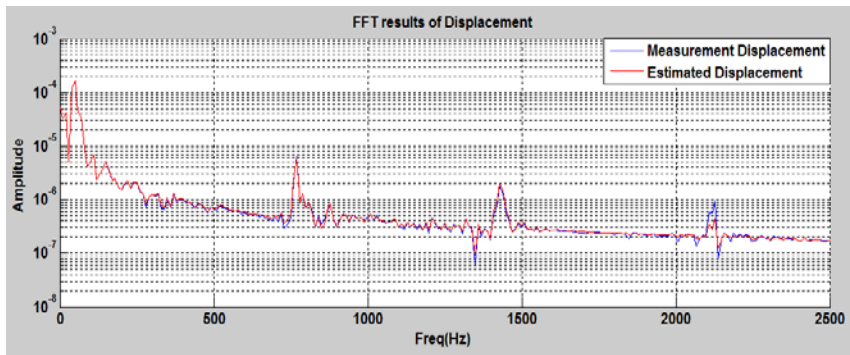


(b) Time history of the input force at Node 9  
(blue: exact input force , red: estimated input force)

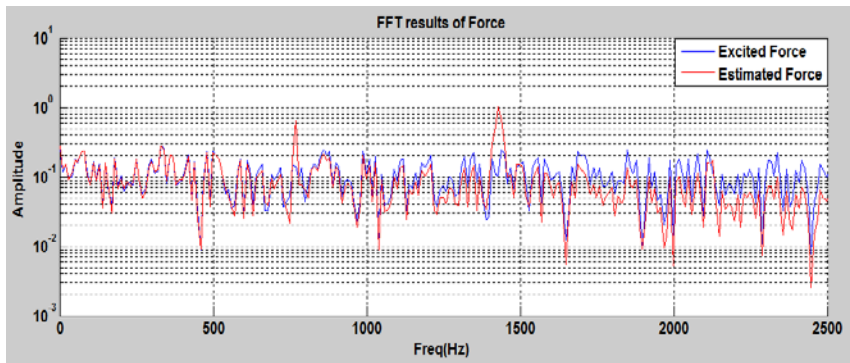


(c) Zoom in the time history of the input force  
(blue: exact input force , red: estimated input force)

**Fig. 4-9 Time history of the comparison between measurement (blue line) and estimation result (red line), (Random excitation)**



(a) Frequency spectrum of the displacement at Node 7



(b) Frequency spectrum of the input force at Node 9

**Fig. 4-10** Frequency spectrum of the displacement and input force  
(Random excitation)

## **Chapter 5.**

# **Prediction on Fluctuating Surface Pressure of the High Speed Flight Vehicle**

### **5.1. Introduction**

The ramjet engine is widely used as one of the most efficient and most advanced propulsion systems for a supersonic flight vehicle. Due to its geometric simplicity, it has been widely adopted by supersonic missiles. Recently, Russia (YAKHONT), India (BrahMos) and China (CX-1) have developed supersonic vehicles which have adopted a ramjet engine. It was found that these were developed based on the YAKHONT vehicle, which is a supersonic anti-ship cruise missile developed by Russia [46].

The high speed flight vehicle (HSFV) is regarded as an imaginary supersonic flight vehicle equipped with a ramjet engine in this thesis. It has a similar configuration with that of YAHONT in terms of the realistic configuration, rather than an ideal one in Nagashima's experimental ramjet configuration [47]. This type of vehicle experiences severe dynamic loads during atmospheric flight. Such dynamic loads are random vibratory loads caused by aerodynamic fluctuating pressures acting on the surface of the vehicle.

Around the supersonic air inlet, shock and boundary interaction may lead to severe fluctuating pressures and self-excited shock oscillation. This self-excited oscillation is referred to as inlet buzz. Many researchers [47-50] have studied the buzz phenomenon occurring in those vehicles as early as the 1940s. Hong et al. [48] presented computational investigations of these buzz characteristics on a supersonic inlet considering the historic path of a mass flow change using Nagashima's experimental ramjet configuration. Nagashima's ramjet configuration belongs to a wind tunnel testing article. It showed a representative experimental result for a ramjet buzz effect [47]. Yeom et al. [50] conducted a numerical analysis to investigate the inlet buzz and combustion oscillation in an axisymmetric ramjet engine with a combustion flame holder. In their study, a YAHONT type configuration was used to analyze the buzz effect.

However, in this thesis, the buzz phenomenon is not considered in depth because there already exist many investigations about the buzz effect for the ramjet engine. In contrast, only a few investigations have been found about the fluctuating surface pressures in a supersonic air inlet. In more detail, the random vibratory loads caused by the fluctuating surface pressures acting on the external surface and inner wall of the air inlet are readily considered and analyzed in this thesis. The fluctuating surface pressures (i.e. shock wave, separated flow, attached flow and combined flow) are random in nature. Those are responsible for the main

fuselage noises and vibrations in the vehicle. It excites the surface of the vehicle and generates vibratory loads on the fuselage. Those vibratory loads are transferred via complex path to the inner wall of the vehicle and may affect electronic equipment. Hence, those loads play important roles when prescribing the criteria written in the principal structural design of the vehicle [5].

It is not straightforward to predict the fluctuating pressures acting on the flight vehicle analytically, and therefore many previous studies [13, 51, 52] have relied on empirical models when predicting such environments.

Cockburn and Robertson [13] presented the vibratory response of a spacecraft shroud caused by the fluctuating pressures impinging on the surface of the vehicle. The ATLAS-Agena shroud was analyzed at three critical flight Mach numbers. Their semi-empirical model was suggested to predict the fluctuating pressure spectrum for typical air flows, which were shock wave, separated flow, and attached flow. In this paper, the ATLAS-Agena analysis model and prediction results of the fluctuating pressure at Mach number 0.8 will be compared with the presently suggested estimation procedure.

Recently, Klabas et al. [53] presented a prediction procedure and measurement results for the surface pressure fluctuations beneath the turbulent boundary layers (TBL) on an Airbus A320 test aircraft. The feasibility of predicting the surface pressure power spectra was

investigated by applying the various semi-empirical models on the fuselage of the experimental aircraft. Predicting the accuracy of the semi-empirical models could be improved by using TBL parameters (i.e., the pressure coefficient, the local boundary layer thickness, and the turbulence kinetic energy) extracted from the computational fluid dynamics (CFD) simulation. However, the prediction results obtained by the semi-empirical models showed a significant discrepancy over 2,000 Hz frequency range when compared with the measurement data.

Most of the investigations regarding the fluctuating surface pressures were focused on the external surface of the vehicle. However, a vehicle with an air-breathing inlet, such as a ramjet engine, is found to be affected by not only external flow around the vehicle but also internal flow inside the inlet. Therefore, this thesis attempts a prediction of the surface pressure fluctuations by considering both external and internal flows. The present procedure to predict the fluctuating pressures is in fact a combination of CFD and structural finite element analysis (FEA). It is thus capable of predicting the fluctuating pressures caused by complex aerodynamic flows (i.e. shock wave, separated flow, and attached flow) on various locations in the vehicle. After the fluctuating surface pressure is determined, it can be used as an external load to predict the vibratory response of the vehicle using the specific structural analysis methods, i.e. statistical energy method (SEA) and modal superposition method in FEA.

First in this paper, the present procedure will be verified by using the ATLAS-Agena shroud configuration [54-56] against the existing semi-empirical models because of the lack of experimental data available for a HSFV. After that, the HSFV will be analyzed regarding its fluctuating surface pressure on the external surface of a vehicle and inside the air inlet using the present prediction procedure.

## **5.2. Present Prediction Procedure**

Aerodynamic fluctuating pressures were considered as one of the most significant dynamic excitations of the vehicle in the 1960s because a series of the launch vehicle failures occurred at transonic flights [57].

In general, the strength of the fluctuating surface pressures is proportional to the free-stream dynamic pressure ( $q_\infty$ ) for a given unsteady flow. However, the fluctuating pressures are not increased at every location even for a significantly increased free-stream dynamic pressure. This will be the case for a configuration with a rapid change in the cross-section due to the non-homogeneous flow field. Regions exposed to the shock waves and separated flow will experience increased fluctuating pressures of at least ten times larger magnitude than those exposed to an attached flow. Accordingly, the geometry of the flight

vehicle will determine the aerodynamic fluctuating pressure levels because the air flows are closely related to the geometry [13].

In this thesis, a prediction procedure will be suggested to predict the time history of the fluctuating pressures acting on the surface of the vehicle by using CFD simulation. From such CFD results, the frequency spectrum of the fluctuating surface pressure will be established and examined using VA-ONE, which is a commercial vibro-acoustic analysis program.

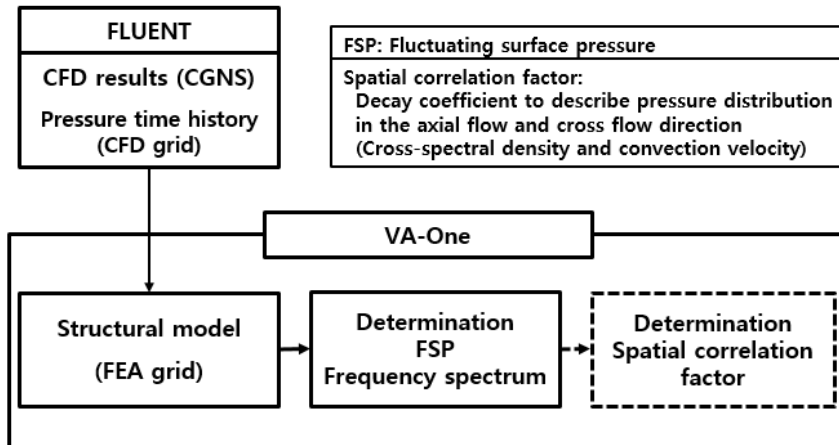
Before estimation is performed on the vibratory response of a structure excited by fluctuating pressure flow, the fluctuating pressure loads impinging on the surface will be determined. The key parameters for such determination are the following: (a) the overall pressure level, (b) the power spectrum, and (c) the spatial correlation coefficients of the structure [13]. After those parameters are determined, the vibratory response will be predicted using either the statistical energy analysis (SEA) or a modal superposition method in FEA.

Figure 5-1 shows a procedure used to determine the fluctuating surface pressures. The detailed description of the present procedure is as follows.

The time history of the fluctuating pressures is estimated from the CFD simulation at each fluid grid. And then it will be exported to CFD general notation system (CGNS) file format together with the geometry data from CFD (FLUENT) analysis results. VA-ONE will then import the pressure

history to the relevant structural grids from each CGNS file and compute the frequency spectrum on the surface of the vehicle using fast Fourier transformation (FFT) and signal processing.

The spatial correlation factor is the final requirement in determining the characteristics of the fluctuating pressure fields [13]. It is a correlation factor to describe impinging pressure distribution in order to calculate the induced mean-square vibratory response of the structure [Reference-D]. Hence external loads impinging on the surface can be calculated using the spatial correlation factor and the fluctuating surface pressure frequency spectrum.



**Fig. 5-1 Procedure for determining the fluctuating surface pressures using CFD and VA-ONE**

## **5.3. Existing Semi-Empirical Model for the Attached Flows**

For the past fifty years, many researchers have studied prediction methods for the pressure fluctuating loads generated by the aerodynamic flows, such as shock waves and attached flow, acting on the surface of the vehicle. Such prediction methods suggested are quoted in this thesis as the semi-empirical models.

In this section, brief descriptions for the three existing representative semi-empirical models, especially for the well-developed attached flow, will be given for the prediction of the surface pressure fluctuating spectra. The semi-empirical model for the attached flow is relatively straightforward to calculate, and it has been well verified in many studies.

### **5.3.1. Cockburn and Robertson's model**

Cockburn and Robertson proposed a pressure fluctuation formulation on the shroud of an ATLAS-Agena launch vehicle [13]. It was developed based on Robertson's semi-empirical model for attached flow and corrected using the wind tunnel and flight test results. As shown in Figure 5-2, various unsteady flows are developed with respect to flight speed and configuration of the vehicle. Those are the shock wave, separated flow,

and attached flow. In this section, a brief description of the attached flow is presented.

Overall mean square pressure fluctuation level is expressed as follows.

$$\sqrt{\overline{P^2}}/q_\infty = 0.006/(1 + 0.14M_\infty^2) \quad (5-1)$$

where the dynamic pressure is given by  $q_\infty = \frac{1}{2}\rho U_\infty^2$ .

Equation (5-1) was introduced by Lawson [58] and has good agreement with experimental results in Mach number range from 0.6 to 3.0 [53].

Power spectrum is formulated as follows.

$$\frac{\Phi(f)U_l}{q_\infty^2 \delta_l} = \frac{\left(\overline{P^2}/q_\infty^2\right)}{\left(f_0 \delta_l / U_l\right) \{1 + (f/f_0)^{0.9}\}^{2.0}} \quad (5-2)$$

The characteristic frequency is given for an attached flow as follows.

$$f_0 = 0.346 \frac{U_l}{\delta_l} \quad (5-3)$$

where the local flow speed is  $U_l \approx U_\infty$ , and  $\delta_l$  is the local turbulent boundary layer thickness.

It can be estimated by

$$\delta_l = 0.37 \frac{x}{\text{Re}^{0.2}} \quad \text{with} \quad \text{Re} = \frac{xU_\infty}{\nu}$$

and the velocity at the boundary layer edge can be approximated as follows:

$$U_e = 0.99U_\infty$$

Cockburn and Robertson's model is known as a little conservative estimation formulation. It has a large plateau in the lower frequency range with a decreasing trend at the higher frequencies [53].

### 5.3.2. Emfimtsov's model

Emfimtsov's model [51] was proposed in 1982. It was derived in terms of Mach number ( $Ma$ ), Reynolds number ( $Re$ ), and Strouhal number ( $St$ ). It was based on the empirical results measured on the various location of the test vehicle. The test data were collected in Mach number range from 0.41~ 2.1 and high Reynolds number range  $Re = 0.5 \times 10^8 \sim 4.85 \times 10^8$ .

Emfimtsov's semi-empirical model is expressed by

$$\Phi(\omega) = \frac{0.01\tau_\omega^2 \delta_l^2}{U_\tau \left[ 0.1 + 0.02 \times St(\omega)^{2/3} \right]} \quad (5-4)$$

where Strouhal number in this case is presented as follows.

$$St(\omega) = \frac{\omega \delta_l}{U_\tau}$$

The shear stress in the TBL can be calculated by

$$\tau_\omega = 0.5 \times C_f \times \rho \times U_e^2$$

The skin friction ( $C_f$ ) is used by Blasius' empirical equation for the resistance coefficients in the pipe flow in the forms [51]

$$C_f = 0.045 \left( \frac{v}{U_e \delta_t} \right)^{0.25}$$

The shear velocity or friction velocity is represented as follows.

$$U_\tau = \sqrt{\frac{\tau_w}{\rho}}$$

### 5.3.3. Goody's model

Goody proposed a semi-empirical model which was derived based on the empirical pressure fluctuating data sets measured by seven research groups in 2004 [52]. Goody's model was developed based on Chase and Howe's model. It was corrected and modified to cover the broad range of Reynolds number ( $1.4 \times 10^3 < Re_\theta < 2.34 \times 10^4$ ) by using the time scale ratio ( $R_T$ ) which is a relating parameter of the pressure fluctuation between the inner and outer layers.

Goody's semi-empirical model is expressed as follows.

$$\frac{\Phi(\omega)U_e}{\tau_w^2 \delta_t} = \frac{3.0 \times St(\omega)^2}{[St^{0.75} + 0.5]^{3.7} + [(1.1 \times R_T^{-0.57}) \times St(\omega)]^7} \quad (5-5)$$

where Strouhal number is as follows.

$$St(\omega) = \frac{\omega \delta_t}{U_e}$$

Goody presented the time scale ratio in his study [52]. It can be shown that

$$R_r = 0.0107 \left( \frac{U_e x}{\nu} \right)^{\frac{3}{5}}$$

It is known that Goody's model fits the measurement data best among the semi-empirical models presented in this thesis [53].

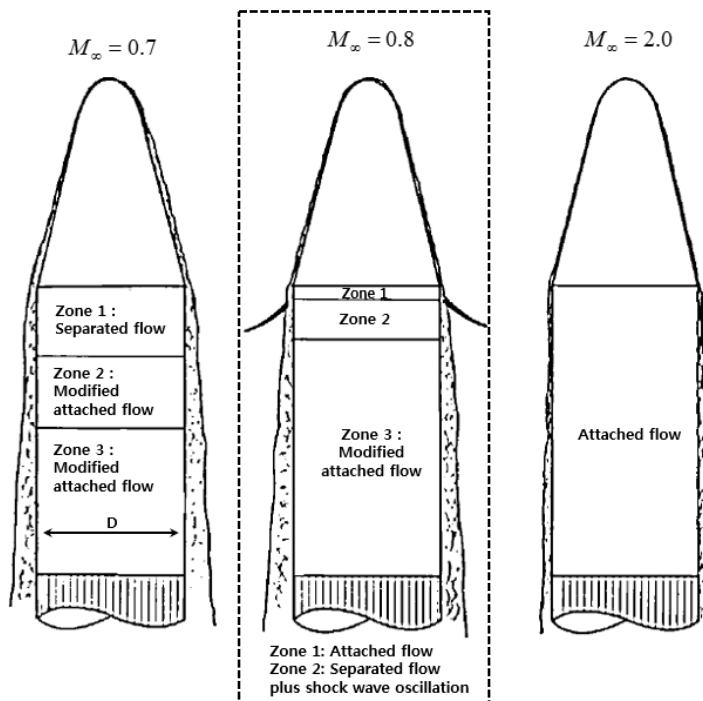


**Fig. 5-2 Characteristics of the aerodynamic fluctuating pressures for ATLAS-Agena payload shroud [13]**

## **5.4. Verification of the present prediction procedure**

### **5.4.1. Development of the verification procedure**

To verify the present prediction procedure (described in Section 5.2) for the fluctuating pressures on the surface of the vehicle, in-flight fluctuating pressure of the shroud in ATLAS-Agena launch vehicle is predicted by using the present procedure. And it is compared against those obtained from the semi-empirical models, which are Cockburn/Robertson's model, Efimtsov's model, and Goody's model. Those were briefly described in the previous sections.

Cockburn [13] presented the prediction results of the fluctuating pressure levels over the shroud section of the ATLAS-Agena launch vehicle at three flight Mach numbers (i.e. 0.7, 0.8, and 2.0). It was predicted by using the empirical method suggested by Lowson [58], which was derived from the previous flight test and wind tunnel measurement data. Cockburn proposed the prediction model for the fluctuating pressure loads acting on the external surface. The most complicated flow field for ATLAS-Agena was generated at  $Ma=0.8$ . It was shown that a series of shock waves, separated flow, and attached flow appear along the surface of the vehicle. Figure 5-2 shows the characteristics of the aerodynamic fluctuating flows for ATLAS-Agena payload shroud at three flight Mach

numbers. At  $Ma=0.8$ , the attached flow was developed at the shoulder without flow separation (Zone 1), reached supersonic speed right aft of the shoulder, and generated a terminal shock wave at Zone 2. Then the flow was separated immediately after the shock at  $0.1 D$  distance from the shoulder and re-attached at  $0.4 D$  (Zone 3). After that the flow remained to be attached beyond the relevant location [13].

#### **5.4.2. Predicting fluctuating pressure using the present procedure on the ATLAS-Agena shroud**

At first, three-dimensional CFD analysis is performed using FLUENT to obtain the time history of the pressure fluctuation acting on the surface of the vehicle. The analysis configuration and flight conditions are shown in Figure 5-3 and Table 5-1. It is found in General Dynamics Technical Report [54] and NASA Report [55].

In Figure 5-3, it is shown that the analysis target area is divided into four smaller zones to compare the characteristics of the flow between Cockburn's and the present model.

Choosing a proper turbulence model is an essential task for analysis of the turbulent flow field. It affects the accuracy of CFD simulation especially for complex flow fields. Many investigations have been studied to find a suitable turbulence model for the surface pressure fluctuations

induced by a turbulent flow. From the previous studies [59-61], the turbulence models can be categorized into the following two groups. The first one is the method based on time-averaged equation, typically Reynolds-averaged Navier-Stokes (RANS) model. And the second is the one based on spatially-filtered equations, such as large eddy simulation (LES) and detached eddy simulation (DES) [62]. RANS model is a well-known standard turbulence model. It needs a relatively low memory requirement and shows good convergence [63]. It is usually applicable for a simple flow field, such as an attached flow. On the other hand, LES and DES models are applicable for a complex flow field, such as shock waves and separated flows. Chern [59] and Juve [60] found that the RANS model was incapable of the shock wave boundary layer problem. They performed CFD simulations on a complex flow field by using LES model. However, the LES and DES models require significantly increased computational resources and have relatively inferior convergence properties. Numerous turbulence models are provided for use in FLUENT [63], such as RANS model including the Spalart-Allmaras one-equation model,  $k-\varepsilon$  and  $k-\omega$  two-equation model, and Menter's shear stress transport (SST) model, and so on. And it also provides the LES and DES turbulence models.

In this thesis, both realizable  $k-\varepsilon$  and LES turbulence models are used to predict a TBL flow and to evaluate their accuracies. Realizable  $k-\varepsilon$  model is a well-known standard turbulence model included in FLUENT. And to apply a near-wall mesh requirement for a TBL grid, lower than 500 of  $y^+$  (dimensionless wall distance) value need to be generated in the wall adjacent cells [18]. The time step of  $2.0 \times 10^{-5}$  sec. is used, which is chosen by previous study [18]. And 100 of the number of sub-iteration is used between each time step. To determine the number of sub-iteration, three of case studies are performed, as shown in Table 5-2 and Figure 5-4. The discrepancy of FSP spectrum between each case becomes decrease as number of sub-iteration increase; that is, there exist much discrepancy between cases I and II, but it shows similar FSP spectrum between cases II and III in high frequency range though the difference of number of sub-iteration between cases II and III is larger than one of cases I and II. From this case study, number of sub-iteration is determined as 100.

Figure 5-5 shows the three-dimensional CFD analysis result (Case 2) for ATLAS-Agena spacecraft shroud by using LES turbulence model. Figure 5-5 (a) shows the Mach number contour. From that, various flow patterns are found, and which are shock wave, separated flow, and

attached flow in each zone. It has similar flow characteristics to Cockburn's model but there exist a few differences, too.

One of the significant differences between Cockburn's and the present model occurs in Zone 1. In the present CFD analysis, the shock wave is developed in the front part of Zone 2 but it affects Zone 1. That is, the attached flow is not observed in Zone 1 in the present CFD. However, according to Cockburn's model, attached flow was developed in Zone 1 and right after that, shock wave was developed in Zone 2. The detailed investigation is available by examining the turbulent kinetic energy (TKE), as shown in Figure 5-5 (b). In it, separated flow and attached flow are developed aft of the shock flow as it is predicted by Cockburn's model (Zones 2 and 3). As shown in Figure 5-5 (b), the turbulence intensity can be estimated from the turbulent kinetic energy. The strongest TKE is developed in Zone 1 and the front part of Zone 2. It is caused by the shock wave (see Figure 5-5 (a)). In Zone 2, a little stronger TKE is developed over the surface but it becomes weaker near and on the surface. It is affected by the separated flow (see Figure 5-5 (a)). The thickness of the boundary layer cannot be easily identified in Figure 5-5 (a) because of the separated flow which affects the whole shroud surface.

The pressure fluctuating time history on the surface of the vehicle is predicted by using FLUENT. And then the pressure fluctuation spectrum on the surface is estimated using VA-ONE. The pressure fluctuating time

history obtained by FLUENT is used as input results for VA-ONE (See Figure 5-1). The time history data are imported at each relevant FEA grid point and then the mean pressure fluctuating spectrum is estimated on the surface using FFT and signal processing algorithm. The overall pressure fluctuating level spectrum on the surface is shown in Figure 5-5. The upper half of Figure 5-6 presents the overall pressure fluctuation contour and the lower one presents the dynamic pressure distribution. Comparing the two results, it is observed that the aerodynamic flows affect the pressure fluctuation level on the surface of the vehicle. In the dynamic pressure contour (lower half), the shock wave is generated in Zone 2 and it affects Zones 1 and 2 together. Concerning the overall pressure level (upper half), however, it is also found that the shock wave affects much further Zone 2 than it does Zone 1.

The small graph inside Figure 5-6 shows the averaged overall pressure level on each Zone with respect to distance from shoulder of the shroud. In it, the lowest overall pressure fluctuating level is induced in Zone 1 and the highest one is in Zone 2. But it decreases as the distance increases because the shock wave and separated flow are developed at the front fuselage and the attached flow is developed at the rear fuselage. Its trend is similar to that predicted in Cockburn and Robertson's model. By conducting more detailed observation on Zone 1, it is found that the dynamic pressure level is greater in Zone 1 than it is in Zone 2. But the

fluctuating pressure level becomes smaller in Zone 1 than it is Zone 2 because there exists a little pressure fluctuation component in Zone 1 (Figure 5-7 (a)), compared with that in Zone 2 (Figure 5-7 (b)). This can be observed from the time history of the total pressure, as shown in Figure 5-7. Similar statement was already described by Cockburn and Robertson [13], “the maximum fluctuating pressure does not always arise at the maximum free-stream dynamic pressure for certain regions with a rapid change of the cross-section due to the non-homogeneous flow field.”

Figure 5-8 shows the pressure fluctuating spectrum in each zone. In Zones 2, 3 which are the locations affected by the shock wave and separated flow, the spectrum value becomes greater than that for the locations affected by the attached flow, Zones 4 and 5. In addition, the spectrum in Zones 2, 3 contain higher frequency contents than those do in Zones 1 and 4. Therefore, it is found that the shock wave and separated flow generate increased frequency spectrum content than the attached flow does. In contrast, the spectrum generated by the attached flow presents a steeply decreasing tendency over 1,000 Hz frequency range.

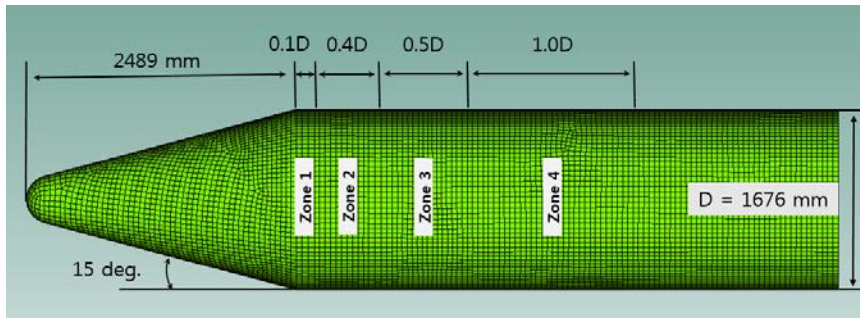


**Fig. 5-3 Verification analysis object configuration (FEA grid, ATLAS-Agena)**

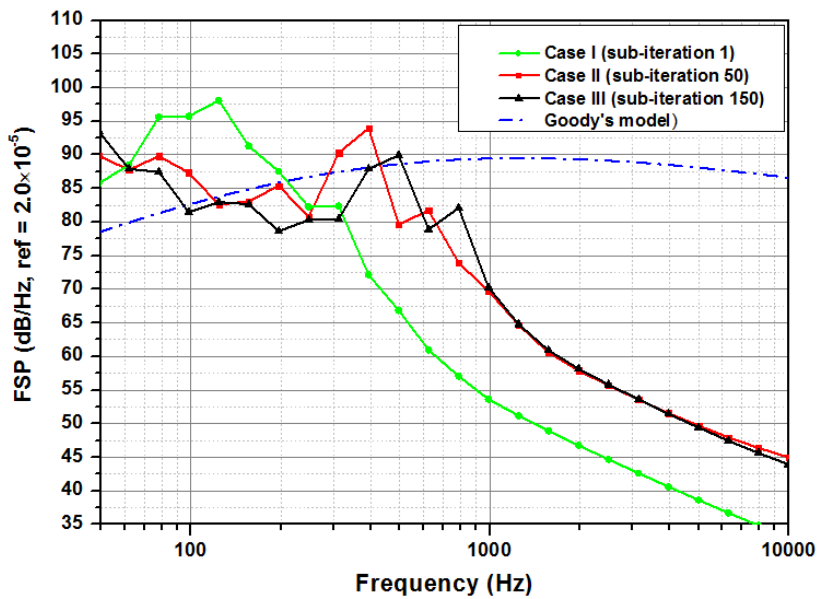
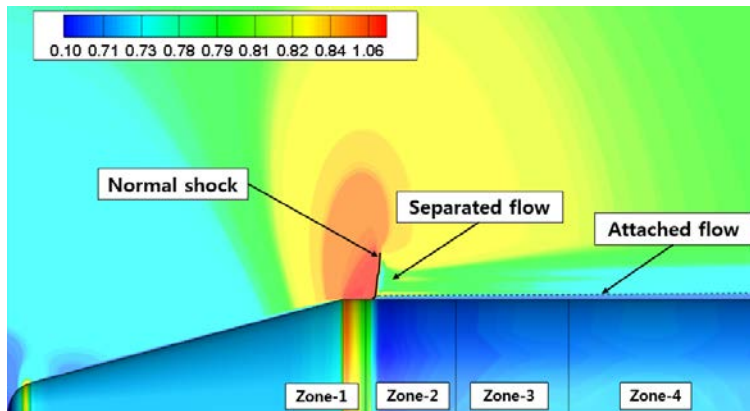
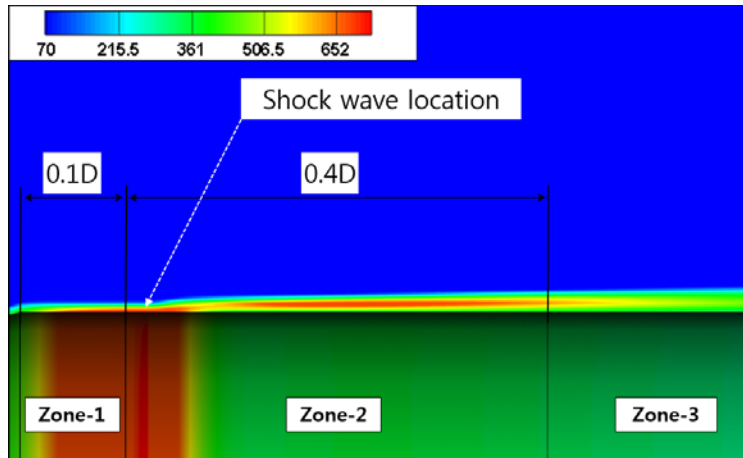


**Fig. 5-4 Variation of the FSP spectrum with respect to number of sub-iteration**



(a) Mach number contour



(b) Turbulent kinetic energy (TKE)

**Fig. 5-5 CFD analysis results of ATLAS-Agena  
(Ma = 0.8, Flight altitude = 5km)**

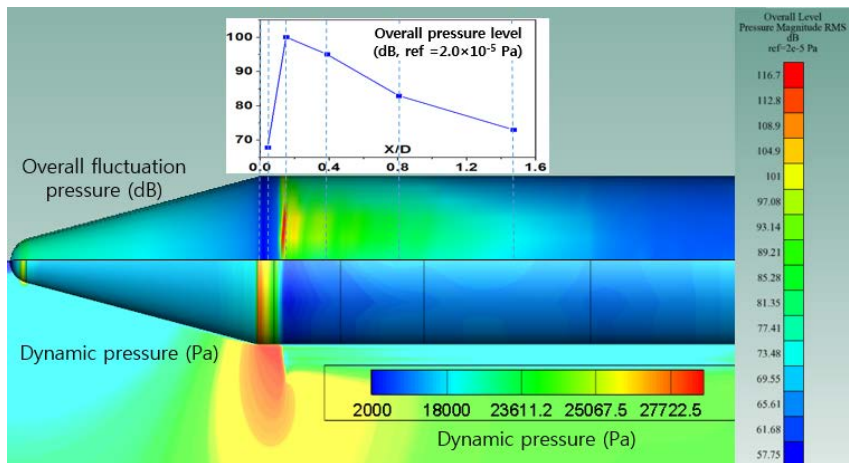
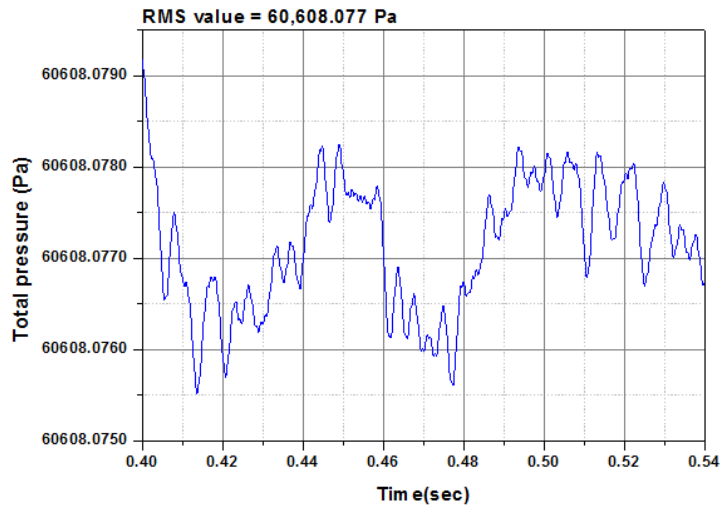
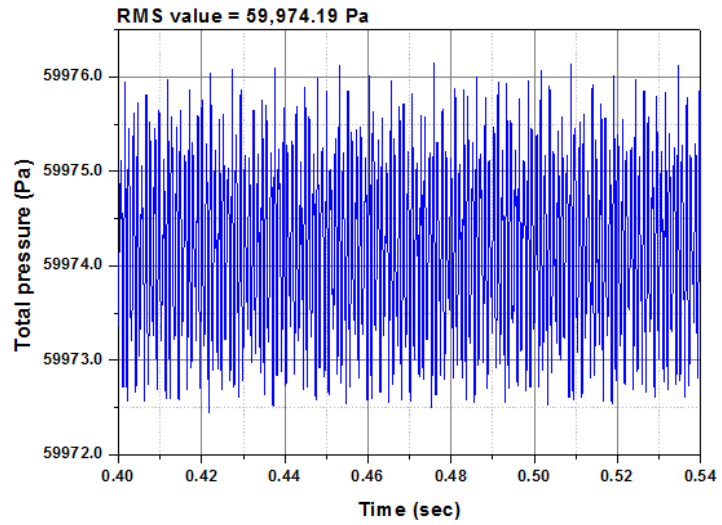


**Fig. 5-6 Distribution of the overall surface pressure spectra and dynamic pressure on the vehicle**



(a) Time history at Zone 1



(b) Time history at Zone 2

**Fig. 5-7 Time history of the total pressure in Zones 1 and 2**

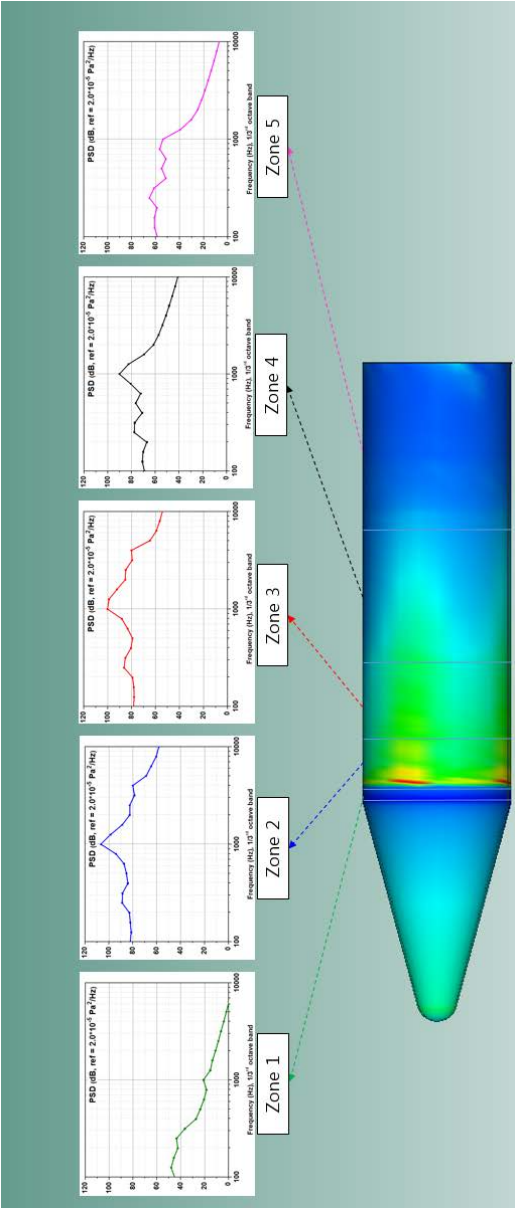


**Fig. 5-8 Surface pressure spectrum in terms of the distance from starting point of the attached flow**

**Table 5-1** Flight and CFD analysis condition of ATLAS-Agena

Parameter	Unit	Value
Mach number (Ma)	( - )	0.8
Altitude	(km)	5.0
Time duration	(sec)	1.0
Time step	(sec)	2.0e-05

**Table 5-2** Cases of sub-iteration

Case	Turbulent model	Residual	Number of sub-iteration	Time duration
I	K- $\epsilon$	$1.0 * 10^{-6}$	1	1.0 sec
II	K- $\epsilon$	$1.0 * 10^{-6}$	50	1.0 sec
III	K- $\epsilon$	$1.0 * 10^{-16}$	150	0.5 sec

### 5.4.3. Examination of the surface pressure fluctuation spectrum

To evaluate validity of the present estimation procedure about the pressure fluctuation spectrum, the present CFD results (Cases 1 and 2) are compared against the existing semi-empirical models. The estimation results in Zone 5 are chosen for comparison because the semi-empirical models were derived for the fully developed attached flow. The flow pattern in Zone 5 is regarded as an attached flow, as shown in Figure 5-5 (a).

Goody's model, and Cockburn/Robertson's model are used for the comparison. The flow parameters used to construct the semi-empirical models are chosen based on the CFD simulation results, in Table 5-3. And in Figure 5-9, the estimation result (sound pressure level in dB unit) of the present CFD is compared with those by the semi-empirical models.

In Table 5-3, "x" is the distance from the nose cone (i.e. leading edge of the TBL) and the Reynolds number can be formulated in the following form

$$\text{Re} = \frac{U_{\infty} x}{\nu} \quad (5-6)$$

Figure 5-9 shows the comparison of the fluctuating surface pressure spectrum between the present model and semi-empirical models. The blue line is the present model based on LES turbulent model and the pink one

is the one using the realizable  $k - \varepsilon$  turbulence model (herein RANS model). While the prediction by RANS model shows in relatively good agreement with that by Goody's model, the result by the LES model shows good agreement with Robertson's model below 1,000 Hz frequency range. Generally, Robertson's model is known to show relatively conservative prediction results. Juve [60] suggested that RANS turbulent model showed good agreement with the empirical models. This was especially true in the case of Goody's model for simple turbulent flows with zero pressure gradient, but it showed worse results for a complex flow field. Chern [59] showed that the power spectra of the pressure fluctuation at both shock wave and separated flow had good agreement with the LES model, although the attached flow and intermediate shock were not ideal.

The result by the present model becomes well-correlated with the semi-empirical models for lower than 1,000 Hz. But as the frequency increases, the spectra will decrease significantly. Therefore the discrepancies between the present model and the semi-empirical model become significantly larger as the frequency increases. However, it was also observed that the semi-empirical model failed to provide good estimation results for the higher frequency range compared with the measurement results. Klabas et al. [53] obtained and reported such observation results by comparing the surface pressure auto-spectra measurement result

corresponding to a research aircraft with the estimation results based on the semi-empirical models. Figure 10 shows one of his representative observation results. “Kulite 4” in the legend designates the measurement result obtained on the surface of the vehicle. Goody’s model fits better the value of the measurement result for the frequency range up to 2,000 Hz than the other semi-empirical models do. The measurement results show a rapidly decreasing trend for the frequency range larger than 2,000 Hz. But no other semi-empirical models are capable of correlating such a rapidly decreasing tendency for the higher frequency range [53].

In summary, the prediction procedure of the surface pressure fluctuation using the present prediction model is compared with those by the semi-empirical models to evaluate its validity. The present procedure predicts smaller spectra characteristics in the higher frequency ranges when compared with the semi-empirical models. However, similar characteristics were also observed in the measurement data of the fluctuating surface pressure in the previous study [53]. This discrepancy needs to be further studied and verified in the future.

Although the present estimation procedure shows differences for the higher frequency range, it features advantages at the same time. Different from the semi-empirical models, the present procedure is capable of estimating the surface pressure fluctuation for the complex aerodynamic flows such as shock waves, separated flow, and combined flow.

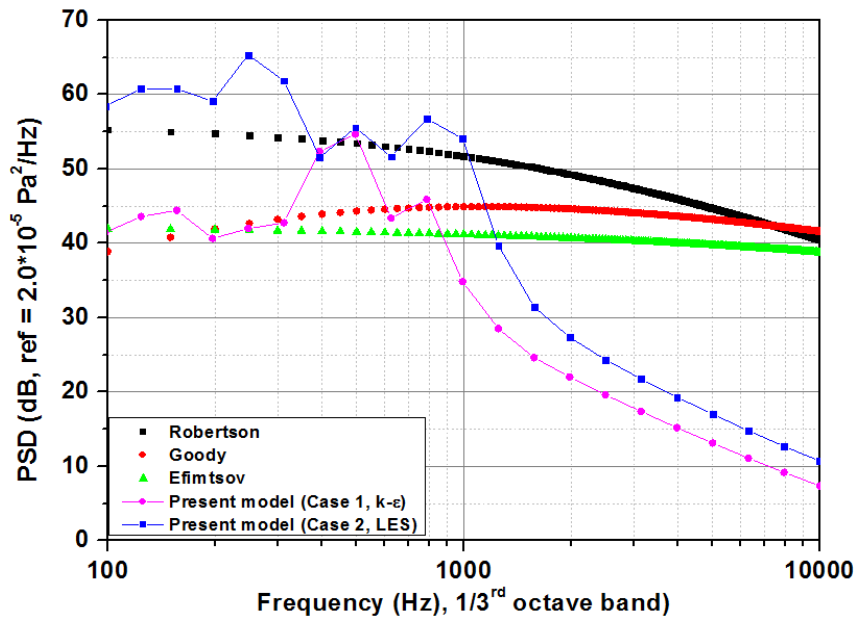
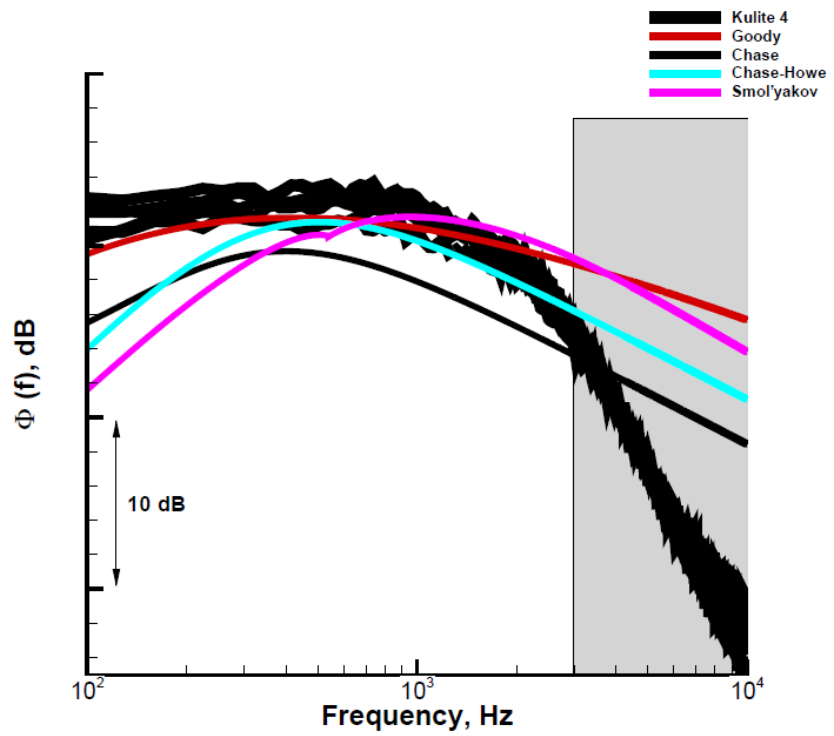


Fig. 5-9 Comparison between the present CFD results and the existing semi-empirical models (in Zone 4)



**Fig. 5-10 Auto spectrum of the fluctuating surface pressure observed by Klabas [9]**

**Table 5-3** Flow parameters for the present flight condition

Parameter	Unit	Value
Distance (x)	(m)	5.3
Density ( $\rho$ )	(kg/m <sup>3</sup> )	0.65
Kinematic viscosity ( $\nu$ )	(m <sup>2</sup> /s)	$1.789 \times 10^{-5}$
Reynolds number (Re)	(-)	$6.439 \times 10^7$

## **5.5. Fuselage excitation on a high speed flight vehicle**

### **5.5.1. Development of the present prediction analysis**

An HSFV is a supersonic flight vehicle with an axisymmetric circular inlet located at the front fuselage. As shown in Figure 5-11, an HSFV is composed of a center body, a cowl, and a plug. The plug moves back and forth to adjust the throttling ratio (T.R.). The throttling ratio is defined as the area ratio of the exit ( $A^E$ ) and the inlet ( $A^I$ ). In this paper, the throttling ratio is chosen as 0.85 to consider inlet buzz phenomenon. Hong [3] investigated the buzz phenomenon in various conditions of the throttling ratio. In his study, inlet buzz was initiated from T.R. = 1.62 to 0 on Nagashima's ramjet configuration.

The three-dimensional CFD calculation is performed to obtain the fluctuating surface pressure time history on the outer surface and inside the inlet surface of the vehicle by using the FLUENT program. Certain viscosity values, supersonic inflow conditions, and far-field outflow conditions are established and used. The fuselage angle of attack (AOA) is 3 degrees. To analyze the viscous flows, structured grids [63] are used because the structured grid is found to be more effective than the tetrahedral mesh [63] to consider the viscosity. The total number of grids used in this analysis is 3,110,292. Figure 5-12 shows the configuration of

the grid locations in the front section of the vehicle. On and near the surface of the inlet, the dense grids are applied to resolve the boundary layer. Regarding the turbulence model, the LES model is expected to be better than the RANS model for this configuration because the complex flows usually occur at the front fuselage (Figure 5-13). However, using the LES turbulence model may become impractical because HSFV is usually of a large size (longitudinal length is about 8 m). Although the RANS model has some limitations in resolving the complex turbulent flow, in this paper, 'realizable  $k - \varepsilon$  turbulence model' [63] is selected for use. This is for estimating the general characteristics of the fluctuating surface pressure inside of the air inlet and on the external surfaces of the vehicle.

The time-step size is chosen while considering accuracy of the analysis result and computational time because CFD usually requires abundance of time and the computational resources. Hong [48] presented the computational investigation on the inlet buzz characteristics in the supersonic inlet, which is similar to the present CFD computation. He carried out the time-step experiment and grid refinement test to determine a proper time-step size and grid dependency for efficient and accurate unsteady CFD computations. Four different grids and five time-step sizes are selected. Based on the previous study, the time-step of  $\Delta t = 2.0 \times 10^{-5}$

is used in this study. Table 5-4 shows the selected parameters in the present CFD analysis for HSFV in this thesis.

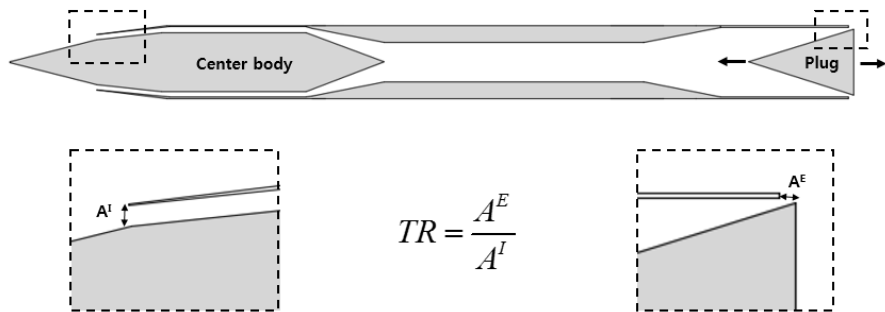


**Fig. 5-11 Conceptual configuration of the present HSFV.**

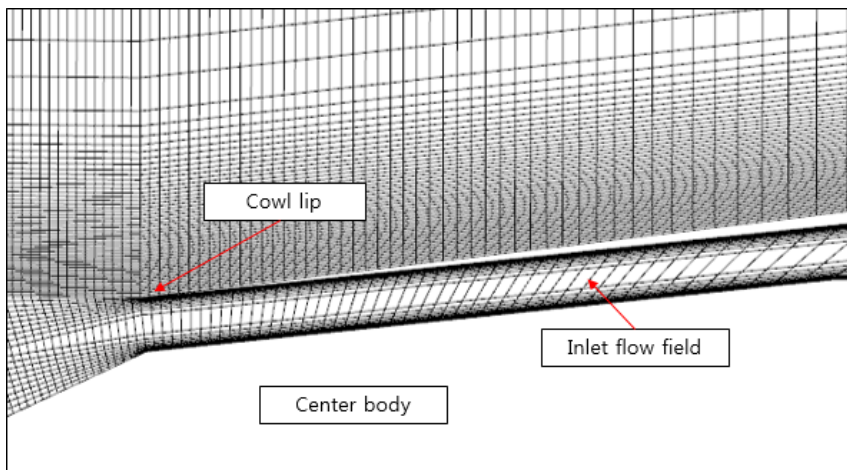


**Fig. 5-12 Configuration of the sectional grid locations  
(sectional view)**

**Table 5-4** Parameters of the present CFD analysis for HSFV

Turbulence model	Angle of attack	T. R.	Time-step (sec)	Time duration (sec)
Realizable $k-\varepsilon$	3°	0.85	$2.0 \times 10^{-5}$	0.5

## **5.5.2. Prediction of the fluctuating surface pressure on the vehicle**

Figure 5-13 presents a visualization of the Mach number distribution at two different times. The inlet buzz is observed in this flight condition and complex aerodynamic flows such as shock wave, separated flow, and attached flow are also observed at the front fuselage of the vehicle. The shock movement at the inside of the inlet is observed at two different times (in Figure 5-13 (a) and (b)), and it is regarded as a buzz phenomenon. The subdivided areas (FSP, FSP\_IN\_1, etc.) on which the fluctuating surface pressure impinges are shown in Figure 5-14.

It is known that regions exposed to separated flow and shock waves will encounter a certain level of fluctuating pressure, which is at least ten times greater in magnitude as compared to that in the regions exposed to an attached flow [13]. Thus, it can be expected that the regions at FSP\_IN\_1, FSP\_OUT\_1 and FSP\_OUT\_2 will experience greater fluctuating pressure levels than other regions in the vehicle due to the existence of the shock waves and separated flows, as showed in Figure 5-15.

Figure 5-14 shows the FEA grid configuration of the HSFV and the location of each fluctuating surface pressure impinging on the vehicle. From the present procedure (Figure 5-1), the averaged fluctuating pressure

spectrum can be obtained using VA-ONE, by importing the pressure time history data obtained by CFD analysis.

Figure 5-15 shows the overall fluctuating surface pressure level (OAFSPL) on the surface of the vehicle. The maximum value is located in the FSP\_IN\_1 and FSP\_OUT\_1 region. Compared with the CFD results, the shock wave and separated flow are found in this region, as shown in Figure 5-13.

On the external surface (Figure 5-15 (b)), the OAFSPL becomes decreased at the rearward location of the fuselage because the shock wave and the separated flow affect the front fuselage more than the rear one. This suggests that the attached flow is well developed from the FSP\_OUT\_3 location of the fuselage. On the other hand, inside of the inlet (Figure 5-15 (a)), the maximum OAFSPL is observed at the FSP where the normal shock is developed and all the OAFSPL's, inside of the air inlet, shows relatively larger values, when compared with those on the external surface. It is concluded that the air flow inside the inlet becomes turbulent enough to generate a large fluctuating surface pressure.

Figure 5-16 (a) and (b) shows the fluctuating pressure spectrum on the external surface and the inside of the inlet of the vehicle in the 1/12<sup>th</sup> octave band frequency, respectively. The legend included in Figure 5-16 indicates the location of the surface on the vehicle, as shown in Figure 5-14. Together with the fluctuating surface pressure caused by the turbulent

flow, periodic frequency contents caused by the buzz phenomenon are observed. All the periodic frequency component are harmonic, by the way. Its first frequency starts at 265 Hz, and the harmonic frequency is expressed as  $f_{harmonic} = 265 \times n$  Hz (where  $n = 1, 2, 3, \dots$ ). It is known as a buzz phenomenon, in general. And interesting characteristics are found, such that the periodic oscillation frequencies are found both of inside the inlet and on the external surface of the vehicle. It is concluded that the buzz affects not only the internal wall of the inlet but also the external surface of the vehicle. The periodic frequency at the external surface is caused by the normal shock oscillation which moves back and forth direction in the air inlet, and the shock movement affects the external flow of the vehicle (See Figure 5-13 (a) and (b)).

The maximum fluctuating pressure level is observed at FSP\_IN\_1 and FSP\_OUT\_1. This suggests that the fully turbulent flow is developed in this region due to the shock wave and separated flows. FSP\_OUT\_3 ~ 7, which exists far from the nose cone, show a relatively smaller fluctuating surface pressure compared to those at the front locations. It is found that the shock wave and separated flow generate quite strong fluctuating surface pressure compared to the attached flow. The fluctuating pressure spectrum generated by the shock wave and separated flow includes the higher frequency contents than those generated by the attached flow. The

maximum content is found to be greater by 40 dB than the minimum one in this case.

Both the fluctuating surface pressure and buzz phenomenon are generated inside the inlet and on the external surface of the vehicle. The periodic frequency contents caused by the buzz are distributed at every location of the vehicle, i.e., inside the inlet, and on the external surface. It is found that buzz generates higher magnitude having harmonic frequency content than those caused by turbulent flow, hence it may affect in part the vibratory responses of the vehicle. But buzz phenomenon is not considered as a dangerous excitation component. It does not occur in a nominal flight condition. In contrast, the fluctuating surface pressure inside the inlet is significantly larger than those of the external surface of the vehicle. It may be regarded as a major excitation component acting on HSFV that have circular air inlets with a ramjet engine.

In summary, the present computational analysis aims to predict and investigate the fluctuating surface pressure impinging on the external surface and internal air breathing inlet surface of the HSFV.

The prediction results by the present procedure, which is a combination of both CFD and structural FEA is compared with those of the semi-empirical models to assess the validity of the present procedure by using ATLAS-Agena. The present procedure shows relatively good agreement with the semi-empirical models at the frequency range lower than 1,000

Hz but shows large discrepancy in the higher frequency range. But it can be improved by applying a refined turbulence model such as LES model for CFD calculation. The LES turbulence model generally provides better prediction results for complex turbulent flows such as shock waves or separated flows than the RANS turbulence model does. However, it is not practical because it requires an abundant amount of computational resources to analyze a large scale vehicle.

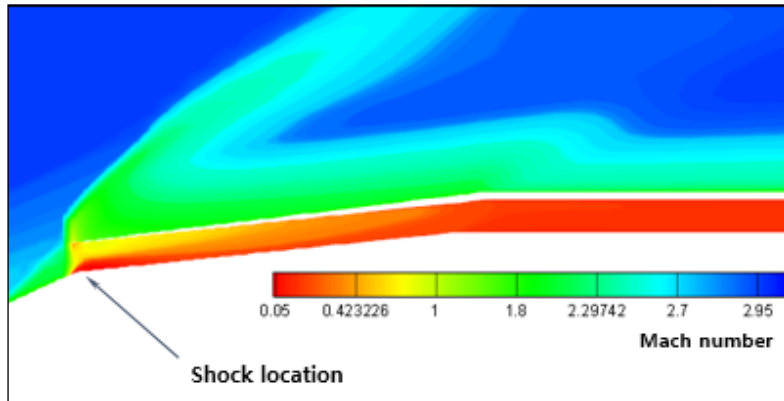
Comparing the present procedure with the semi-empirical models, the present model is capable of predicting the fluctuating surface pressure for complex aerodynamic flows such as shock waves, separated flow, and combined flow. This is in contrast to the semi-empirical model, which has certain limitations for predicting complex flows. It should be derived and tailored by using a sufficient amount of the empirical data measured from the wind tunnel and flight tests for the specific vehicle. The result by the present model becomes well-correlated with the semi-empirical models in the frequency lower than 1,000 Hz for the attached flow and it has similar tendency with Cockburn and Robertson's study for complex flows.

Considering the fluctuating pressure of an HSFV, on the external surface of the vehicle, the largest fluctuating surface pressure is found to exist near the cowl lip caused by shock waves and separated flow. And it becomes decreased at the rear fuselage because the shock wave and separated flow affect less and attached flow is well developed at the rear

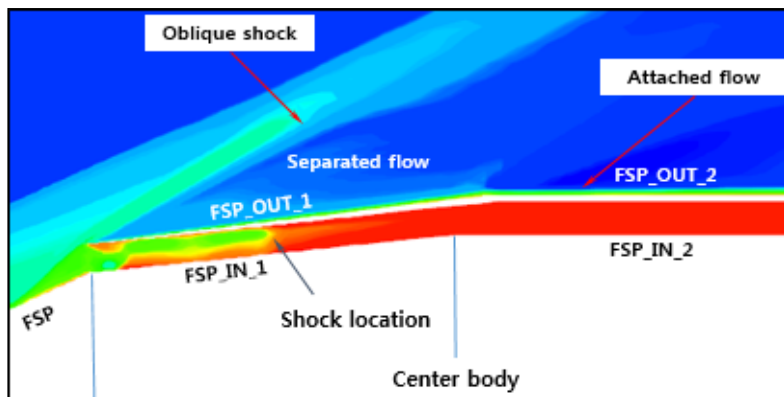
fuselage. In addition, the largest fluctuating surface pressure caused by the shock wave is greater than 40 dB in comparison with the smallest one caused by the attached flow. The fluctuating pressure spectrum generated by the attached flow shows a property of decreasing tendency in the higher frequency range.

On the other hand, inside of the inlet, the fluctuating surface pressures are larger than those of the external surface and it shows similar characteristics to the one generated by shock waves and separated flow. Therefore, for the supersonic flight vehicle that has an air breathing inlet such as an HSFV, the fluctuating pressure inside the inlet should be considered as a major excitation component.

In the future, a fully coupled analysis between CFD and CSD will be conducted for more accurate prediction on the vibratory response of an HSFV.



(a) Shock located out of the inlet



(b) Shock located inside the inlet

**Fig. 5-13 Shock movement at the inside the inlet (buzz effect) and flow field configuration**

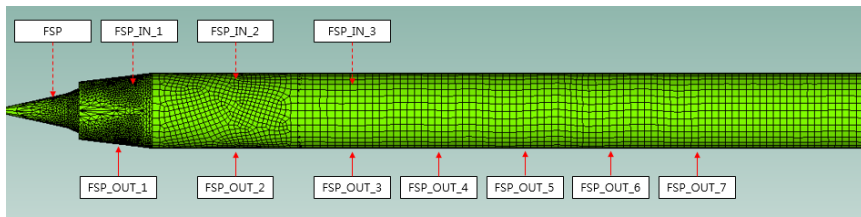
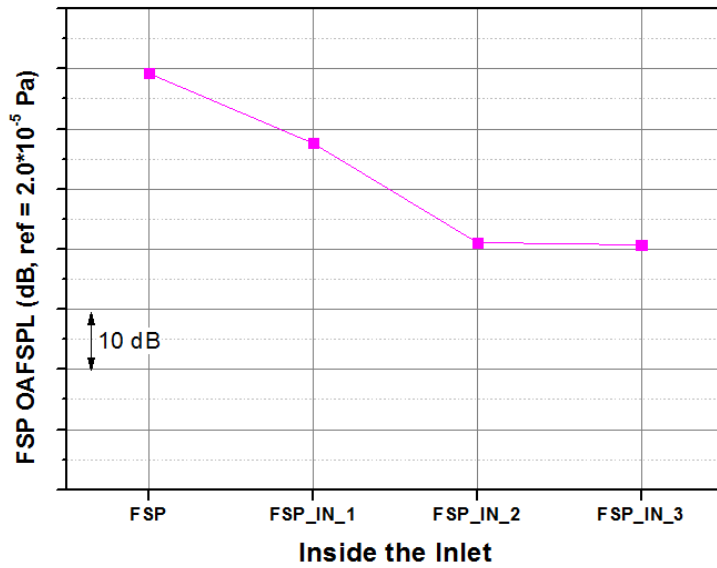
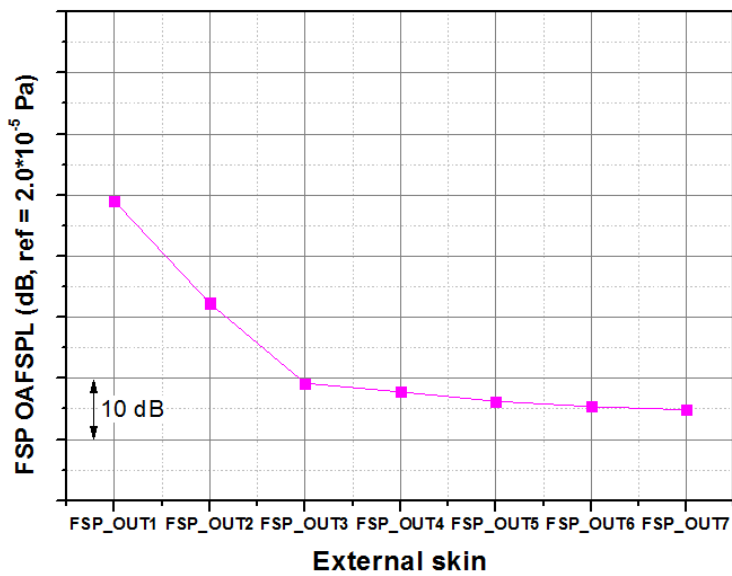


**Fig. 5-14** configuration of the FEA grid distribution

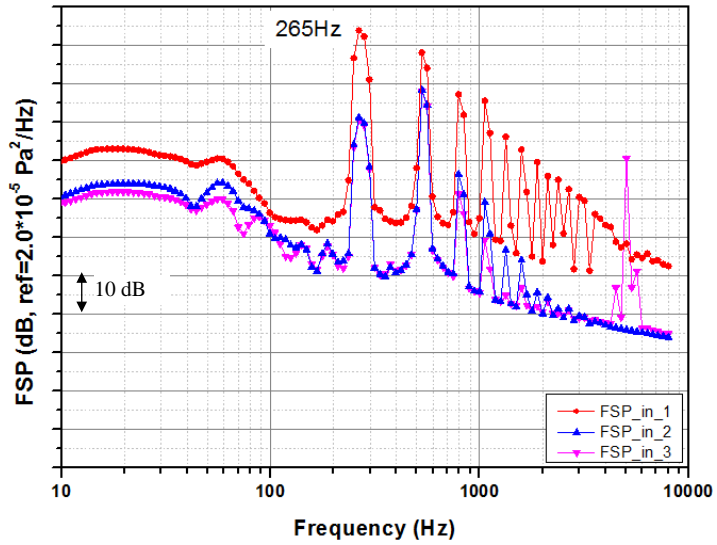


(a) OAFSPL inside the inlet

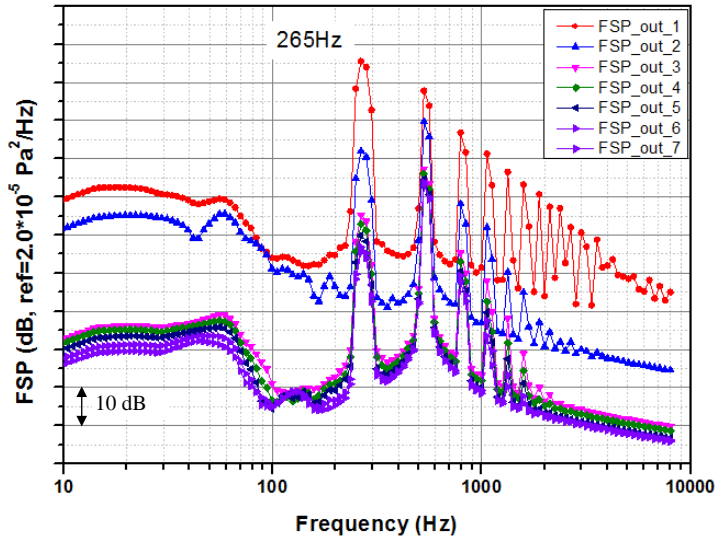


(b) OAFSPL on the external surface

**Fig. 5-15 Overall level pressure magnitude RMS (dB, ref=2.0e-5 Pa)**



(a) FSP inside the inlet



(b) FSP on the external surface

**Fig. 5-16 Fluctuating surface pressure spectrum on the external surface and inside the inlet**

## **Chapter 6.**

### **Vibratory Response Analysis Using SEA**

#### **6.1. Development of the Present Response Analysis Model**

The present HSFV SEA model was developed based on the shell element created by CATIA, a commercial computer-aided design software package. The commercial vibro-acoustic software package VA-ONE 2014 was used in this thesis because it is capable of solving vibro-acoustic problems precisely and efficiently, especially for large-scale structures and those in high frequency ranges.

The present HSFV subsystem includes the cylindrical skin, internal structural frame, fuel tank barrier/rib, and the inner air volumes. To build these subsystems, the curved shell, single curved shell, flat plate, and beam elements of the SEA subsystems were used considering the details of the geometry configuration and the structural characteristics. The present HSFV SEA model was composed of 98 SEA subsystems.

To evaluate the validity of frequency range of SEA subsystem, the ‘modes in band’ are examined at the equipment bay at the front part of the vehicle. It is generally recommended that the number of ‘modes in band’

should be greater than three ‘modes in band’ in a frequency band to have a confidence of SEA results. Figure 6-1 shows the number of ‘modes in band’ at the equipment bay in terms of frequency. The number of ‘modes in band’ in subsystem indicates that in order to maintain a minimum of three ‘modes in band’, will be valid for a frequency range greater than 500 Hz.

Defining the coupling loss factor (CLF) and the damping loss factor (DLF) is one of key parameters in SEA. The CLF and DLF are defined in a similar manner, but they are different in that the DLF is a measure of the power dissipation out of a subsystem while the CLF is that of power transmitted among subsystems. In general, the CLF can be evaluated by analytical method using semi-infinite assumption of typical subsystems but DLF is difficult to either predict or measure about its reliable values from either analysis or measurement. For that reason, many researchers have studied the DLF for interested structures or materials before they analyzed vibratory responses. Qinzhong Shi et al. [64] presented DLF values and estimation procedures using measurement about H-IIA launch vehicle. To predict DLF values, a real launch vehicle was used. They experimentally extracted by equipment the value of DLF and CLF of H-IIA fairing through impact and acoustic excitation.

Because predicting DLF using experimental method is difficult and a time-consuming task, in this paper, an empirical damping values

suggested by Lyon were used instead of experimental method. Lyon [18] suggested certain procedures for evaluating the damping loss factor (Figure 2-5). He suggested that an empirical damping value could be used when either measured or theoretical damping values were not available. It was estimated based on measured values for similar subsystems. Figure 2-5 shows the empirical damping loss factor for typical subsystems. From Figure 2-5, the DLF was selected to be 0.01 (1% damping) because general launch vehicles and missiles are composed of thin plates and shells joined by bolts and rivets. Therefore, in this thesis, vibratory response prediction for HSFV was performed by using DLF value of 0.01.

Figure 6-2 (a) shows the present HSFV SEA model. Diffuse acoustic field (DAF) excitation was used in the present SEA model to take the acoustic loads into account. The acoustic SPL results using DSM-II, as shown in Figure 3-3 (b), were applied to each surface of the HSFV as excitation loads using the properties of the inherent DAF excitation.

Point force excitation was used in the present SEA model to apply the self-excited vibration of the rocket motor at the rear locations of the vehicle, where an interface exists between the rocket motor and the vehicle structure.

The maximum acoustic SPL at a flight altitude of 6 m was selected from among the other possible prediction conditions where the acoustic loads were applied in the present SEA model. Table 6-1 shows the OASPL at

different positions in the present vehicle at the instant when the location of vehicle is 6 m away from the initial launch location.

To apply the fluctuating surface pressure impinging on the vehicle during cruise flight, TBL loading was used in the SEA analysis model and FSP (fluctuating surface pressure) loading was used in the FEA analysis model (Figure 6-2 (b)) to compute the vibration responses at different frequency ranges (e.g., SEA model: high frequency range, FEA model: low and mid frequency range). The present FEA model is composed of 30,296 FEA elements. Using the FEA model, the fluctuating surface pressure spectrum and TBL parameters can be estimated by the FSP in VA-ONE, which is used with the FEA subsystems with the pressure time history data imported from the CFD results.

The FEM analysis model was verified by comparing natural frequencies between analysis predictions and the modal experiment results of the vehicle. The first bending mode of the prediction is 68.2 Hz. It is similar to the modal experiment result (1<sup>st</sup> bending 63Hz) within 7% discrepancy.

**Table 6-1** OASPL on the surface (vehicle flight altitude: 6m)

Position No.	1	2	3	4	5
OASPL (dB)	139.0	137.0	135.1	133.2	132.0

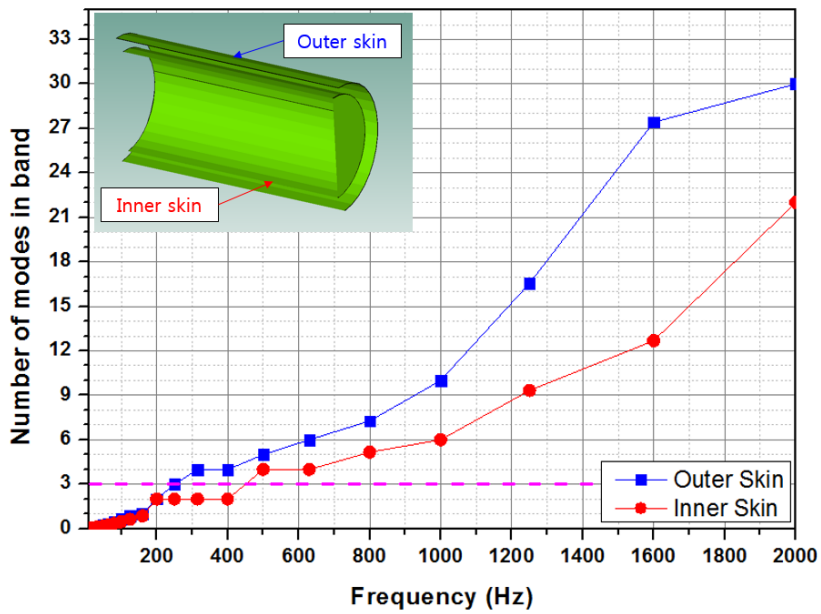
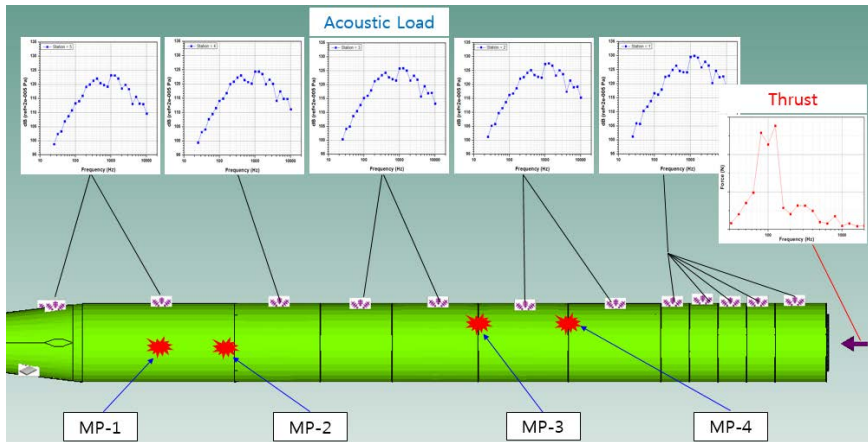
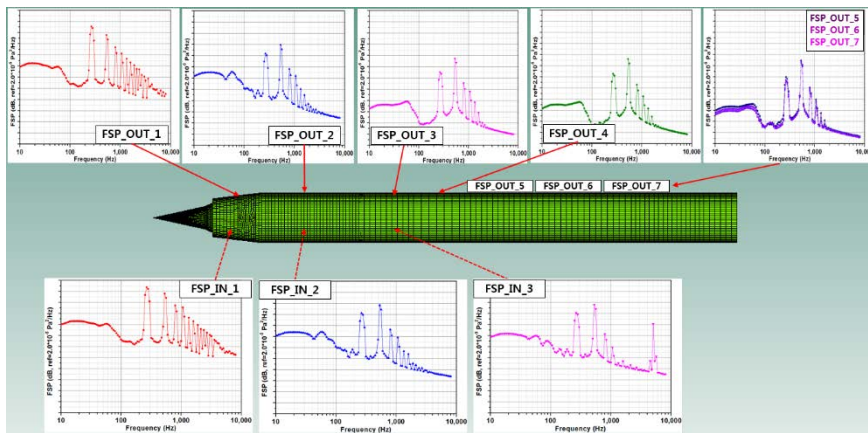


**Fig. 6-1** Number of “modes in band” at the equipment bay in terms of frequency (1/3<sup>rd</sup> octave frequency band)



(a) Acoustic loads and Rocket motor self-excited loads –SEA model  
(Lift-off condition)



(b) Fluctuating surface pressure distribution – FEA model  
(Cruise flight condition)

**Fig. 6-2 External depiction of the loads distribution on a HSFV**

## 6.2. Discussion of the Predicted Structural Response

Figure 6-3 shows the response prediction results at the mounting plate of the electronic equipment excited by only the self-excitation of the rocket motor. The pink circle represents the present SEA prediction result, the blue square represents the FEA result, and the red line denotes the vibration specification as suggested in MIL-STD-810 [6], which is the general environmental specification for military vehicles.

It is interesting to note the differences between the present SEA and FEA results because the reliability of SEA predictions usually drops in low frequency ranges while this occurs for FEA predictions in high frequency ranges [4].

The present SEA prediction was made using the 1/3<sup>rd</sup> octave band up to 2,000 Hz, while the FEA results were achieved with the 1 Hz frequency band up to 400 Hz. To confirm the appropriateness of the frequency range for the present SEA prediction, the number of “modes in band” for the subsystems was examined. The number of modes in band in subsystem indicated that in order to maintain a minimum of three modes in band, the prediction would be valid in a frequency range greater than 400 Hz. For this reason, the FEA prediction was obtained for frequencies up to 400 Hz. If the FEA result is obtained in a higher frequency range, the prediction results would not be valid due to the increased number of elements used

and the overlapped natural modes in the higher frequency range. It was expected that the prediction accuracy would become degraded and the computational time would increase rapidly as the frequency range increases.

Figure 6-3 shows that the present SEA prediction results were greater than those by FEA. It is known that SEA shows a tendency to provide greater values as compared to FEA due to the basic assumption in SEA, particularly in low frequency ranges. And the prediction results of SEA below 400 Hz is not reliable because the number of modes in band is not greater than three number in the subsystem. The peak values are observed at 135 Hz and 167 Hz. These values are assessed to be the fundamental and second resonant frequencies of the mounting plate of the electronic equipment. Because the response by FEA at 135 Hz is greater than the specification of MIL-STD-810, the plate must be reinforced to avoid possible resonant vibration. It is found that the major source of vibratory response caused by rocket motor self-excitation loads is a resonant burning. It generates high level of vibratory response in 80 to 120 of frequency range. Therefore resonant burning should be considered as a major excitation loads for HSFV.

Figure 6-4 shows the results at the equipment bay excited when only considering the acoustic loads on the surface of the present HSFV.

The SEA result was obtained in the 1/3<sup>rd</sup> octave band up to 8,000 Hz.

Figures 6-4 (a) and (b) compare the vibration response results at the equipment bay of the front part of the vehicle and the rear part of vehicle, respectively. The red line is the vibration specification suggested in MIL-STD-810. The specification at the rear fuselage is greater than that at the front fuselage because the rear fuselage is closer to the rocket motor than the front fuselage. The pink circle represents the frequency response at the mounting plate (MP-2); this value was used as a reference value to be compared with the specification (red line). On the whole, the reference value is smaller than the specification value. However, at the rear fuselage, it is very close to the specification level near 1,000 Hz. From these results, the mounting plate in the rear fuselage requires a protection measure from acoustic loads, especially near 1,000 Hz.

Figure 6-5 shows the results at the mounting plate of the electronic equipment excited by the acoustic loads and rocket motor self-excitation simultaneously. This excitation result is similar to that in the lift-off condition. In Figure 6-5 (a), the estimation results (pink square) are shown to exceed the specification limit in the frequency range between 80 Hz and 150 Hz. It was predicted that this result arose due to the self-excitation of the rocket motor. In a higher frequency range, the response increases as the frequency increases due to the acoustic loads, but the results are still within the specified range. In Figure 6-5 (b), the response is close to the specification limit at the frequency range over 1,000 Hz. This is regarded

to be due to the acoustic loads.

Rocket motor self-excitation affects the front fuselage more than it does the rear fuselage. It was found that this load is directly transferred to the front fuselage due to the system characteristics of the present HSFV. However, it was also found that the acoustic load affects the rear fuselage more than it does the front fuselage because the acoustic load on the surface is larger at the rear fuselage than that at the front fuselage.

During cruise flight, the vehicle is subjected to two different dynamic loads simultaneously. The first is the fluctuating load of the aerodynamic pressure, and the second is the self-induced load of the main engine. However, only aerodynamic loads are considered in this thesis because it is difficult to predict and/or measure self-induced loads of main engine. The self-induced loads of main engine will be studied more in future work.

Figure 6-6 shows the FEA prediction results as calculated in the 1/12<sup>th</sup> octave band at the different locations of each mounting plate excited by only the fluctuating loads of the aerodynamic pressure (see Figure 6-2 (b)). Mounting plates 1 (MP-1) is located in the front part of the fuselage, and mounting plate 3 (MP-3) is located in the rear part of the fuselage (Figure 6-2 (a)). The largest peak frequencies are observed to be 265 Hz and 530 Hz in MP-3 and MP-1, respectively. They are predicted as the response caused by buzz frequencies. The response in the front fuselage is larger than that in the rear case because the aerodynamic loads are more severe

in front fuselage as compared to the rear fuselage. The prediction results are over the specification limit at 265 Hz and 530 Hz but others are relatively low compared to the specification limit. This indicates that the fluctuating loads of the aerodynamic pressure caused by buzz effect excite the vehicle structure significantly as it is compared with the fluctuating surface pressure without buzz.

To investigate the sensitivity of vibratory response in terms of variation of the fluctuating surface pressure in high frequency range, the modified FSP spectrum (Figure 6-7 (a)) is applied to the SEA model at the locations of FSP\_OUT\_3, 4, 5, 6, and 7 (Figure 6-2 (b)). Figure 6-7 (a) shows the modified FSP spectrum. The pink circle is an original spectrum having large discrepancy with semi-empirical model beyond 800 Hz. The blue square is a modified spectrum corrected by Goody's model beyond 800 Hz. And the red dot is a spectrum estimated by Goody's model at the location of FSP\_OUT\_3 on HSFV. Figure 6-7 (b) shows the vibratory responses of the sensitivity test. It shows very little changes of the vibratory response comparing to the discrepancy of FSP spectrum in high frequency range (between original spectrum and modified one). From this sensitivity evaluation, it is found that vibratory response on the mounting plate (MP-1) of the electronic equipment in HSFV is affected very little by variation of fluctuating surface pressure in high frequency range. It means that vibratory response of HSFV caused by fluctuating surface

pressure has a reliability in this thesis even though the fluctuating surface pressure has an estimation error in high frequency range.

Figure 6-8 (a) shows the vibration response results at MP-1, excited by fluctuating loads of the aerodynamic pressure. The red line represents the SEA results and the blue line represents the results of the FEA method as calculated in the 1/3<sup>rd</sup> octave band and 1/12<sup>th</sup> octave band respectively. There are no SEA results available for low frequency ranges below 200 Hz. In the high frequency range of over 400 Hz, the predicted values of SEA are very similar to those of FEA prediction. Generally, in the high frequency range, it is known that SEA results are more reliable than those by a FEA method. For the computation time, the SEA method required less than 10 minutes to calculate the vibration response up to 8,000 Hz. On the other hand, the FEA method needed more than 47 hours to calculate the vibration response up to 2,000 Hz frequency ranges. It was found that SEA is a very powerful method when used to predict vibration responses, especially for large-scale structures and high-frequency vibration problems such as launch vehicle dynamic loads.

Thus, when predicting the vibratory responses of HSFVs, the FEA method is shown to be more effective in low and mid frequency ranges, whereas the SEA method becomes more valid in high frequency ranges over 400 Hz. Figure 6-8 (b) shows the vibratory response predictions by combining SEA and FEA in broad frequency range. Blue bar is obtained

from results of FEA within 400 Hz and red one is obtained from those of SEA beyond 400 Hz. Combining FEA and SEA results in a relevant frequency range is an effective method to estimate the vibratory response for HSFV.

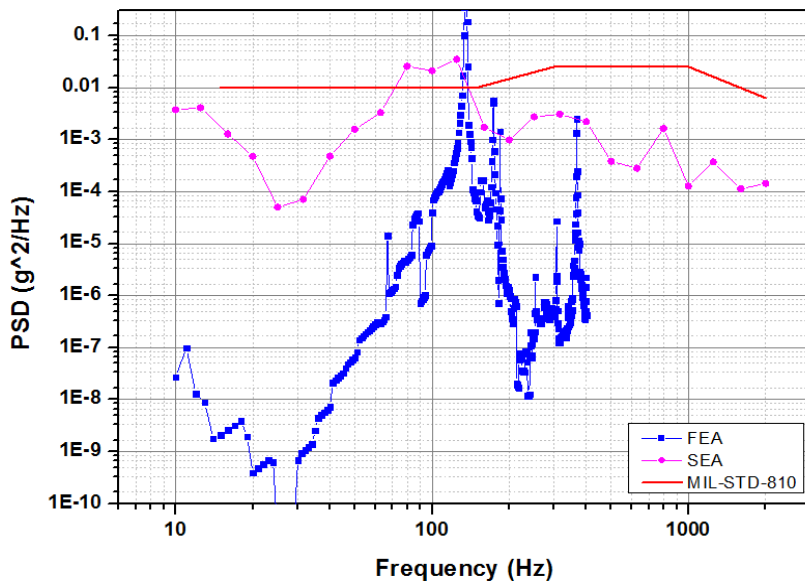
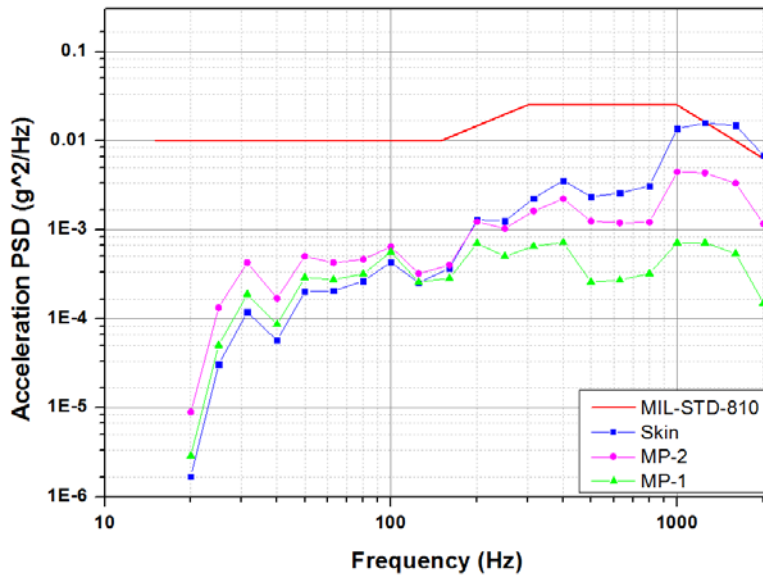
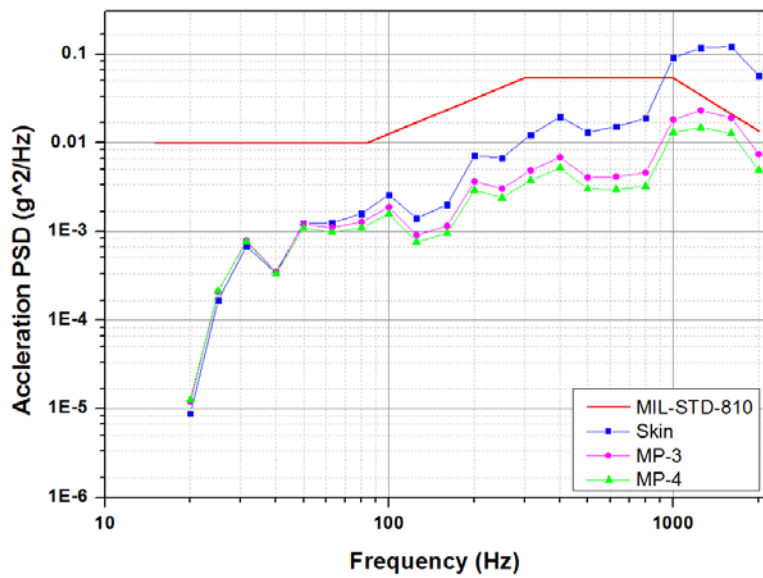


**Fig. 6-3 Comparison of the SEA and FEA response prediction results excited by the rocket motor**

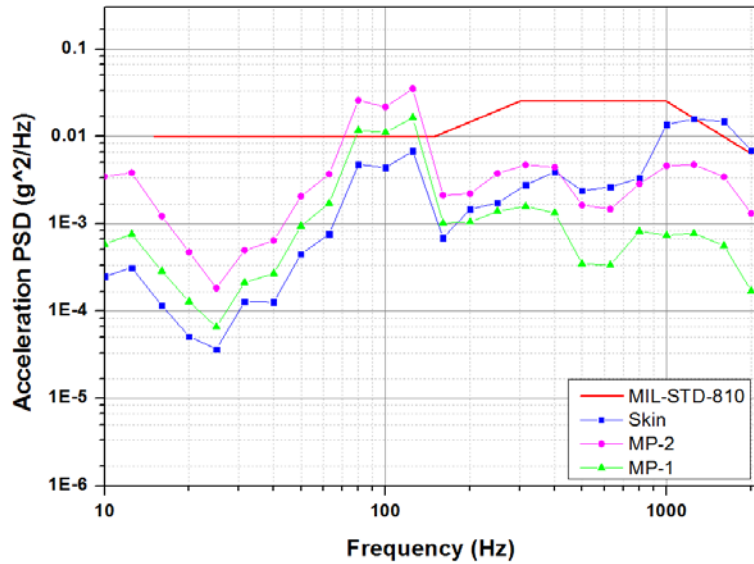


(a) Front mounting plate

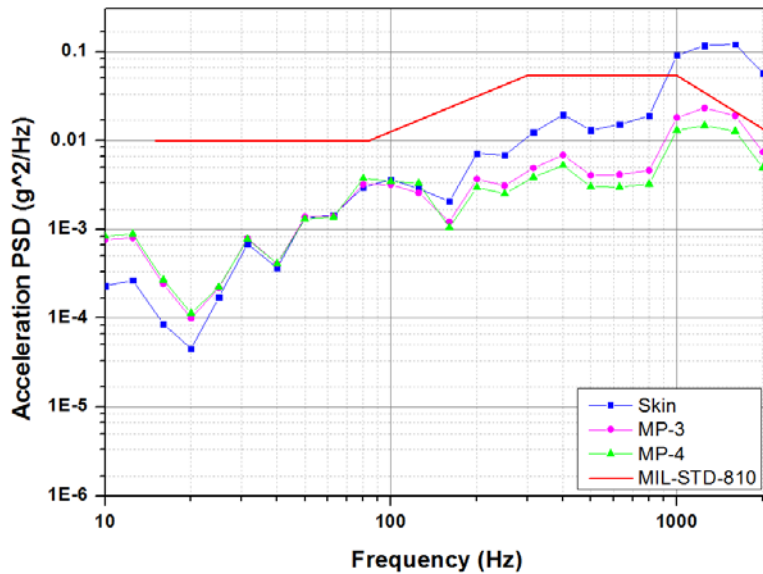


(b) Rear mounting plate

**Fig. 6-4 SEA analysis results at the mounting plate during the lift-off (as excited by acoustic loads)**



(a) Front mounting plate



(b) Rear mounting plate

**Fig. 6-5 SEA prediction results at the mounting plate during lift-off (excited by acoustic loads and by random loads of the rocket motor)**

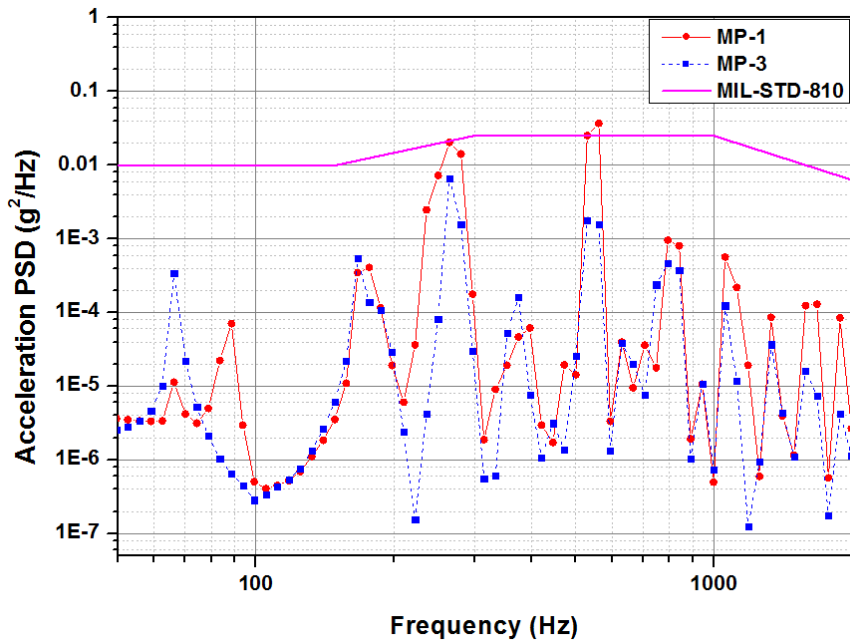
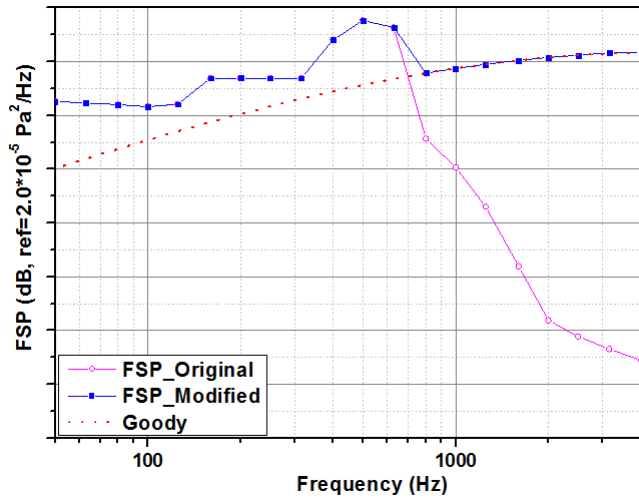
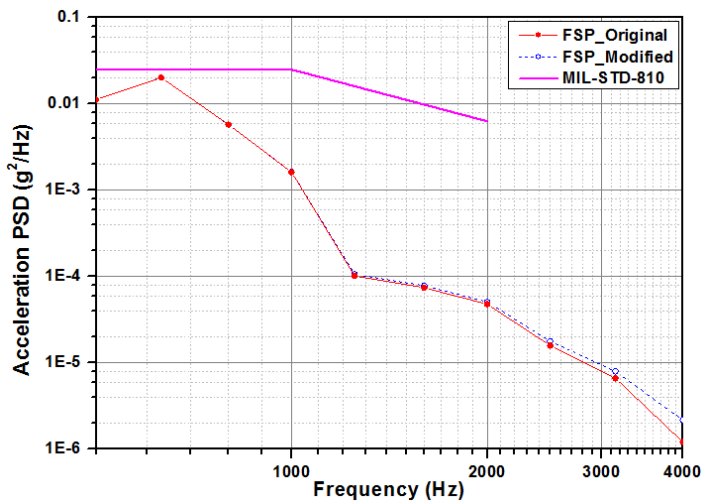


**Fig. 6-6 FEA prediction results at the mounting plate MP-1 (red) and MP-3 (blue) excited by the aerodynamic pressure fluctuating loads**

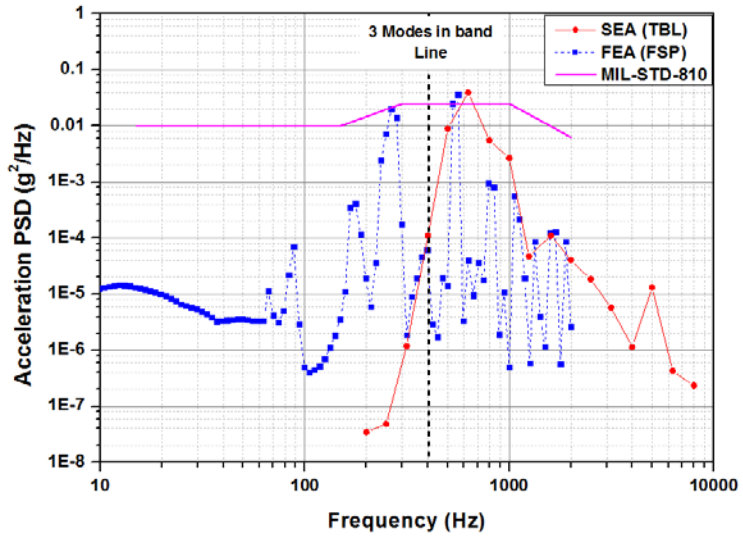


(a) Modified spectrum of the fluctuating surface pressure

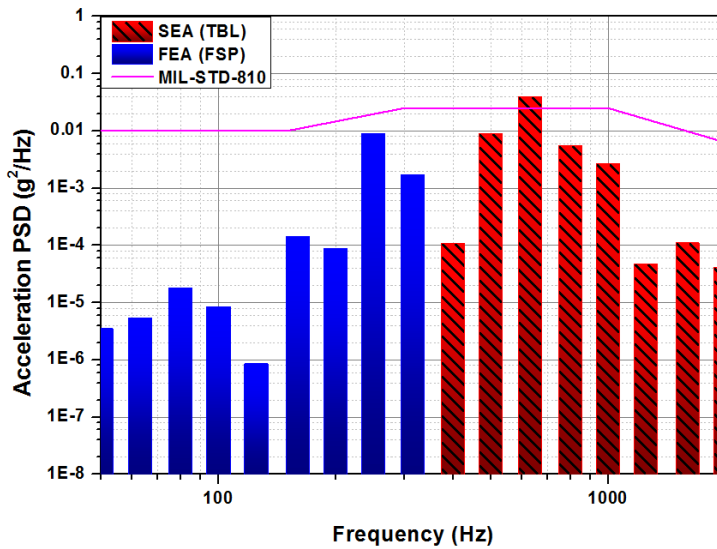


(b) Comparisons of vibratory response excited by different FSPs

**Fig. 6-7 Effectiveness of vibratory response in terms of variation of FSP spectrum in high frequency range**



a) FEA and SEA estimation results (at MP-1)



b) Combining estimation result of FEA and SEA

**Fig. 6-8 Comparison of response analysis results between SEA and FEA on mounting plate 1 (only excited by aerodynamic loads)**

## **Chapter 7.**

### **Conclusions and Future Works**

#### **7.1. Summary**

An analytical prediction methodology which helps to establish design specifications for the action of dynamic loads on the electronic equipment inside a vehicle was suggested. It provides the prompt prediction procedure of dynamic loads and vibratory responses for the special vehicles which do not have enough data can be applied in the early design stage of the vehicle. Using suggested methodology, the excitation loads and vibratory responses of the supersonic flight vehicle with air breathing inlet was predicted. The dynamic characteristics of this type of vehicle have not been known much until now. But it can be predicted by this study.

Three types of dynamic loads (i.e. acoustic loads, rocket motor self-excited loads, and aerodynamic fluctuating pressure) impinging on the vehicle were predicted using empirical, experimental and numerical method respectively. And then to predict vibratory loads on the vehicle, estimated dynamic loads were applied to the SEA and FEA structural analysis model. From this approach, the predicted responses were compared with the proposed specification limit suggested in MIL-STD-

810 to verify the appropriateness of the specification.

1. Acoustic loads impinging on the surface of the vehicle in terms of locations on the surface and flight altitude of the HSFV were predicted. An improved empirical method considering the screen effect and reflection effect caused by existence of launch canister was developed based on the DSM-II in NASA SP-8072. It was predicted that the maximum over all sound pressure level on the surface of the vehicle in terms of the flight altitude of the vehicle. And the frequency spectrum of the sound pressure level was predicted at relevant altitude.

2. The rocket motor self-excited load was obtained by the static firing test of the rocket motor. It was found that “resonant burning” which is the pressure oscillation frequencies correlates with those of the longitudinal acoustic modes of the solid rocket motor was observed between frequencies of 80 Hz to 120 Hz. The indirect force estimation method which estimates the unknown input force by using structural response measurement was proposed. To verify the practicability of the present approach, numerical simulation of a cantilevered beam was investigated. It showed good tracking capability to estimate various input forces (i.e., single sinusoidal force, impulsive force and random excitation force).

3. Computational analysis was shown to predict and investigate the fluctuating surface pressure impinging on the external surface and internal air inlet surface of the HSFV. The prediction results by the present procedure, which is a combination of both CFD and structural FEA was compared with those of semi-empirical models by using ATLAS-Agena launch vehicle. The results by the present prediction procedure become well correlated with semi-empirical models in the frequency lower than 1,000 Hz for the attached flow and it has similar tendency with previous study for complex flows. The major advantages of the present prediction procedure is that it is capable of predicting the fluctuating surface pressure for complex aerodynamic flows such as shock wave, separated flow, and combined flow. Considering the fluctuating pressure of an HSFV, the largest fluctuating surface pressure is found to exist near the cowl lip caused by shock waves and separated flow and it becomes decrease at the rear fuselage. The largest fluctuating surface pressure caused by shock wave is greater than 40 dB in comparison with the smallest one caused by attached flow. The fluctuating surface pressures, inside of the inlet, are larger than those of the external surface

4. Response predictions were conducted at the mounting plate of electronic equipment in a high-speed flight vehicle using SEA and FEA method. A SEA was used when acoustic loads and rocket motor self-

excitation impinge upon the vehicle (lift-off condition) and FEA and SEA method were used when only fluctuating loads of the aerodynamic pressure are subjected to the vehicle (cruise flight condition). From the results of this study, it was found that the most critical dynamic loads for HSFV launch events are the self-induced excitation loads of the rocket motor caused by resonant burning. These mainly affect the front fuselage in the low frequency range, whereas acoustic loads affect the rear fuselage more in the high frequency range. And, the fluctuating loads of the aerodynamic pressure affect the vibration response of the HSFV are relatively large compared to other dynamic loads in frequency range between 200 Hz to 2,000 Hz. And it is found that combining FEA and SEA method in a relevant frequency range will become more valid to estimate the vibratory response for HSFV. And it is capable of improving the reliability of the prediction and relieve computational loads.

## **7.2. Future Works**

The present thesis suggests a prediction methodology and prediction results of vibratory responses caused by various dynamic loads under special operating environment of HSFV. However, there will be a lot of challenges in this area, as follows:

1. Improved procedure of the input force estimation method in high frequency range will be studied by considering influence of the natural frequency on the input force estimation results.
2. Semi-empirical model of the aerodynamic pressure fluctuation loads for complex flow, such as shock wave and separated flows, and inside the inlet of HSFV will be required.
3. The present HSFV dynamic response assessments will be updated and refined. In addition, the vibratory response prediction methodology will be completed by considering all possible dynamic loads, especially for main engine loads, for HSFV launch events.
4. Hybrid analysis method (SEA+FEA) will be studied to improve calculation accuracy and computational efficiency of vibratory response for large scale structures in broad band frequency ranges.

## Bibliography

- [1] Kabe, A.M. *Design and verification of launch and space vehicle structures.* in *AIAA Structures, Dynamics and Materials Conference, number AIAA-98-1718.* 1998.
- [2] Osborne, E., et al., *Solid rocket motor random vibration,* in *37th AIAA/ASME/SAE/ASEE Joint Propulsion Conference.* 2001, American Institute of Aeronautics & Astronautics.
- [3] Dotson, K., J. Womack, and P. Grosserode, *Structural Dynamic Analysis of Solid Rocket Motor Resonant Burning.* *Journal of Propulsion and Power,* 2001. 17(2): p. 347-354.
- [4] Jeffrey M. Larko and V. Cotoni, *Vibroacoustic Response of the NASA ACTS Spacecraft Antenna launch Acoustic Excitation.* NASA/TM—2008-215168, 2008.
- [5] Larko, J.M. and W.O. Hughes, *Initial Assessment of the Ares IX Launch Vehicle Upper Stage to Vibroacoustic Flight Environments,* in *14th International Congress, Sound & Vibration, ICSV14.* 2008: Cairns, Australia.
- [6] *Department of Defense Test Method Standard for Environmental Engineering Considerations and Laboratory Tests.* 2000, MIL-STD-810F, US Department of Defense (DoD)(01.01. 2000).

- [7] *Spacecraft mechanical loads analysis handbook*. 2013, European Cooperation for Space Standardization.
- [8] Plotkin, K., L. Sutherland, and B. Vu, *Lift-Off Acoustics Predictions for the Ares I Launch Pad*. 2009.
- [9] Arenas, J.P. and R.N. Margasahayam, *Noise and Vibration of Spacecraft Structures*. Ingeniare. Revista chilena de ingeniería, 2006. 14(3): p. 251-264.
- [10] Conlon, S.C. and S.A. Hambric, *Predicting the vibroacoustic response of satellite equipment panels*. J Acoust Soc Am, 2003. 113(3): p. 1455-74.
- [11] ALLEN, A.R., *Vibro-acoustic sensitivity analysis of built-up systems using hybrid FE-SEA*. Master's Thesis 2, Acoustic Technology Technical University of Denmark, 2006.
- [12] Yang, M.Y. and J.F. Wilby, *Derivation of Aero-Induced Fluctuating Pressure Environments for Ares IX*, in *14th AIAA/CEAS Aeroacoustics conference(29th AIAA Aeroacoustics conference)*. 2008: Vancouver, British Columbia Canada.
- [13] Cockburn, J. and J. Robertson, *Vibration response of spacecraft shrouds to in-flight fluctuating pressures*. Journal of Sound and Vibration, 1974. 33(4): p. 399-425.
- [14] *VA One 2014 User's Guide*. 2014: vibro-acoustics, ESI.

- [15] Hwang, H.-J., *Prediction and validation of high frequency vibration responses of NASA Mars Pathfinder spacecraft due to acoustic launch load using statistical energy analysis*. 2002.
- [16] Troclet, B., et al., *FEM/SEA hybrid method for predicting mid and high frequency structure-borne transmission*. Open Acoustics Journal, 2009. 2: p. 45-60.
- [17] Fahy, F.J., *Statistical Energy Analysis: a critical overview*. Philosophical Transactions of the Royal Society of London A: Mathematical, Physical and Engineering Sciences, 1994. 346(1681): p. 431-447.
- [18] Lyon, R.H. and DeJong, R. G., *Theory and Application of Statistical Energy Analysis - second edition*. 1998: RH Lyon Corp.
- [19] Woodhouse, J., *AN Introduction to Statistical Energy Analysis of Structural Vibration*. Applied Acoustics, 1982. 14: p. 455-469.
- [20] Lee, D.-O., et al., *Shock Response Prediction of a Low Altitude Earth Observation Satellite during Launch Vehicle Separation*. International Journal of Aeronautical and Space Sciences, 2010. 11(1): p. 49-57.
- [21] Lee, D.-O., *Vibroacoustic and Shock Response Prediction of a Low Altitude Earth Observation Satellite Using Statistical Energy Analysis and Virtual Mode Synthesis and Simulation*, in *Division of Aerospace Engineering*. 2010, KAIST.

- [22] Ji, L. and Z. Huang, *A Simple Statistical Energy Analysis Technique on Modeling Continuous Coupling Interfaces*. Journal of Vibration and Acoustics, 2013. 136(1): p. 014501.
- [23] Cotoni, V., R.S. Langley, and P.J. Shorter, *A Statistical Energy Analysis Subsystem Formulation using Finite Element and Periodic Structure Theory*. Journal of Sound and Vibration, 2008. 318(4-5): p. 1077-1108.
- [24] Ming, R. and J. Pan. *The Limitation in the SEA Prediction of Power Transmission and Energy Distribution*. in *Fifth International Congress on Sound and Vibration*. 1997.
- [25] Center, L.R. and K. Eldred, *Acoustic Loads Generated by the Propulsion System*. 1971, National Aeronautics and Space Administration.
- [26] Pirk, R., et al., *Acoustics and Vibro-Acoustics Applied in Space Industry*. 2013.
- [27] Seoryong Park, S.J., HanAhChim Choung, Wonjong Eun, Ho-Joon Lee, SangJoon Shin, Soogab Lee. *Empirical acoustic loads prediction of high-speed vehicle including effects of launch pad*. *The 2015 International Congress and Exposition on Noise Control Engineering*. 2015. San Francisco, California, USA.

- [28] Dotson, K.W. and B.H. Sako, *Interaction between solid rocket motor internal flow and structure during flight*. Journal of propulsion and power, 2007. 23(1): p. 140-145.
- [29] Allen, M.S. and T.G. Carne. *Comparison of inverse structural filter (ISF) and sum of weighted accelerations technique (SWAT) time domain force identification methods*. 2006. 47th AIAA/ASME/ASCE/AHS/ASC structures, structural dynamics, and materials conference.
- [30] S. Rajkumar, A.D.B., C. Sujatha and S. Narayanan. *Comparison of Various Techniques used for Estimation of Input Force and Computation of Frequency Response Function (FRF) from Measured Response data*. in *The 22th International Congress on Sound and Vibration*. 2015. Florence, Italy.
- [31] Dobson, B. and E. Rider, *A review of the indirect calculation of excitation forces from measured structural response data*. Proceedings of the Institution of Mechanical Engineers, Part C: Journal of Mechanical Engineering Science, 1990. 204(2): p. 69-75.
- [32] Blanchet, D., et al., *Wind Noise Source Characterization and How It Can Be Used To Predict Vehicle Interior Noise*. 2014, SAE Technical Paper.

- [33] Shorter, P., D. Blanchet, and V. Cotoni, *Modeling interior noise due to fluctuating surface pressures from exterior flows*. 2012, SAE Technical Paper.
- [34] Welch, G. and G. Bishop, *An Introduction to the Kalman Filter*. 2006, Department of Computer Science University of North Carolina at Chapel Hill.
- [35] Young, P.C., *Recursive least squares estimation*, in *Recursive Estimation and Time-Series Analysis*. 2011, Springer. p. 29-46.
- [36] Tuan, P.-C., et al., *An input estimation approach to on-line two-dimensional inverse heat conduction problems*. Numerical Heat Transfer, 1996. 29(3): p. 345-363.
- [37] Ma, C.-K., et al., *A study of an inverse method for the estimation of impulsive loads*. International journal of systems science, 1998. 29(6): p. 663-672.
- [38] Ma, C.K. and D.C. Lin, *Input forces estimation of a cantilever beam*. Inverse Problems in Engineering, 2000. 8(6): p. 511-528.
- [39] Ma, C.K., J.M. Chang, and D.C. Lin, *Input forces estimation of beam structures by an inverse method*. Journal of Sound and Vibration, 2003. 259(2): p. 387-407.
- [40] Lee, M.-H., *Estimation of structure system input force using the inverse Fuzzy estimator*. Structural Engineering and Mechanics, 2011. 37(4): p. 351-365.

- [41] Lee, M.H. and C. Tsung-Chien, *Intelligent fuzzy weighted input estimation method for the input force on the plate structure*. Structural Engineering and Mechanics, 2010. 34(1): p. 1-14.
- [42] Lee, M.-H., *Inverse active vibration force inputs estimation for a beam-machine system*. International Journal of Systems Science, 2012. 43(4): p. 764-775.
- [43] Wu, A.L., et al., *Input force identification: application to soil-pile interaction*. Structural Control and Health Monitoring, 2009. 16(2): p. 223-240.
- [44] Chandrupatla, T.R., et al., *Introduction to finite elements in engineering*. Vol. 2. 2002: Prentice Hall Upper Saddle River, NJ.
- [45] Chowdhury, I. and S.P. Dasgupta, *Computation of Rayleigh damping coefficients for large systems*. The Electronic Journal of Geotechnical Engineering, 2003. 8.
- [46] Hewitt, P., B. Waltz, and S. Vandiviere, *Ramjet Tactical Missile Propulsion Status*. 2002, DTIC Document.
- [47] Nagashima, T., T. OBOKATA, and T. ASANUMA, *Experiment of Supersonic Air Intake Buzz*. Inst. of Space and Aeronautical Science of Tokyo, Report 37(7): p. 165-209, 1972.
- [48] Hong, W. and C. Kim, *Computational Study on Hysteretic Inlet Buzz Characteristics under Varying Mass Flow Conditions*. AIAA Journal 52(7) : p. 1357-1373, 2014.

- [49] Lu, P.-J. and L.-T. Jain, *Numerical Investigation of Inlet Buzz Flow*. Journal of Propulsion and Power, 1998. 14(1): p. 90-100.
- [50] Yeom, H.-W., H.-G. Sung, and V. Yang, *A Numerical Analysis of Supersonic Intake Buzz in an Axisymmetric Ramjet Engine*. Int J Aeronaut Space Sci, 2015. 16: p. 165-76.
- [51] Efimtsov, B., *Characteristics of the Field of Turbulent Wall Pressure Fluctuations at Large Reynolds Numbers*. Soviet Phisic Acoustics-USSR, 1982. 28(4): p. 289-292.
- [52] Goody, M., *Empirical spectral model of surface pressure fluctuations*. AIAA journal, 2004. 42(9): p. 1788-1794.
- [53] Klabes, A., et al. *Fuselage Excitation During Cruise Flight Conditions: Measurement and Prediction of Pressure Point Spectra*. in *21st AIAA/CEAS Aeroacoustics Conference*. 2015.
- [54] *External Design Loads – Operational CENTAUR Vehicles*. 1965, GENERAL DYNAMICS CONVAIR DIVISION San Diego, California.
- [55] *ATLAS-Centaur AC-12 Flight Performance for Surveyor III*. 1968, Lewis Research Center, Cleveland, Ohio.
- [56] Larko, J.M. and W.O. Hughes, *Initial Assessment of the Ares IX Launch Vehicle Upper Stage to Vibroacoustic Flight Environments*. 2008.

- [57] Yang, M.Y. and J.F. Wilby, *Derivation of Aero-Induced Fluctuating Pressure Environments for Ares IX*. AIAA Paper, 2008. 2801: p. 2008.
- [58] Lawson, M.V., *Prediction of Boundary Layer Pressure Fluctuations*. 1968, DTIC Document: Wright-Patterson Air Force Base, Ohio.
- [59] Chern, S.-Y., et al. *LES for Separated Supersonic Turbulent Boundary Layer and Shock Interaction*. in *52nd Aerospace Sciences Meeting*. 2014.
- [60] Juvé, D., M. Berton, and E. Salze, *Spectral Properties of Wall-pressure Fluctuations and Their Estimation from Computational Fluid Dynamics*, in *Flinovia-Flow Induced Noise and Vibration Issues and Aspects*. 2015, Springer. p. 27-46.
- [61] Mahmoudnejad, N. and K.A. Hoffmann. *Numerical Computation of Wall Pressure Fluctuations Due to a Turbulent Boundary Layer*. in *49th AIAA Aerospace Sciences Meeting including the New Horizons Forum and Aerospace Exposition*. 2011.
- [62] Sodja, J., *Turbulence models in CFD*. University of Ljubljana, 2007: p. 1-18.
- [63] *ANSYS Fluent 2016 User's Guide: Fluent*. 2016: ANSYS, Inc.

- [64] Shi, Q., et al. *Acoustic Analysis of H-IIA Launch Vehicle Fairing Using SEA*. in *Fourth International Symposium Environmental Testing for Space Programmes*. 2001.
- [65] Tuan, P.C., Ji C.C., Fong, L.W. and Huang, W.T., *An input estimation approach to on-line two-dimensional inverse heat conduction problems*, *Numeri. Heat Tr. B – Fund.*, 29, 345-363, 1996.
- [66] A. Powell, *On the approximatin to the infinite solution by the method of normal modes for random vibrations*, *Journal of the Acoustics Society of America* 30, 1136-1139, 1958.
- [67] A. Powell, *On the fatigue failure of structures due to vibrations excited by random pressure fields*, *Journal of the Acoustics Society of America* 30, 1130-1135, 1958.

# Appendix

## A. Recursive Least Square Estimation

The least square method is a standard approach to obtain the approximate solution of overdetermined systems, i.e., sets of equations in which there exist more number of equations than the number of unknowns. It is the solution to minimize the sum of the square of the errors between the estimation and given data including the noise

Suppose the following linear system.

$$y = Hx + v,$$

where

$x = (x_1, x_2, \dots, x_n)^T$  is a unknown constant vector,

$y = (y_1, y_2, \dots, y_k)^T$  is a noisy measurement vector,

$v = (v_1, v_2, \dots, v_k)^T$  is a measurement noise

$$\begin{pmatrix} y_1 \\ \vdots \\ y_k \end{pmatrix} = \begin{pmatrix} H_{11} & \cdots & H_{1n} \\ \vdots & \ddots & \vdots \\ H_{k1} & \cdots & H_{kn} \end{pmatrix} \begin{pmatrix} x_1 \\ \vdots \\ x_n \end{pmatrix} + \begin{pmatrix} v_1 \\ \vdots \\ v_k \end{pmatrix} \quad (\text{A-1})$$

Given  $\tilde{x}$  as an estimator of  $x$  and the error between the noisy measurement and the projected value:

$$e = y - H\tilde{x} \quad (\text{A-2})$$

Using the least square principle, we try to find  $\tilde{x}$  to minimize the error

$$\begin{aligned}
J(\tilde{x}) &= e^T e \\
&= (y - H\tilde{x})^T (y - H\tilde{x}) \\
&= y^T y - \tilde{x}^T H^T y - y^T H\tilde{x} + \tilde{x}^T H^T H\tilde{x}
\end{aligned} \tag{A-3}$$

$$\frac{\partial J}{\partial \tilde{x}} = -y^T H + \tilde{x}^T H^T H = 0 \tag{A-4}$$

$$\tilde{x} = (H^T H)^{-1} H^T y \tag{A-5}$$

Equation (A-5) have a solution when the number of measurements is not fewer than the number of variables.

If the measurement noise  $v$  has a variance  $\sigma$ , such as:

$$E(v_i^2) = \sigma^2$$

The covariance matrix of measurement noise:

$$\begin{aligned}
R &= E(vv^T) \\
&= \begin{pmatrix} \sigma_1^2 & \cdots & 0 \\ \vdots & \ddots & \vdots \\ 0 & \cdots & \sigma_k^2 \end{pmatrix}
\end{aligned}$$

The cost function can be defined as:

$$\begin{aligned}
J(\tilde{x}) &= e^T R^{-1} e \\
&= (y - H\tilde{x})^T R^{-1} (y - H\tilde{x}) \\
&= y^T R^{-1} y - \tilde{x}^T H^T R^{-1} y - y^T R^{-1} H\tilde{x} + \tilde{x}^T H^T R^{-1} H\tilde{x}
\end{aligned}$$

The partial derivative J over  $\tilde{x}$  is:

$$\frac{\partial J}{\partial \tilde{x}} = y^T R^{-1} H + \tilde{x}^T H^T R^{-1} H = 0$$

And we can find the best estimation of  $\tilde{x}$  as:

$$\tilde{x} = (H^T R^{-1} H)^{-1} H^T R^{-1} y \quad (\text{A-6})$$

If the measurements are obtained sequentially, we can update Equation (A-6) with each new measurement recursively.

A linear recursive estimator can be represented in the following form:

$$\begin{aligned} y_k &= H_k^T x + v_k \\ \tilde{x}_k &= \tilde{x}_{k-1} + K_k (y_k - H_k^T \tilde{x}_{k-1}) \end{aligned} \quad (\text{A-7})$$

where  $K_k$  is the estimator gain vector.

The new estimate  $\tilde{x}_k$  is updated from the previous estimate  $\tilde{x}_{k-1}$  with a correlation via the gain vector.

The mean value of current estimation error is as follows:

$$\begin{aligned} E(e_k) &= E(x - \tilde{x}_k) \\ &= E(x - x_{k-1} - K_k (y_k - H_k^T x_{k-1})) \\ &= E(e_{k-1} - K_k (H_k^T x + v_k - H_k^T x_{k-1})) \\ &= (I - K_k H_k^T) E(e_{k-1}) - K_k E(v_k) \end{aligned} \quad (\text{A-8})$$

where  $e_k = x - \tilde{x}_k$

The estimation error covariance is determined,  $P_k = E(e_k e_k^T)$ .

$$\begin{aligned} P_k &= \left[ ((I - K_k H_k^T) E(e_{k-1}) - K_k E(v_k)) ((I - K_k H_k^T) E(e_{k-1}) - K_k E(v_k))^T \right] \\ &= ((I - K_k H_k^T) P_{k-1} (I - K_k H_k^T)^T + K_k R_k K_k^T) \end{aligned} \quad (\text{A-9})$$

where  $E(v_k e_{k-1}^T) = E(v_k) E(e_{k-1}^T) = 0$ ,  $R_k = E(v_k^2)$ : covariance of  $v_k$

To find the gain vector  $K_k$ , we can minimize the cost function presented in Equation (A-8)

$$\begin{aligned} J_k &= E(e_k^T e_k) \\ &= E(\text{tr}(e_k e_k^T)) \\ &= \text{tr}(P_k) \end{aligned} \quad (\text{A-10})$$

Derivative  $J_k$  with respect to  $K_k$  is:

$$\left( \frac{\partial J_k}{\partial K_k} \right)^T = 2(I - K_k H_k^T) P_{k-1} (-H_k) + 2K_k R_k = 0$$

$K_k$  can be expressed as:

$$K_k = P_{k-1} H_k (H_k^T P_{k-1} H_k + R_k)^{-1} \quad (\text{A-11})$$

We substitute the Equation (A-11) into Equation (A-9) and arrange it to find  $P_k$ .

$$\begin{aligned} P_k &= (I - P_{k-1} H_k S_k^{-1} H_k^T) P_{k-1} (I - P_{k-1} H_k S_k^{-1} H_k^T)^T + P_{k-1} H_k S_k^{-1} R_k S_k^{-1} H_k^T P_{k-1} \\ &\quad \vdots \\ &= (I - K_k H_k^T) P_{k-1} \end{aligned}$$

$$\text{where } S_k = H_k^T P_{k-1} H_k + R_k \quad (\text{A-12})$$

The algorithm for the recursive least square estimation to find constant  $x$  of  $y = Hx + v$  is as follows.

(1) Initialize the estimator:

$$\begin{aligned} \tilde{x}_0 &= E(x) \\ P_0 &= E((x - \tilde{x}_0)(x - \tilde{x}_0)^T) \end{aligned}$$

In the case of no prior knowledge about  $x$ ,  $P_0 = \infty I$ . In the full knowledge,  $P_0 = 0$ .

(2) Iteration steps.

① Obtain a new measurement  $y_k$ ,

$$y_k = H_k^T x + v_k$$

where  $v_k$  has zero mean and covariance  $R_k$  ( $R_k = \sigma^2 \delta_{ij}$ )

② Update the estimate  $\tilde{x}_k$

$$K_k = P_{k-1} H_k (H_k^T P_{k-1} H_k + R_k)^{-1}$$

$$\tilde{x}_k = \tilde{x}_{k-1} + K_k (y_k - H_k^T \tilde{x}_{k-1})$$

$$P_k = (I - K_k H_k^T) P_{k-1}$$

## B. Intelligent Fuzzy Weighting Function in the Recursive Least Square Estimation of Input Force

The input force estimation method consists of the following two parts; one is the Kalman filter and the other is the recursive least square (RLS) algorithm. Some parameters of filter must be initialized before implementing estimation process. Those are the discrete-time processing noise covariance matrix  $Q$ , the discrete-time measurement noise  $R$ , and fading (weighting) factor for recursive least square method  $\gamma$ .

The equations of the Kalman filter without input force term are as follows:

State prediction:

$$\bar{X}(k/k-1) = \Phi \bar{X}(k-1/k)$$

State prediction covariance:

$$P(k/k-1) = \Phi P(k-1/k) \Phi^T + \Gamma Q \Gamma^T$$

Kalman gain:

$$K_a(k) = P(k/k-1) H^T [H P(k/k-1) H^T + R]^{-1}$$

Innovation covariance:

$$S(k) = H P(k/k-1) H^T + R$$

Updated state covariance:

$$P(k/k) = [I - K_a(k)H]P(k/k-1)$$

Innovation or Residual:

$$\bar{Z}(k) = Z(k) - H\bar{X}(k/k-1)$$

Updated state estimation

$$\bar{X}(k/k) = \bar{X}(k/k-1) + K_a(k)\bar{Z}(k)$$

The equations of the recursive least square estimator are as follows:

Sensitivity matrix:

$$B_s(k) = H[\Phi M_s(k-1) + I]\Gamma$$
$$M_s(k) = [I - K_a(k)H][\Phi M_s(k-1) + I]$$

Correction gain for the updating input forces:

$$K_b(k) = \gamma^{-1}P_b(k-1)B_s^T(k)[B_s(k)\gamma^{-1}P_b(k-1)B_s^T(k) + S(k)]^{-1}$$

Error covariance of the estimated input forces:

$$P_b(k) = [I - K_b(k)B_s(k)]\gamma^{-1}P_b(k-1)$$

Estimated input forces:

$$\hat{F}(k) = \hat{F}(k-1) + K_b(k)[\bar{Z}(k) - B_s(k)\hat{F}(k-1)]$$

Kalman gain ( $K_a(k)$ ) becomes smaller as the processing noise

covariance ( $Q$ ) decreases and the measurement noise covariance ( $R$ ) increases.  $R$  is can be chosen in accordance with the precision of the measuring sensor. Otherwise,  $Q$  can be chosen in accordance with the modular error of the system. The processing noise covariance ( $Q$ ) can be defined as follows:

$$Q_w(k+1) = Q_w(k) \times 10^{\alpha(k)}$$

where  $\alpha(k)$  is the fuzzy accelerating factor. The estimation precision becomes better as the  $\alpha(k)$  decreases.

The fading (weighting) factor ( $\gamma(k)$ ) is another important parameter which affects estimation precision and convergence speed in the RLS algorithm. It can be chosen within the interval  $[0, 1]$ . The larger value of  $\gamma(k)$  increases the convergence speed and smaller value of  $\gamma(k)$  improves the estimation accuracy.

The processing noise covariance ( $Q$ ) and fading factor ( $\gamma(k)$ ) can be optimized at each step by using intelligent fuzzy weighting factor which is based on the fuzzy logic inference system [40-42]. The weighting factor ( $\gamma(k)$ ) was derived by Tuan et al. [65] as follows.

$$\gamma(k) = \begin{cases} 1 & |\bar{Z}(k)| \leq \sigma \\ \frac{\sigma}{|\bar{Z}(k)|} & |\bar{Z}(k)| > \sigma \end{cases} \quad (\text{B-1})$$

The fuzzy logic system includes four basic components, which are the fuzzy rule base, the fuzzy inference engine, the fuzzifier, and defuzzifier. The value of fuzzy logic system input,  $\theta(k)$ , may be chosen within the interval, [0,1]. The dimensionless input variable is defined as the following

$$\theta(k) = \frac{\left| \frac{\Delta \bar{Z}(k)}{\bar{Z}(k)} \right|}{\sqrt{\left( \frac{\Delta \bar{Z}(k)}{\bar{Z}(k)} \right)^2 + \left( \frac{\Delta t}{t_f} \right)^2}} \quad (\text{B-2})$$

where  $\Delta \bar{Z}(k) = \bar{Z}(k) - \bar{Z}(k-1)$ ,  $\Delta t$  is the sampling interval, and

$t_f = 0.01$  is assumed. The fuzzy sets for  $\theta(k)$  and  $\gamma(k)$  are labeled in the linguistic terms, such as EL (extremely large), VL (very large), LV (large value), MV (medium value), SV (small value), VS (very small), and ES (extremely small). A fuzzy rule base is a collection of fuzzy IF-THEN rules which are shown in Table B-1.

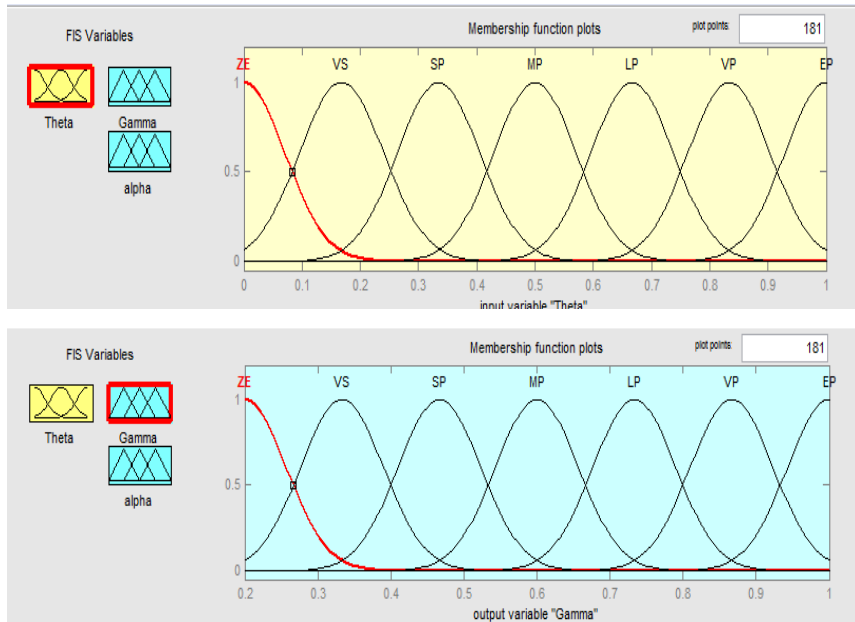
Table B-1. The fuzzy rule base

Input variable	$\theta(k)$	ES	VS	SV	MV	LV	VL	EL
Output variable	$\gamma(k)$	EL	VL	LV	MV	SV	VS	ES

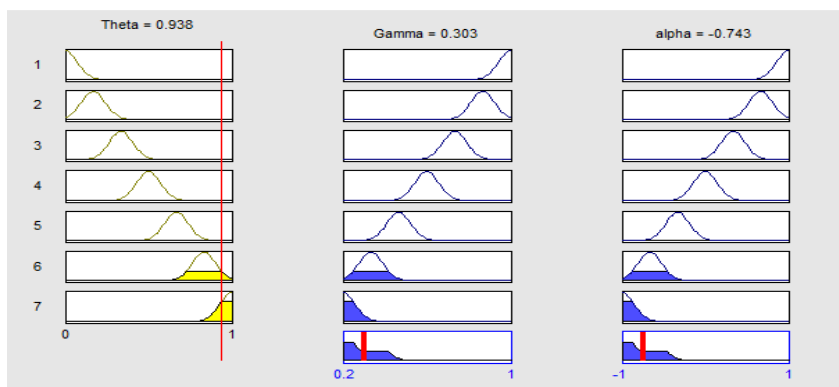
To implement fuzzy inference system, the Mamdani maximum-minimum inference engine in the MATLAB is used in this thesis.

Figure B-1 shows the membership function of the fuzzy sets and Figure B-2 shows the calculation example of Mamdani inference engine.

Figure B-3 shows the flowchart of the fuzzy estimator proposed by Lee et al. [40~42].



**Fig. B-1** Membership function of the fuzzy sets,  $\theta(k)$  and  $\gamma(k)$



**Fig. B-2** Calculation example of Mamdani inference engine

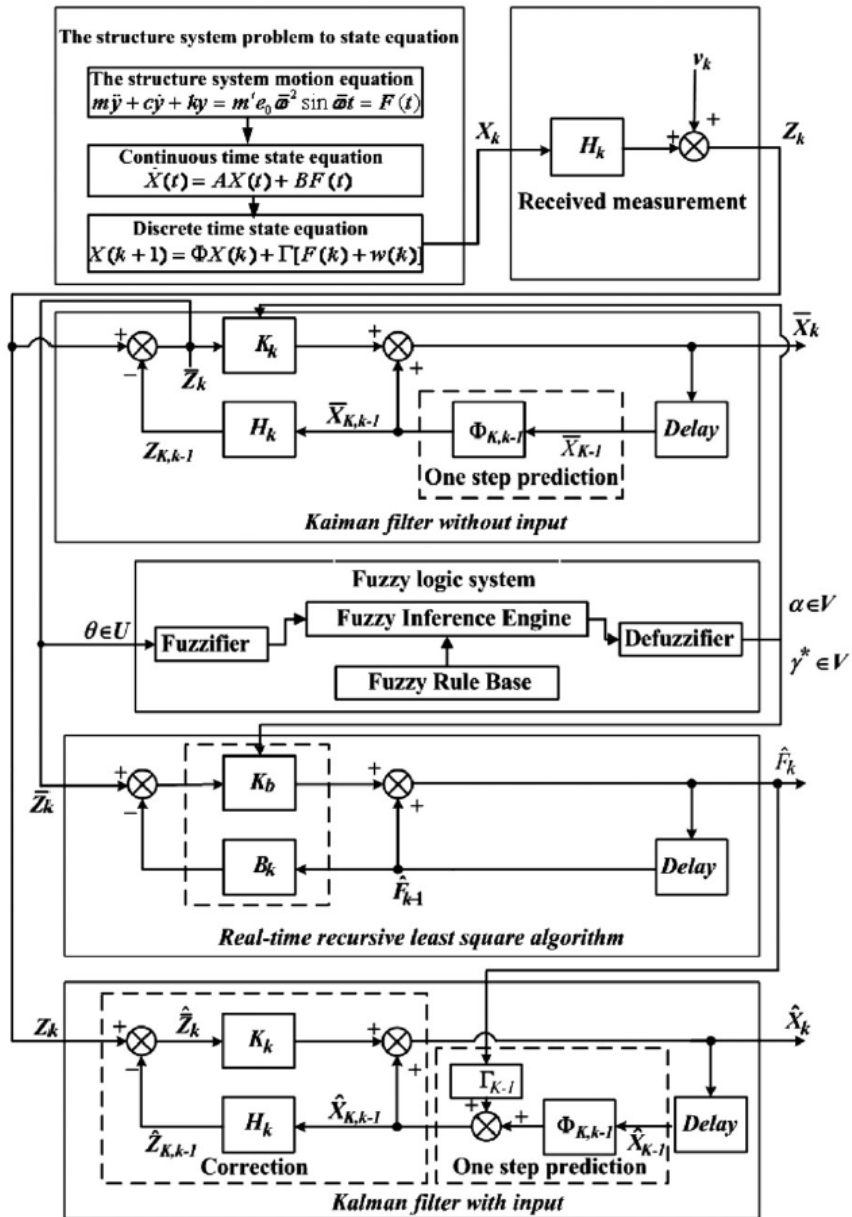


Fig. B-3 Flowchart of the fuzzy input estimation algorithm [40-42]

## **C. Damping Estimation Procedure using Input Force Estimation algorithm**

Structural damping is the key parameter of input force estimation procedure. It affects significantly the estimation result. However it is also known that it is quite difficult to estimate the damping for a complex structure.

In this thesis, the damping estimation procedure using the input force estimation algorithm is proposed as shown in Figure C-1.

Damping is assumed as a Rayleigh damping,  $[C] = \alpha[M] + \beta[K]$ . However, only the stiffness term,  $[C] = \beta[K]$ , is considered in this thesis because the stiffness term affects more the Rayleigh damping than it does the mass term as frequency increase, show Figure 4-4. In the present damping estimation procedure, if we know qualified structural responses at any typical positions and corresponding input forces using empirical test or numerical analysis, the most proper  $\beta$  can be estimated using an iterative method in Figure C-1.

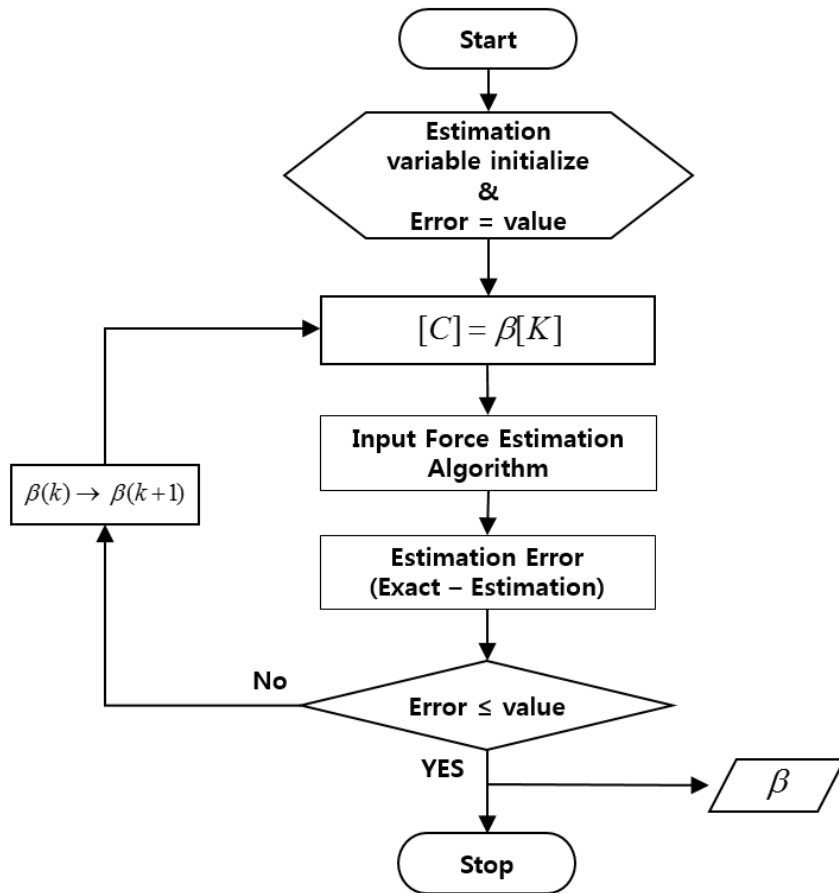


**Fig. C-1** Flowchart of damping estimation procedure

## D. Parameters for Prediction of Vibratory Response caused by Aerodynamic Fluctuating Pressure

The total mean-square response of a structure at any point depend upon:

- ① The summation of the mean square modal response
- ② The summation of the cross-correlations between pairs of modes

The cross terms are in some cases are significant; however, each term in this summation will become equal to zero if the space average of the mean square response is obtained. The cancellation of modal cross-correlations for space average response is due to orthogonality between the modes [66].

Powell's final result [67] for the space-averaged radial acceleration of a cylindrical shroud is as follows:

$$\frac{S_{ii}(\omega)}{S_p(\omega)} = \frac{1}{(\mu g)^2} \sum_{m=1}^{\infty} \sum_{n=1}^{\infty} \beta_{mn} H^2 \left( \frac{\omega_{mn}}{\omega} \right) j_{mn}^2(\omega) \quad (D-1)$$

where:

$S_{ii}(\omega)$  : the acceleration mean-square (power) spectral density in  
(  $g^2 / Hz$  )

$S_p(\omega)$  : the pressure mean-square (power) spectral density in

$$(Pa^2 / Hz)$$

$\mu$  : mass per unit area of the shroud surface ( $kg / m^2$ )

$g$  : gravitational acceleration ( $m / sec^2$ )

$\beta_{mn}$  : introduced by the space averaging, defined as follows:

$$\begin{aligned} \beta_{mn} &= 2, \quad m = 1, 2, \dots, \quad n = 0, \\ &= \frac{4n^4}{(1+n^2)^2}, \quad m = 1, 2, \dots, \quad n = 1, 2, 3, \dots, \end{aligned}$$

$H\left(\frac{\omega_{mn}}{\omega}\right)$ : magnification factor of the  $mn$  mode at frequency  $\omega$

$$H\left(\frac{\omega_{mn}}{\omega}\right) = \sqrt{\left\{\left(\frac{\omega_{mn}}{\omega}\right)^2 - 1\right\}^2 + \frac{1}{Q_{mn}^2}\left(\frac{\omega_{mn}}{\omega}\right)^2}$$

where  $Q_{mn}$  is the magnification factor at resonance,  $\omega_{mn}$  frequency, of the  $mn$  mode, and the subscript  $m$  and  $n$  denote the number of axial half waves and the number of full circumferential waves, respectively.

The joint acceptance ( $j_{mn}^2(\omega)$ ) refers to the pressure field and modes of the structure. It was defined by Powell [66] and described as following:

$$S_{Lm}(\omega) = S_{P_0} AH^2 j_{mn}^2(\omega) \quad (D-2)$$

where

$S_{Lm}$  : power spectral density of applied loads on the structure

$S_{p_{0m}}$  : power spectral density of aerodynamic fluctuating pressure

It describes a measure of the effectiveness of the complex pressure field in exciting a particular mode of the structure.

The joint acceptance term,  $j_{mn}^2(\omega)$ , refers to the direct joint acceptance of the  $mn$  mode of the structure and is generally assumed to be separable into  $m$  (axial) and  $n$  (circumferential) components.

$$j_{mn}^2(\omega) = j_m^2(\omega)j_n^2(\omega) \quad (D-3)$$

$$j_m^2(\omega) = \frac{1}{L_x^2} \int_{x=0}^{L_x} \int_{x=0}^{L_x} C(\zeta, \omega) \Phi_m(x) \Phi_m(x') dx dx' \quad (D-4)$$

$$j_n^2(\omega) = \frac{1}{L_y^2} \int_{y=0}^{L_y} \int_{y=0}^{L_y} C(\eta, \omega) \Phi_n(y) \Phi_n(y') dy dy' \quad (D-5)$$

$\Phi_m(x)$ ,  $\Phi_m(x')$ : axial components of the mode shape at point  $x$ ,  $x'$

$\Phi_n(y)$ ,  $\Phi_n(y')$ : circumferential components at point  $y$ ,  $y'$

where  $\zeta = (x - x')$ ,  $\eta = (y - y')$

$C(\zeta; \omega)$ ,  $C(\eta; \omega)$  are axial and circumferential narrow band space-correlation coefficients of the particular fluctuating pressure field (attached flow, separated flow, shock wave). Those have been proposed by many researchers with respect to different flow fields and different type of structures.

For example, Cockburn [13] proposed space-correlation coefficients

for an attached flow on the shroud of ATLAS-Agena as follows:

$$C(\zeta; \omega) = \exp \left[ - \left\{ 0.1 \frac{\omega |\zeta|}{U_c} + 0.27 \frac{|\zeta|}{\delta_l} \right\} \right] \cos \frac{\omega \zeta}{U_c} \quad , \text{longitudinal (D-6)}$$

$$C(\eta; \omega) = \exp \left[ - \left\{ 0.72 \frac{\omega |\eta|}{U_c} + 2.0 \frac{|\eta|}{\delta_l} \right\} \right] \quad , \text{circumferential (D-7)}$$

where  $\delta_l$  is a local thickness of the boundary layer, and  $U_c$  is a convection velocity.

In this thesis, space-correlation coefficients were estimated by VA-ONE using unsteady CFD analysis results (pressure in terms of time at each grid point). Space-correlation coefficients in VA-ONE is proposed as follows:

$$C(\zeta; \omega) = \exp \left[ -c_\zeta(\omega) \sqrt{k_\zeta^2(\omega) + k_\zeta^2(\omega) + \left( \frac{1}{3\delta_l} \right)^2 |\zeta|} \right] \cos(k_\zeta(\omega)\zeta) \quad (D-8)$$

$$C(\eta; \omega) = \exp \left[ -c_\eta(\omega) \sqrt{k_\zeta^2(\omega) + k_\zeta^2(\omega) + \left( \frac{1}{3\delta_l} \right)^2 |\eta|} \right] \cos(k_\eta(\omega)\eta) \quad (D-9)$$

where  $c_\zeta(\omega)$ ,  $c_\eta(\omega)$  : decay coefficient

$$k_\zeta(\omega) = \alpha(\omega) \frac{\omega}{U_c}, \quad \alpha(\omega)=1, \quad U_c = 0.7U_\infty$$

$$k_\eta(\omega) = \beta(\omega) \frac{\omega}{U_c}, \quad \beta(\omega)=0, \quad U_c = 0.7U_\infty$$

# 국문초록

## 공기 흡입구를 가진 초음속 비행체의 가진하중 및 진동응답 예측에 관한 연구

김진형

서울대학교 대학원

기계항공공학부

본 논문에서는 초음속 비행체의 동작 중 다양한 동적하중에 의해 발생하는 비행체의 진동응답 예측기법에 대한 연구를 수행하였다. 본 논문의 고속비행체는 램젯엔진과 같이 공기흡입구를 가지는 가상의 초음속 비행체이다. 이와 같은 고속비행체는 발사 시점이나 비행 중에 발생하는 매우 큰 동적하중을 경험하게 된다. 이러한 비행체는 진동에 취약한 고성능의 전자장비를 탑재하고 있으며 매우 얇은 스킨구조로 이루어져 있다. 이러한 경량구조물은 랜덤진동, 충격하중 그리고 음향하중 등이 발생하는 동작환경에 노출되어 있으며 진동하중에 취약한 탑재장비의 오작동의 원인으로 작용할 수 있다. 본 논문에서는 세 가지의 동적하중 (음향하중, 로켓모터

가진하중, 그리고 공력섭동압력하중)을 주요한 동적하중으로 고려하였다. 일반적으로, 우주발사체와 같은 큰 구조물에 대한 고주파수 영역에 대한 구조응답 해석은 ‘deterministic method’ (유한요소법 등)로 정밀하고 효율적인 예측이 어려운 것으로 알려져 있다. 이러한 고주파수 영역에 대한 일반적인 해석방법에 대한 단점을 극복하고자 본 논문에서는 ‘통계적 에너지 해석법’을 적용하였다. 또한, 진동응답 예측결과는 MIL-STD-810의 설계규격과 비교하여 적절성을 확인하였다. 본 논문의 목적은 다양한 동적하중으로 인하여 발생하는 초음속비행체의 기체구조물과 비행체 내부의 다양한 위치에서의 탑재장비 진동응답을 예측하여 이를 동적하중에 대한 설계규격으로 작성할 수 있는 예측기법에 대한 연구의 수행이다.

주제어: 진동응답, 통계적 에너지 해석법, 음향하중, 로켓모터  
진동하중, 압력섭동하중.

학 번: 2013-30195